

MOLECULAR HYDROGEN AND GLOBAL STAR FORMATION RELATIONS IN GALAXIES

BRANT E. ROBERTSON^{1,2,3} AND ANDREY V. KRAVTSOV^{1,2}

Draft version February 6, 2020

ABSTRACT

We use hydrodynamical simulations of disk galaxies to study relations between star formation and properties of the molecular interstellar medium (ISM). We implement a model for the ISM that includes low-temperature ($T < 10^4$ K) cooling, directly ties the star formation rate to the molecular gas density, and accounts for the destruction of H_2 by an interstellar radiation field from young stars. We demonstrate that the ISM and star formation model simultaneously produces a spatially-resolved molecular-gas surface density Schmidt-Kennicutt relation of the form $\Sigma_{\text{SFR}} \propto \Sigma_{\text{H}_2}^{n_{\text{mol}}}$ with $n_{\text{mol}} \approx 1.4$ independent of galaxy mass, and a total gas surface density – star formation rate relation $\Sigma_{\text{SFR}} \propto \Sigma_{\text{gas}}^{n_{\text{tot}}}$ with a power-law index that steepens from $n_{\text{tot}} \sim 2$ for large galaxies to $n_{\text{tot}} \gtrsim 4$ for small dwarf galaxies. We show that deviations from the disk-averaged $\Sigma_{\text{SFR}} \propto \Sigma_{\text{gas}}^{1.4}$ correlation determined by Kennicutt (1998) owe primarily to spatial trends in the molecular fraction f_{H_2} and may explain observed deviations from the global Schmidt-Kennicutt relation. In our model, such deviations occur in regions of the ISM where the fraction of gas mass in molecular form is declining or significantly less than unity. We show that long gas consumption time scales in low-mass and low surface brightness galaxies may owe to their small fractions of dense, molecular, star-forming gas rather than mediation by strong supernovae-driven winds. Our simulations also reproduce both the observed relation between ISM pressure and molecular fraction and the relation of the star formation rate, gas surface density, and disk angular frequency. We show that the Toomre criterion that accounts for both gas and stellar densities correctly predicts the onset of star formation in our simulated disks. We examine the density and temperature distributions of the ISM in simulated galaxies and show that the density probability distribution function (PDF) generally exhibits a complicated structure with multiple peaks corresponding to different temperature phases of the gas. The overall density PDF can be well-modeled as a sum of lognormal PDFs corresponding to individual, approximately isothermal phases. We also present a simple method to mitigate numerical Jeans fragmentation of dense, cold gas in Smoothed Particle Hydrodynamics codes through the adoption of a density-dependent pressure floor.

Subject headings: Galaxies, Star Formation

1. INTRODUCTION

Galaxy formation presents some of the most important and challenging problems in modern astrophysics. A basic paradigm for the dissipational formation of galaxies from primordial fluctuations in the density field has been developed (e.g. White & Rees 1978; Blumenthal et al. 1986; White & Frenk 1991), but many of the processes accompanying galaxy formation are poorly understood. In particular, star formation shapes the observable properties of galaxies but involves a variety of complicated dynamical, thermal, radiative, and chemical processes on a wide range of scales (see McKee & Ostriker 2007, for a review). Observed galaxies exhibit large-scale correlations between their global star formation rate surface density Σ_{SFR} and average gas surface density Σ_{gas} (Kennicutt 1989, 1998), and these global correlations serve as the basis for treatments of star formation in many models of galaxy formation. While such models have provided important insights, the validity and general applicability of a global $\Sigma_{\text{SFR}} - \Sigma_{\text{gas}}$ correlation has been increasingly challenged by detailed observations of galaxies (e.g., Wong & Blitz 2002; Boissier et al. 2003; Heyer et al. 2004; Boissier et al. 2006; Calzetti et al. 2007; Kennicutt et al. 2007).

In this study, we adopt an alternative approach in which empirical and theoretical knowledge of the efficiency of star formation in dense, molecular gas is used as the basis for a star formation model in hydrodynamical simulations of disk galaxy evolution. This approach requires modeling processes that shape properties of the dense phase of the interstellar medium (ISM) in galaxies. The purpose of this paper is to present a model of the ISM and star formation that both accounts for important microphysical processes, including the abundance and destruction of molecular hydrogen, and features a star formation efficiency calibrated on the scale of molecular clouds. The model is used to study how ISM processes operate to affect the star formation efficiency on galactic scales in galaxies of different masses.

Stellar populations in galaxies exhibit salient trends of colors and metallicities with galaxy luminosity (e.g., Kauffmann et al. 2003; Blanton et al. 2005; Cooper et al. 2007). In the hierarchical structure formation scenario these trends should emerge through the process of star formation in the progenitors of present-day galaxies. Observationally, ample evidence suggests that the efficiency of the conversion of gas into stars depends strongly and non-monotonically on mass of the system. For example, the faint-end of the galaxy luminosity function has a shallow slope ($\alpha_L \approx 1.0 - 1.3$, e.g., Blanton et al. 2001, 2003) compared to the steeper mass function of dark matter halos ($\alpha_{\text{DM}} \approx 2$, e.g., Press & Schechter 1974; Sheth & Tormen 1999), indicating a decrease in star formation efficiency in low-mass galaxies. At the same time, the neutral hydrogen (HI) and baryonic mass functions may

¹ Kavli Institute for Cosmological Physics, and Department of Astronomy and Astrophysics, University of Chicago, 933 East 56th Street, Chicago, IL 60637, USA

² Enrico Fermi Institute, 5640 South Ellis Avenue, Chicago, IL 60637, USA

³ Spitzer Fellow

be steeper than the luminosity function ($\alpha_{\text{HI}} \approx 1.3 - 1.5$, e.g., Rosenberg & Schneider 2002; Zwaan et al. 2003) and the baryonic Tully & Fisher (1977) relation is continuous down to extremely low-mass dwarf galaxies (e.g., McGaugh 2005; Geha et al. 2006), indicating that the fractional baryonic content of galaxies of different mass is similar. Hence, low-mass galaxies that are unaffected by environmental processes are gas-rich, yet often form stars inefficiently.

While feedback processes from supernovae and AGN (e.g., Brooks et al. 2007; Sijacki et al. 2007), or the efficiency of gas cooling and accretion (Dekel & Birnboim 2006, 2007), may account for part of these trends, the efficiency of star formation as a function of galaxy mass may also owe to intrinsic ISM processes (e.g., Tassis et al. 2006; Kaufmann et al. 2007). To adequately explore the latter possibility, a realistic model for the conversion of gas into stars in galaxies is needed.

Traditionally, star formation in numerical simulations of galaxy formation is based on the empirical Schmidt-Kennicutt relation (Schmidt 1959; Kennicutt 1989, 1998), in which star formation rate is a *universal* power-law function of the total disk-averaged or global gas surface density: $\Sigma_{\text{SFR}} \propto \Sigma_{\text{gas}}^{n_{\text{tot}}}$ with $n_{\text{tot}} \approx 1.4$ describing the correlation for the entire population of normal and starburst galaxies. However, growing observational evidence indicates that this relation may not be universal on smaller scales within galaxies, especially at low surface densities.

Estimates of the slope of the Schmidt-Kennicutt relation within individual galaxies exhibits significant variations. For example, while Schuster et al. (2007) and Kennicutt et al. (2007) find $n_{\text{tot}} \approx 1.4$ for the molecular-rich galaxy M51a, similar estimates in other large, nearby galaxies (including the Milky Way (MW); Misiriotis et al. 2006) range from $n_{\text{tot}} \approx 1.2$ to $n_{\text{tot}} \approx 3.5$ (Wong & Blitz 2002; Boissier et al. 2003) depending on dust-corrections and fitting methods. The disk-averaged total gas Schmidt-Kennicutt relation for normal (non-starburst) galaxies also has a comparably steep slope of $n_{\text{tot}} \approx 2.4$, with significant scatter (Kennicutt 1998). While the variations in the $\Sigma_{\text{SFR}} - \Sigma_{\text{gas}}$ correlation may indicate systematic uncertainties in observational measurements, intrinsic variations or trends in galaxy properties may also induce differences between the global relation determined by Kennicutt (1998) and the $\Sigma_{\text{SFR}} - \Sigma_{\text{gas}}$ correlation in individual galaxies.

Galaxies with low gas surface densities, like dwarfs or bulgeless spirals, display an even wider variation in their star formation relations. Heyer et al. (2004) and Boissier et al. (2003) show that in low-mass galaxies the star formation rate dependence on the total gas surface density, $\Sigma_{\text{SFR}} \propto \Sigma_{\text{gas}}^{n_{\text{tot}}}$, exhibits a power-law slope $n_{\text{tot}} \approx 2 - 3$ that is considerably steeper than the global Kennicutt (1998) relation slope of $n_{\text{tot}} \approx 1.4$. Further, star formation in the low-surface density outskirts of galaxies also may not be universal. Average star formation rates appear to drop rapidly at gas surface densities of $\Sigma_{\text{gas}} \lesssim 5 - 10 M_{\odot} \text{pc}^{-2}$ (Hunter et al. 1998; Martin & Kennicutt 2001), indicating that star formation may be truncated or exhibit a steep dependence on the gas surface density. The existence of such threshold surface densities have been proposed on theoretical grounds (Kennicutt 1998; Schaye 2004), although recent GALEX results using a UV indicator of star formation suggest that star formation may continue at even lower surface densities (Boissier et al. 2006). Star formation rates probed by damped Lyman alpha absorption (DLA) systems also appear to lie below the Kennicutt

(1998) relation, by an order of magnitude (Wolfe & Chen 2006; Wild et al. 2007), which may indicate that the relation between star formation rate and gas surface density in DLA systems differs from the local relation measured at high Σ_{gas} .

In contrast, observations generally show that star formation in galaxies correlates strongly with *molecular* gas, especially with the highly dense gas traced by HCN emission (Gao & Solomon 2004; Wu et al. 2005). The power-law index of the Schmidt-Kennicutt relation connecting the star formation rate to the surface density of molecular hydrogen consistently displays a value of $n_{\text{mol}} \approx 1.4$ and exhibits considerably less galaxy-to-galaxy variation (Wong & Blitz 2002; Murgia et al. 2002; Boissier et al. 2003; Heyer et al. 2004; Matthews et al. 2005; Leroy et al. 2005, 2006; Gardan et al. 2007). Molecular gas, in turn, is expected to form in the high-pressure regions of the ISM (Elmegreen 1993a; Elmegreen & Parravano 1994), as indicated by observations (Blitz & Rosolowsky 2004, 2006; Gardan et al. 2007).

Analytical models and numerical simulations that tie star formation to the fraction of gas in the dense ISM are successful in reproducing many observational trends (e.g., Elmegreen 2002; Kravtsov 2003; Krumholz & McKee 2005; Li et al. 2005b, 2006; Tasker & Bryan 2006, 2007; Krumholz & Thompson 2007; Wada & Norman 2007; Tassis 2007). Recently, several studies have explored star formation recipes based on molecular hydrogen. Pelupessy et al. (2006) and Booth et al. (2007) implemented models for H_2 formation in gaseous disks and used them to study the molecular content and star formation in galaxies. However, these studies focused on the evolution of galaxies of a single mass and did not address the origin of the Schmidt-Kennicutt relation, its dependence on galaxy mass or structure, or its connection to trends in the local molecular fraction.

Our study examines the Schmidt-Kennicutt relation critically, including its dependence on the structural and ISM properties of galaxies of different masses, to explain the observed deviations from the global Schmidt-Kennicutt relation found by Kennicutt (1998), to investigate other connections between star formation and disk galaxy properties such as rotation or gravitational instability, and to explore how the temperature and density structure of the ISM pertains to the star formation attributes of galaxies.

To these ends, we develop a model for the ISM and star formation whose key premise is that star formation on the scales of molecular clouds (~ 10 pc) is a function of molecular hydrogen density with a universal star formation efficiency per free-fall time (e.g., Krumholz & Tan 2007). Molecular hydrogen, which we assume to be a proxy for dense, star forming gas, is accounted for by calculating the local H_2 fraction of gas as a function of density, temperature, and metallicity using the photoionization code Cloudy (Ferland et al. 1998) to incorporate H_2 -destruction by the UV radiation of local young stellar populations. We devise a numerical implementation of the star formation and ISM model, and perform hydrodynamical simulations to study the role of molecular gas in shaping global star formation relations of self-consistent galaxy models over a representative mass range.

The results of our study show that many of the observed global star formation correlations and trends can be understood in terms of the dependence of molecular hydrogen abundance on the local gas volume density. We show that the physics controlling the abundance of molecular hydrogen and its destruction by the interstellar radiation field play a key role in shaping these correlations, in agreement with ear-

lier calculations based on more idealized models of the ISM (Elmegreen 1993a; Elmegreen & Parravano 1994). While our simulations focus on the connection between the molecular ISM phase and star formation on galactic scales, the formation of molecular hydrogen has also been recently studied in simulations of the ISM on smaller, subgalactic scales (Glover & Mac Low 2007; Dobbs & Bonnell 2007). These simulations are complementary to the calculations presented in our study and could be used as input to improve the molecular ISM model we present.

The paper is organized as follows. The simulation methodology, including our numerical models for the ISM, interstellar radiation field, and simulated galaxies, is presented in §2. The results of the simulations are presented in §3, where the simulated star formation relations in galactic disks and correlations of the molecular fraction with the structure of the ISM are examined. We discuss our results in §4 and conclude with a summary in §5. Details of our tests of numerical fragmentation in disk simulations and calculations of the model scaling between star formation, gas density, and orbital frequency are presented in the Appendices. Throughout, we work in the context of a dark-energy dominated cold dark matter cosmology with a Hubble constant $H_0 \approx 70 \text{ km s}^{-1} \text{ Mpc}^{-1}$.

2. METHODOLOGY

To examine the connection between molecular gas and star formation in disk galaxies, we develop a model that accounts for coolants efficient at low temperatures ($T < 10^4 \text{ K}$), calculates the equilibrium abundance of H_2 in dense gas, and estimates the local star formation rate based on the local H_2 density with a universal star formation efficiency per free fall time. This ISM model is detailed below in §2.1, and is referred to as the $\text{H}_2\text{D-SF}$ model (for “ H_2 density-star formation”). We extend the $\text{H}_2\text{D-SF}$ model to account for the destruction of H_2 by an interstellar radiation field powered by local star formation, and refer to the extended model as the $\text{H}_2\text{D-SF+ISRF}$ model (for “ H_2 density-star formation plus interstellar radiation field”). The $\text{H}_2\text{D-SF+ISRF}$ model is also detailed below in §2.1. The new molecular gas ISM and star formation models are contrasted against a simple ISM model that includes only atomic cooling with a temperature floor $T = 10^4 \text{ K}$ and a star formation rate calculated from the total gas density above a density threshold, which we refer to as the GD-SF model (for “gas density-star formation”). The GD-SF model is very similar to ISM and star formation models commonly used in previous galaxy formation simulations. Each star formation and ISM model is numerically implemented in the smoothed particle hydrodynamics (SPH) / N-body code GADGET2 (Springel et al. 2001; Springel 2005), which is used to perform the simulations presented in this work. General issues of numerical fragmentation in the disk simulations of the kind presented here are described in §2.3, §2.4, and in the Appendix. The ISM models are applied to simulations of the isolated evolution of disk galaxies with a representative range of circular velocities and structural properties. The galaxy models are designed as analogues of the well-studied nearby galaxies DDO154, M33, and NGC 4501, and are detailed in §2.5. The results of the simulations are presented in §3.

2.1. ISM Properties

The thermal properties of the ISM are largely determined by the radiative heating \mathcal{H} and cooling Λ rates of interstellar gas. Given \mathcal{H} and Λ , the rate of change of the internal energy

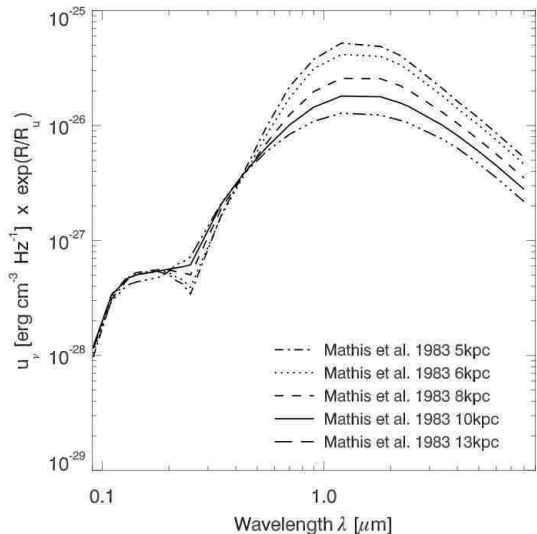


FIG. 1.— Local interstellar radiation field (ISRF) energy density u_ν in the Milky Way (Mathis et al. 1983), scaled by the exponential decrease of stars in the Galactic disk with radius. Shown are the values of u_ν in the model of Mathis et al. (1983) for galactocentric radii of $R = 5 \text{ kpc}$ (dash dotted line), $R = 6 \text{ kpc}$ (dotted line), $R = 8 \text{ kpc}$ (thin dashed line), $R = 10 \text{ kpc}$ (thick solid line), and $R = 13 \text{ kpc}$ (dash double-dotted line). Note that Mathis et al. (1983) adopt a solar radius of $R_\odot = 10 \text{ kpc}$. When normalized to a common density of stars by their exponential scale length $R_u = 4 \text{ kpc}$, the short-wavelength portion of the ISRF is similar throughout the disk. In our simulations, we adopt the spectral form of the ISRF at the solar radius and scale the intensity by the local star formation rate surface density normalized by the star formation rate surface density in the solar neighborhood of $\Sigma_{\text{SFR},\odot} \approx 4 \times 10^{-9} M_\odot \text{ yr}^{-1} \text{ pc}^{-2}$.

u of gas with a density ρ_g evolves as

$$\rho_g \frac{du}{dt} = \mathcal{H} - \Lambda, \quad (1)$$

with additional terms to describe the energy input from feedback or hydrodynamical interactions. The temperature dependence of \mathcal{H} and Λ will depend on the metallicity and density of gas, and on the nature of the external radiation field. For the atomic cooling processes of hydrogen and helium, the contributions to Λ from collisional ionization, recombination, dielectronic recombination, collisional excitation, bremsstrahlung, and the Compton effect can be expressed succinctly (e.g., Dalgarno & McCray 1972; Black 1981; Ikeuchi & Ostriker 1986; Cen 1992; Katz et al. 1996). Simulations of H_2 cooling and interest in its role in structure formation have developed recently (Anninos & Norman 1996; Ostriker & Gnedin 1996; Abel et al. 1997; Nakamura & Umemura 2001; Ricotti et al. 2001; Machacek et al. 2001; Yoshida et al. 2003, 2006; Kuhlen & Madau 2005; O’Shea & Norman 2007; Smith et al. 2007), although earlier simulations considered molecular hydrogen coolants in other contexts (e.g., Struck-Marcell 1982; Monaghan & Lattanzio 1991). The calculation of non-hydrogenic atomic processes, even at high temperatures, can be considerably more complicated (Cox & Tucker 1969; Raymond et al. 1976; Sutherland & Dopita 1993).

To calculate the above heating and cooling processes in ISM gas, as well as additional cooling processes from molecules and ionic species other than H_2 , we use the photoionization code Cloudy version C06.02a, last described by Ferland et al. (1998). Cloudy calculates a variety of heating and cooling processes for H, He, and metals, including all the processes noted above as well as absorption by dust grains, photoelectric absorption, and molecular photoab-

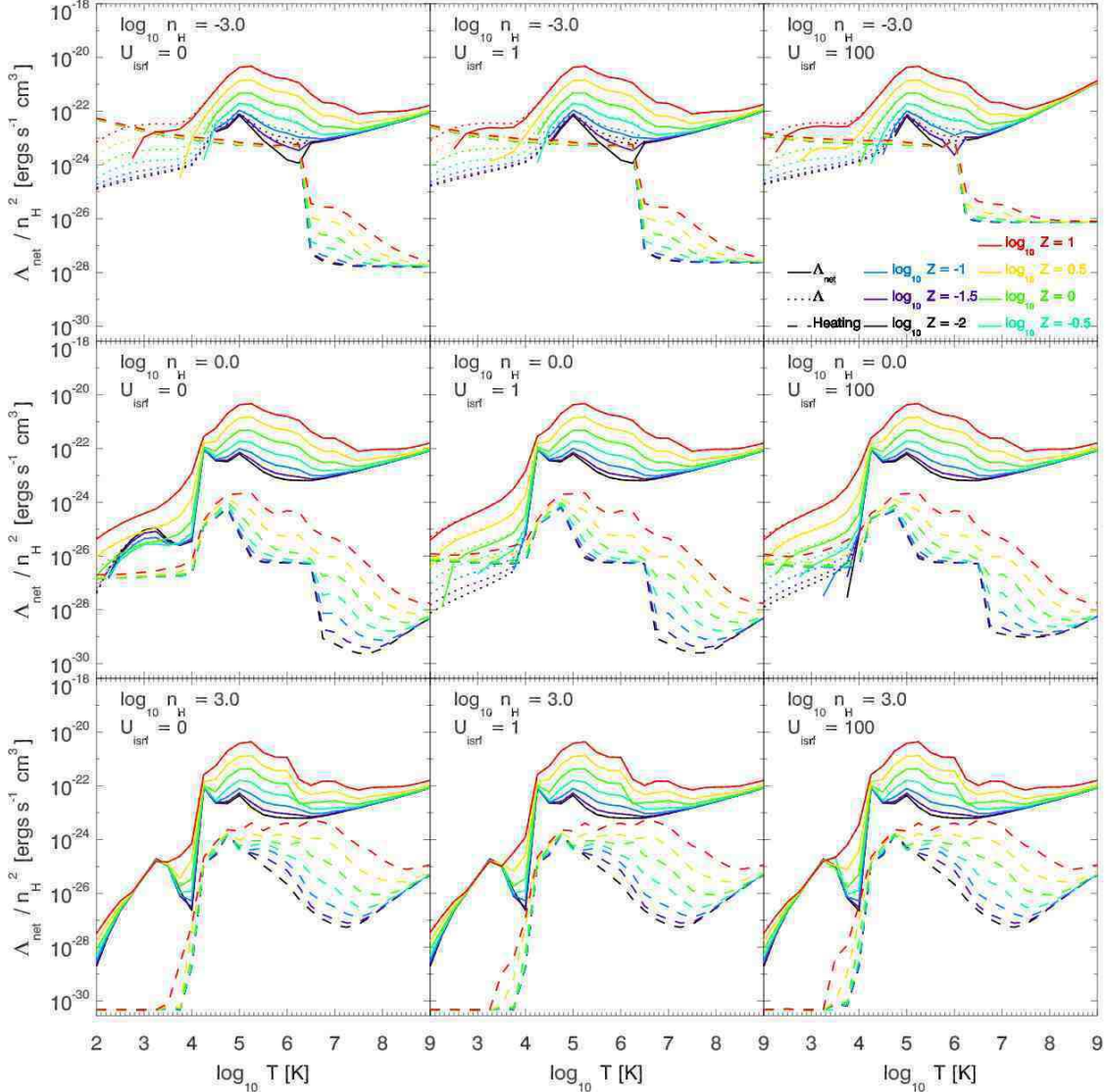


FIG. 2.— Cooling (Λ) and heating (\mathcal{H}) rates for interstellar and intergalactic gas as a function of gas density (n_{H}), temperature (T), metallicity (Z), and interstellar radiation field (ISRF) strength (U_{isrf}), in units of the ISRF strength in the MW at the solar circle, as calculated by the code Cloudy (Ferland et al. 1998). Shown are the cooling (dotted lines), heating (dashed lines) and net cooling (solid) functions over the temperature range $T = 10^2 - 10^9$ K. Dense gas can efficiently cool via atomic and molecular coolants below $T = 10^4$ K, depending on the gas density and the strength of the ISRF. A strong ISRF can enable the destruction of H_2 gas and thereby reduce the star formation rate.

sorption. The chemical network and cooling calculated by Cloudy includes the molecules and atomic ions that allow gas to cool to temperatures $T < 10^4$ K. For details on the molecular network and cooling, the reader is encouraged to examine Hollenbach & McKee (1979, 1989), Ferland et al. (1998), and the Cloudy documentation suite Hazy⁴.

The heating term \mathcal{H} can include a variety of physical effects. Our Cloudy calculations include heating from the cosmic ultraviolet background at $z = 0$ following Haardt & Madau (1996), extended to include the contribution to the UV background from galaxies (see the Cloudy documentation for details). Cosmic ray heating is also incorporated following Ferland & Mushotzky (1984), but it is only the dominant source of ionization at densities where the ISM becomes optically-thick to UV radiation. The presence of a blackbody cosmic microwave background radiation

with a temperature of $T \approx 2.7$ K is included. Milky Way-like ($R_V = 3.1$) dust, including both graphite and silicate dust, is modeled with the local ISM abundance. Grain heating and cooling mechanisms are included, following van Hoof et al. (2001) and Weingartner & Draine (2001).

The $\text{H}_2\text{D-SF}$ model of the ISM includes all the cooling and heating processes described above. We can extend this model by including a prescription for heating and H_2 -destruction from an interstellar radiation field (ISRF) powered by young stars. The $\text{H}_2\text{D-SF+ISRF}$ model includes the following treatment of the ISRF, and is used to examine the consequences of soft UV radiation from star formation for the molecular phase of the ISM.

Mathis et al. (1983) modeled the ISRF needed to power the emission spectrum of dust both in the diffuse ISM and in molecular clouds in the Milky Way. The short-wavelength ($\lambda \lesssim 0.3 \mu\text{m}$) ISRF spectral energy distribution was inferred to scale roughly exponentially with a scale length $R_{\text{it}} \sim 4$ kpc in

⁴ <http://www.nublado.org>

the MW disk (for a solar galactocentric radius of $R_\odot = 10$ kpc), tracing the stellar population, while the strength of the long-wavelength ISRF SED varied non-trivially with radius owing to the relative importance of emission from graphite and silicate grains. Figure 1 shows the ISRF spectral energy density determined by Mathis et al. (1983) (adapted from their Table A3) for $R = 0.5 - 1.3R_\odot$, normalized to a fixed stellar surface density. As Figure 1 demonstrates, the spectral shape of the short-wavelength ISRF is roughly independent with radius. This shape is similar to the radiation field considered by Draine (1978) and Draine & Bertoldi (1996). For simplicity, we fix the ISRF spectrum to have its inferred spectral shape in the solar vicinity (Figure 1, solid line) and scale the intensity with the local star formation rate density normalized by the solar value as

$$U_{\text{isrf}} \equiv \frac{u_\nu}{u_{\nu,\odot}} = \frac{\Sigma_{\text{SFR}}}{\Sigma_{\text{SFR},\odot}} \quad (2)$$

where $\Sigma_{\text{SFR},\odot} \approx (2-5) \times 10^{-9} M_\odot \text{ yr}^{-1} \text{ pc}^{-2}$ (e.g., Smith et al. 1978; Miller & Scalo 1979; Talbot 1980; Rana 1987, 1991; Kroupa 1995). For our model, we adopt $\Sigma_{\text{SFR},\odot} = 4 \times 10^{-9} M_\odot \text{ yr}^{-1} \text{ pc}^{-2}$. The calculation of the star formation rate, Σ_{SFR} , is described in §2.2. When included, the ISRF is simply added to the input spectrum for the Cloudy calculations as an additional source of radiation.

While the ionization potential of atomic hydrogen (13.6eV) is lower than the direct destruction (14.7eV) and photoionization continuum (15.4eV) thresholds of H_2 (Spitzer 1948), absorption by soft UV ($\lambda \sim 0.1 \mu\text{m}$) photons can enable the destruction of H_2 through transitions to the vibrational continuum or to excited states that can be photoionized or photodissociated (Stecher & Williams 1967). The ISRF can supply the soft UV photons that lead to H_2 dissociation and can subsequently regulate the H_2 abundance at low gas densities ($n_{\text{H}} \sim 1 \text{ cm}^{-3}$). For values of $U_{\text{isrf}} \gtrsim 0.1$, the ISRF dominates over the Haardt & Madau (1996) UV background.

Figure 2 shows the cooling rate Λ (dotted line), the heating rate \mathcal{H} (dashed line), and net cooling rate Λ_{net} (solid lines) calculated for a range of temperatures (T), densities (n_{H}), metallicities (Z), and ISRF strengths (U_{isrf}). For each value of T , n_{H} , Z , and U_{isrf} a Cloudy simulation is performed assuming a plane-parallel radiation field illuminating a 10 pc thick slab chosen to be comparable to our hydrodynamical spatial resolution. Each simulation is allowed to iterate until convergence, after which the heating rate, cooling rate, ionization fraction, molecular fraction, electron density, and molecular weight is recorded from the center of the slab. These quantities are tabulated on a grid over the range $\log_{10} T = \{2, 9\} \log_{10} \text{ K}$ with $\Delta \log_{10} T = 0.25$, $\log_{10} n_{\text{H}} = \{-6, 6\} \log_{10} \text{ cm}^{-3}$ with $\Delta \log_{10} n_{\text{H}} = 1.5$, $\log_{10} Z = \{-2, 1\} \log_{10} Z_\odot$ with $\Delta \log_{10} Z = 1.5$, and $U_{\text{isrf}} = \{0, 1, 10, 100, 1000\} U_{\text{isrf},\odot}$, and log-linearly interpolated according to the local gas properties. The left panels of Figure 2 with $U_{\text{isrf}} = 0$ correspond to net cooling functions used in the $\text{H}_2\text{D-SF}$ model, while the $\text{H}_2\text{D-SF+ISRF}$ model includes all the net cooling functions presented in the figure. The GD-SF model that includes only atomic cooling incorporates the regions of the net cooling functions in the left ($U_{\text{isrf}} = 0$) panels of Figure 2 at temperatures $T > 10^4 \text{ K}$. In addition to well known cooling and heating processes operating at high temperatures ($T > 10^4 \text{ K}$), the results of the Cloudy simulations show that cooling of gas near $n_{\text{H}} \sim 1 \text{ cm}^{-3}$ is regulated by the presence of the ISRF (Figure 2, middle left and center panels) and an ISRF strength of $U_{\text{isrf}} \sim 1$ contributes a

low-temperature heating rate \mathcal{H} an order of magnitude larger than the cosmic UV background. At much higher densities ($n_{\text{H}} \sim 10^3 \text{ cm}^{-3}$), the gas remains optically-thin to cosmic ray heating but becomes insensitive to the presence of either the ISRF or the cosmic UV background. We note that the correlation between the ISRF field strength and the local star formation rate limits the applicability of the low- n_{H} / high- U_{isrf} region of the cooling function but we include such regimes for completeness.

2.2. Star Formation and Feedback

Modeling the star formation rate in the ISM as a power-law function of the gas density ρ_{g} dates to at least Schmidt (1959), who modeled the past star formation rate of the Galaxy needed to produce the observed luminosity function of main sequence stars. We adopt the model that star formation occurs in molecular clouds in proportion to the local molecular gas density $f_{\text{H}_2} \rho_{\text{g}}$, as suggested by a variety of observations (e.g., Elmegreen & Lada 1977; Blitz & Thaddeus 1980; Beichman et al. 1986; Lada 1987; Young & Scoville 1991). The model thus assumes that H_2 is a good proxy for star forming gas.

On the scale of individual gas particles the star formation is then determined by the density of molecular hydrogen, which is converted into stars on a time scale t_* : $\rho_* \propto f_{\text{H}_2} \rho_{\text{g}} / t_*$. Observations indicate that at high densities t_* scales with the local free fall time of the gas, $t_{\text{ff}} \propto \rho_{\text{g}}^{-0.5}$, as

$$t_* \approx t_{\text{ff}} / \epsilon_{\text{ff}}, \quad (3)$$

with the star formation efficiency per free fall time, $\epsilon_{\text{ff}} \approx 0.02$, approximately independent of density at $n \approx 10^2 - 10^4 \text{ cm}^{-3}$ (Krumholz & McKee 2005; Krumholz & Tan 2007).

We adopt $t_* = 1 \text{ Gyr}$ for gas at density $n_{\text{H}} = 10 h^2 \text{ cm}^{-3}$ ($t_{\text{ff}} = 2.33 \times 10^7 \text{ yrs}$), which corresponds to $\epsilon_{\text{ff}} = 0.023$. By calibrating the star formation efficiency to observations of dense molecular clouds through ϵ_{ff} , our model differs from the usual approach of choosing gas consumption time scale to fit the global star formation rate and the Schmidt-Kennicutt relation in galaxies. As we show below, the chosen efficiency results in global star formation rate for the entire galaxies consistent with observations (see §3).

Incorporating the assumption that a mass fraction β of young stars promptly explode as supernovae, the star formation rate in our models is given by

$$\dot{\rho}_* = (1 - \beta) f_{\text{H}_2} \frac{\rho_{\text{g}}}{t_*} \left(\frac{n_{\text{H}}}{10 h^2 \text{ cm}^{-3}} \right)^{0.5}. \quad (4)$$

We assume $\beta \approx 0.1$, appropriate for the Salpeter (1955) initial mass function. Implicit in Equation 4 is that the molecular fraction f_{H_2} may vary with a variety of local ISM properties as

$$f_{\text{H}_2} = f_{\text{H}_2}(\rho_{\text{g}}, T, Z_{\text{g}}, U_{\text{isrf}}). \quad (5)$$

The $\text{H}_2\text{D-SF}$ model includes the dependence on the gas density, temperature T , metallicity Z_{g} . The $\text{H}_2\text{D-SF+ISRF}$ model additionally includes the dependence of the molecular fraction on the strength of the interstellar radiation field U_{isrf} parameterized as a fraction of the local interstellar field energy density. In both the $\text{H}_2\text{D-SF}$ and $\text{H}_2\text{D-SF+ISRF}$ models, the equilibrium molecular fraction is tabulated by using the Cloudy calculations discussed in §2.1. Variations in the cosmic ray ionization rate or the dust model could affect the form of Equation 5 but we do not consider them here. For the simple GD-SF model that does not track the molecular

gas abundance, we set $f_{\text{H}_2} = 1$ in gas with densities above the star formation threshold density $n_{\text{H}} \gtrsim 0.1 \text{cm}^{-3}$ (see, e.g., Governato et al. 2007).

Figure 2 shows that the feature in the cooling rate at $T \sim 10^3$ K for low metallicity, intermediate density gas (e.g., middle left panel), which owes to molecular hydrogen, disappears in the presence of the interstellar radiation field (see also Figure 5). Equations 1 and 4 then imply that destruction of H_2 by soft UV photons from young stars regulates star formation in the $\text{H}_2\text{D-SF+ISRF}$ model. The dissociation of H_2 by the ISRF means that ISM gas may be cold and dense but its SFR may be suppressed if the local ISRF is strong. We discuss this effect in the context of the simulated galaxy models in §3.

The energy deposition from supernovae into interstellar gas is treated as a thermal feedback, given by

$$\rho_{\text{g}} \frac{du}{dt} = \epsilon_{\text{SN}} \dot{\rho}_{\star} \quad (6)$$

where ϵ_{SN} is the energy per unit mass of formed stars that is deposited into the nearby ISM. We choose $\epsilon = 1.4 \times 10^{49} \text{ergs } M_{\odot}^{-1}$ or, in the language of Springel & Hernquist (2003b), an effective supernovae temperature of $T_{\text{SN}} = 3 \times 10^8$. This value for the energy deposition for supernovae has been used repeatedly in simulations of galaxy mergers (e.g., Robertson et al. 2006a,b,c). Given that extremely short cooling time of dense gas at low resolutions, prescribing supernovae feedback as thermal input into the gas has long been known to have a weak effect on the global evolution of simulated galaxies (e.g., Katz 1992; Steinmetz & Müller 1995). For this reason, the results of this paper also do not depend strongly on the value of ϵ_{SN} or the supernovae mass fraction β . Metal enrichment of the ISM is treated in the instantaneous approximation, with a mass fraction $y = 0.02$ of the supernovae ejecta being returned into the gas as metals (see Springel & Hernquist 2003a).

2.3. Avoiding Numerical Jeans Fragmentation

Perturbations in a self-gravitating medium of mean density ρ and sound speed c_s can grow only if their wavelength exceeds the Jeans length λ_{Jeans} (Jeans 1928). The corresponding Jeans mass contained within λ_{Jeans} is

$$m_{\text{Jeans}} = \frac{\pi^2 c_s^3}{6G^{3/2} \rho^{1/2}} \quad (7)$$

(see, e.g., §5.1.3 of Binney & Tremaine 1987). Bate & Burkert (1997) identified a resolution requirement for smoothed particle hydrodynamics simulations such that the number of SPH neighbors N_{neigh} and gas particle mass m_{gas} should satisfy $2N_{\text{neigh}}m_{\text{gas}} < m_{\text{Jeans}}$ to capture the pressure forces on the Jeans scale and avoid numerical fragmentation. Klein et al. (2004) suggest that the effective resolution of SPH simulations is the number of SPH smoothing lengths per Jeans scale

$$h_{\text{Jeans}} = \frac{\pi^{5/2} c_s^3}{6G^{3/2} N_{\text{neigh}} m_{\text{gas}} \rho^{1/2}}, \quad (8)$$

which is very similar to the number of Jeans masses per SPH kernel mass, if we define the kernel mass as

$$m_{\text{SPH}} \equiv \sum_{i=1}^{N_{\text{neigh}}} m_i. \quad (9)$$

Our simulations include low temperature coolants that allow ISM gas to become cold and dense, and for the typical number

of gas particles used in our models ($N_{\text{gas}} \approx 400,000$) the Jeans mass is not resolved at the lowest temperatures and largest galaxy masses. Motivated by techniques used to avoid numerical Jeans fragmentation in grid codes (e.g., Machacek et al. 2001), a density-dependent pressure floor is introduced into our SPH calculations. For every gas particle, the kernel mass is monitored to ensure it resolves some number N_{Jeans} of Jeans masses. If not, the particle internal energy is altered following

$$u = u \times \begin{cases} \left(\frac{N_{\text{Jeans}}}{h_{\text{Jeans}}} \right)^{2/3} & : h_{\text{Jeans}} < N_{\text{Jeans}} \\ \left(\frac{2N_{\text{Jeans}}m_{\text{SPH}}}{m_{\text{Jeans}}} \right)^{2/3} & : m_{\text{Jeans}} < 2N_{\text{Jeans}}m_{\text{SPH}} \end{cases}, \quad (10)$$

to provide the largest local pressure and to assure the local Jeans mass is resolved. We discuss the purpose and effect of this pressurization in more detail in the first Appendix, but we note that this requirement scales with the resolution and naturally allows for better-resolved SPH simulations to follow increasingly lower temperature gas. For the simulation results presented in this paper, we use $N_{\text{Jeans}} = 15$, which is larger than the effective $N_{\text{Jeans}} = 1$ used by Bate & Burkert (1997). We have experimented with simulations with $N_{\text{Jeans}} = 1 - 100$ and find $N_{\text{Jeans}} \sim 15$ to provide sufficient stability over the time evolution of the simulations for the structure of galaxy models we use. Other simulations may require different values N_{Jeans} or a different pressurization than the $u \propto m_{\text{Jeans}}^{-2/3}$ scaling suggested by Equation 7.

2.4. Median Equation-of-State

In the absence of a numerical pressure floor, the equation-of-state (EOS) of gas will follow the loci where heating balances cooling in the temperature-density phase space. For treatments of atomic H and He cooling dense gas will be roughly isothermal at $T \approx 10^4 \text{K}$, but more generally the gas will have an average density-dependent temperature. However, the gas pressurization requirements to avoid numerical Jeans fragmentation change the EOS of the gas. For purposes of calculating the molecular or ionization fraction of dense ISM gas that has been numerically pressurized, an estimate of the EOS in the absence of resolution restraints is required. Figure 3 shows the temperature-density phase diagram of ISM gas in a simulation of a Milky Way-sized galaxy without using the SPH pressure floor described in §2.3 and detailed in the Appendix.

The median EOS of this gas, determined by the heating and cooling processes calculated by the Cloudy code for a given density, temperature, metallicity, and interstellar radiation field strength, is used in our simulations to assign an effective temperature to dense gas pressurized at the Jeans resolution limit of the simulation. Similarly, the molecular fraction of the numerically-pressurized gas must be assigned at densities that exceed resolution limit of the simulations. As Figure 3 indicates, the transition between the warm phase at densities $n_{\text{H}} \lesssim 1 \text{cm}^{-3}$ and the cold phase at densities $n_{\text{H}} \gtrsim 30 \text{cm}^{-3}$ is rapid (see also Wolfire et al. 2003). The required pressure floor can artificially limit the density of gas to the range $n_{\text{H}} \lesssim 30 \text{cm}^{-3}$ where, in the presence of an ISRF, the molecular fraction of the gas would be artificially suppressed (without an ISRF, even gas at $n_{\text{H}} \approx 1 \text{cm}^{-3}$ is already mostly molecular and would be relatively unaffected, see §3.1.1). To account for this numerical limitation, gas at densities $n_{\text{H}} > 1 \text{cm}^{-3}$ that is numerically-pressurized to resolve the Jeans scale is assigned a minimum molecular fraction according to the median EOS and the high-density ($n_{\text{H}} > 30 \text{cm}^{-3}$) $f_{\text{H}_2} - n_{\text{H}}$ trend of gas in

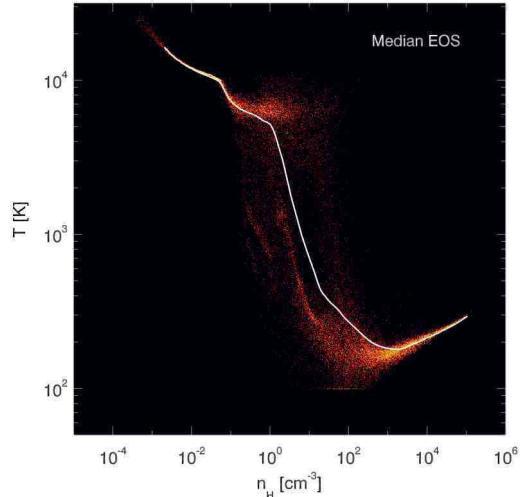


FIG. 3.— Median equation-of-state (EOS) of gas in a Milky Way-sized galactic disk in our ISM model. Shown is the histogram of particles in the hydrogen number density n_{H} – temperature T plane and the median temperature measured in bins of density (white line). The median EOS is used to determine the properties of gas pressurized to avoid numerical Jeans fragmentation (see §2.3 and §2.4). At high densities, the particles follow the loci where heating balances cooling for their densities, temperatures, metallicities, and local interstellar radiation field strengths.

the absence of the pressure floor. The $f_{\text{H}_2} - n_{\text{H}}$ relation calculated by Cloudy can be modeled for pressurized gas in this regime as $0.67 (\log_{10} n_{\text{H}} + 1.5) - 1 \lesssim f_{\text{H}_2} \leq 1$. The utilization of the median EOS to assign detailed properties to the dense gas in this manner has the further benefit of adaptively scaling with the local resolution, allowing an approximation of the ISM properties that improves with an increase in the particle number used in a simulation. Throughout the paper, when simulation results include gas particles that are pressurized to avoid numerical Jeans fragmentation, their reported temperatures and molecular fractions are determined from the median EOS presented in Figure 3.

2.5. Isolated Galaxy Models

We use three cosmologically-motivated galaxy models to study global star formation relations. Below we describe the models and list the observational data used to motivate their adopted structure.

The initialization of the galaxy initial conditions follows the methodology described by Springel et al. (2005), with a few exceptions. The properties of the disks are chosen to be representative of disk galaxies that form within the CDM structure formation paradigm (e.g., Mo et al. 1998). The model galaxies consist of a Hernquist (1990) dark matter halo, exponential stellar and gaseous disks with scale lengths $R_{\text{d},*}$ and $R_{\text{d},g}$, and an optional Hernquist (1990) stellar bulge with scale radius $a_{\text{b},*}$. For a given virial mass, the Hernquist (1990) dark matter halo parameters are scaled to an effective Navarro et al. (1996) halo concentration. The velocity distributions of the dark matter halos are initialized from the isotropic distribution function provided in Hernquist (1990), using the rejection technique described by Press et al. (1992). The vertical distribution of the stellar disk is modeled with a $\text{sech}^2(z/2z_{\text{d}})$ function with $z_{\text{d}} = 0.2 - 0.3R_{\text{d},*}$. The stellar disk velocity field is initialized by using a Gaussian with the local velocity dispersion σ_z^2 determined from the potential and density via the

Jeans equations. The stellar disk rotational velocity dispersion and streaming velocity are set with the epicyclical approximation (see §3.2.3 and §4.2.1(c) of Binney & Tremaine 1987). The bulge velocity field is also modeled by a Gaussian with a velocity dispersion determined from the Jeans equations but with no net rotation. The gas disk is initialized as an isothermal medium of temperature of $T = 10^4 \text{K}$ in hydrostatic equilibrium with the total potential, including the disk self-gravity, which determines vertical distribution of the gas self-consistently (see Springel et al. 2005). The gravitational softening lengths for the dark matter and baryons are set to $\epsilon_{\text{DM}} = 100h^{-1} \text{pc}$ and $\epsilon_{\text{baryon}} = 50h^{-1} \text{pc}$, respectively.

The galaxy models are designed to roughly match the observed rotation curves, and HI, H_2 , and stellar surface mass distributions of DDO154 ($v_{\text{circ}} \approx 50 \text{km s}^{-1}$), M33 ($v_{\text{circ}} \approx 125 \text{km s}^{-1}$), and NGC4501 ($v_{\text{circ}} \approx 300 \text{km s}^{-1}$). These systems cover a wide range in circular velocity, gas fractions, disk scale lengths, molecular gas fractions, gas surface densities, and gas volume densities. The parameters of the galaxy models are provided in Table 1.

2.5.1. DDO 154 Analogue

DDO 154 is one of the most gas rich systems known and therefore provides unique challenges to models of the ISM in galaxies. For the DDO 154 galaxy analogue, we used the Carignan & Beaulieu (1989) HI map and rotation curves as the primary constraint on the mass distribution. The total gas mass is $M_{\text{d},g} \approx 2.7 \times 10^8 h^{-1} M_{\odot}$ (Carignan & Beaulieu 1989; Hunter & Elmegreen 2004). The stellar disk mass has been estimated at $M_{\text{d},*} \approx 3.4 \times 10^6 h^{-1} M_{\odot}$ (Lee et al. 2006) with a scale length of about $R_{\text{d},*} \approx 0.38h^{-1} \text{kpc}$ at $\lambda = 3.6 \mu\text{m}$. The gaseous disk scale length was determined by approximating the HI surface density profile, with $R_{\text{d},g} \approx 1.52^{-1} \text{kpc}$ providing a decent mimic of the HI data. These numbers are similar to those compiled by McGaugh (2005) for DDO 154 and, combined with the dark matter virial velocity $V_{200} = 50 \text{km s}^{-1}$ and concentration $c = 6$, produce a rotational velocity of $v_{\text{circ}} \approx 50 \text{km s}^{-1}$ (where v_{circ} is defined as the maximum of rotation velocity profile) similar to the value of $v_{\text{circ}} \approx 54 \text{km s}^{-1}$ reported by Karachentsev et al. (2004).

2.5.2. M33 Analogue

The nearby spiral M33 has well measured stellar, HI, H_2 , and SFR distributions, and serves nicely as an example disk galaxy with an intermediate rotational velocity. For the M33 galaxy analogue, we used the Heyer et al. (2004) HI and H_2 map as guidance for determining the gas distribution with a total gas mass of $M_{\text{d},g} \approx 1.68 \times 10^9 h^{-1} M_{\odot}$ (Corbelli 2003; Heyer et al. 2004). According to this data, the gas disk scale length is roughly $R_{\text{d},g} \approx 2.7h^{-1} \text{kpc}$. We set the total stellar disk mass to $M_{\text{d},*} \approx 2.6 \times 10^9 h^{-1} M_{\odot}$ to match the total baryonic mass of $M_{\text{baryon}} \approx 4.3 \times 10^9 h^{-1} M_{\odot}$ reported by McGaugh (2005), and set the disk scale length to $R_{\text{d},*} \approx 0.9h^{-1} \text{kpc}$. These numbers are similar to those compiled by McGaugh (2005) for M33 and, combined with the dark matter virial velocity $V_{200} = 100 \text{km s}^{-1}$ and concentration $c = 10$, produce a rotational velocity of $v_{\text{circ}} \approx 125 \text{km s}^{-1}$.

2.5.3. NGC 4501 Analogue

The massive spiral NGC 4501 is a very luminous disk galaxy ($M_K = -25.38$, Möllenhoff & Heidt 2001) that is gas poor by roughly a factor of ~ 3 for its stellar mass (Giovanelli & Haynes 1983; Kenney & Young 1989;

TABLE 1
 GALAXY MODELS

Structural Parameters									
Galaxy Analogue	V_{200} km s $^{-1}$	v_{circ} km s $^{-1}$	c	M_{disk} $h^{-1}M_{\odot}$	f_{gas}	$R_{\text{d},*}$ $h^{-1}\text{kpc}$	$R_{\text{d,g}}$ $h^{-1}\text{kpc}$	M_{bulge} $h^{-1}M_{\odot}$	$a_{\text{b},*}$ $h^{-1}\text{kpc}$
DDO 154	50	50	6	2.91×10^8	0.99	0.38	1.52
M33	100	125	10	4.28×10^9	0.40	0.98	2.94
NGC 4501	180	300	14	1.02×10^{11}	0.04	3.09	2.16	1.14×10^{10}	0.62
Numerical Parameters									
Galaxy Analogue	N_{DM}	$N_{\text{d},*}$	$N_{\text{d,g}}$	N_{bulge}	ϵ_{DM} $h^{-1}\text{kpc}$	ϵ_{baryon} $h^{-1}\text{kpc}$	N_{neigh}	$N_{\text{neigh}}m_{\text{gas}}$ $h^{-1}M_{\odot}$	Data Refs.
DDO 154	120000	20000	400000	...	0.1	0.05	64	6.51×10^5	1,2,3,4,5
M33	120000	120000	400000	...	0.1	0.05	64	2.74×10^5	5,6,7
NGC 4501	120000	177600	400000	22400	0.1	0.05	64	4.60×10^4	8,9,10,11,12

REFERENCES. — (1) Carignan & Beaulieu (1989); (2) Hunter & Elmegreen (2004); (3) Hunter et al. (2006); (4) Lee et al. (2006); (5) McGaugh (2005); (6) Corbelli (2003); (7) Heyer et al. (2004); (8) Wong & Blitz (2002); (9) Möllenhoff & Heidt (2001) (10) Guhathakurta et al. (1988); (11) Rubin et al. (1999); (12) Boissier et al. (2003)

Blitz & Rosolowsky 2006), and serves as an extreme contrast to the dwarf galaxy DDO 154. To construct an analogue to NGC 4501, we used the rotation curve data compiled by Boissier et al. (2003) from the observations of Guhathakurta et al. (1988) and Rubin et al. (1999) as a guide for designing the potential. The stellar disk scale length $R_{\text{d},*} \approx 3.1 h^{-1}\text{kpc}$ and bulge-to-disk ratio $M_{\text{bulge}}/M_{\text{disk}} = 0.112$ were taken from the K -band observations of Möllenhoff & Heidt (2001), and the total stellar mass was chosen to be consistent with the Bell & de Jong (2001) K -band Tully-Fisher relation. The gas distribution was modeled after the surface mass density profile presented by Wong & Blitz (2002). These structure properties, combined with a virial velocity $V_{200} = 180 \text{ km s}^{-1}$ and dark matter concentration $c = 14$, provide a circular velocity of $v_{\text{circ}} \approx 300 \text{ km s}^{-1}$ appropriate for approximating the observed rotation curve.

3. RESULTS

The isolated evolution of each of the three disk galaxy models is simulated for $t = 1.0 \text{ Gyr}$ using the three separate ISM and star formation models described in §2: the model H₂D-SF with H₂-based star formation, the model H₂D-SF+ISRF which in addition includes the gas heating by local interstellar radiation, and the GD-SF model with a $T = 10^4 \text{ K}$ temperature floor and constant threshold density for star formation. In all cases, the ISM of galaxies is assumed to have initial metallicity of $10^{-2} Z_{\odot}$ and is self-consistently enriched by supernovae during the course of simulation.

Below, the evolution of each galaxy and ISM model is examined in detail. Galactic structure, molecular gas content, and star formation histories are examined in §3.1. The Schmidt-Kennicutt relations describing the correlation between star formation surface density and gas surface densities are examined in §3.2. The relation between the local ISM pressure, the interstellar radiation field, and the molecular fraction is detailed in §3.3. The correlation between the star formation rate, gas surface density, and disk angular frequency is explored in §3.4, and the possible role of critical surface densities in regulating star formation is examined in §3.5. The density and temperature structure of the ISM and their relation to star formation are presented in §3.6.

3.1. Galactic Structure and Evolution

The gas distributions in the simulated disk galaxies after $t = 0.3 \text{ Gyr}$ of evolution in isolation are shown in Figure 4. The image intensity reflects the disk surface density while the color indicates the local mass-weighted temperature of the ISM. A variety of structural properties of the galaxies are evident from the images, including ISM morphologies qualitatively similar to those observed in real galaxies. Almost every disk model is globally stable over gigayear time-scales, excepting only the H₂D-SF model for the $v_{\text{circ}} = 50 \text{ km s}^{-1}$ galaxy. The fragmentation in the H₂D-SF / $v_{\text{circ}} = 50 \text{ km s}^{-1}$ model is resolved and owes to the large cold gas reservoir that becomes almost fully molecular in the absence of H₂-destruction (see §3.2.1 and §3.2.2 for further discussion of fragmentation in this model).

The runs with $T < 10^4 \text{ K}$ coolants develop spiral structure and bar-like instabilities during their evolution. The detailed structures of the spiral patterns and bar instabilities are likely influenced by numerical fluctuations in the potential, but they illustrate the role of spiral structure in the ISM of real galaxies. As the ISM density is larger in these structures, their molecular fraction is higher and gas temperature is lower compared with the average disk properties. The higher molecular fractions in the spiral arms imply that they will also be sites of enhanced star formation in our ISM model, similar to real galaxies.

The small-mass systems evolved with the GD-SF model are more diffuse and have less structure than those evolved with low-temperature coolants, owing to the higher ($T > 10^4 \text{ K}$) ISM temperature (and hence pressure) in high-density regions. The diffuse morphologies of low-mass galaxies in the GD-SF and H₂D-SF+ISRF models owe to the abundance of warm atomic gas with thermal energy comparable to the binding energy of the gas. The tendency of low-mass galaxy disks to be more diffuse and extended than more massive systems owing to inefficient cooling was shown by Kravtsov et al. (2004) and Tassis et al. (2006) to successfully reproduce the faint end of the luminosity function of galactic satellites and scaling relations of dwarf galaxies. Kaufmann et al. (2007) used hydrodynamical simulations of the dissipative formation of disks to demonstrate that the temperature floor of $T = 10^4 \text{ K}$ results in the equilibrium disk scale height-to-scale length ratio in systems with $v_{\text{circ}} \sim 40 \text{ km s}^{-1}$ to be roughly three times

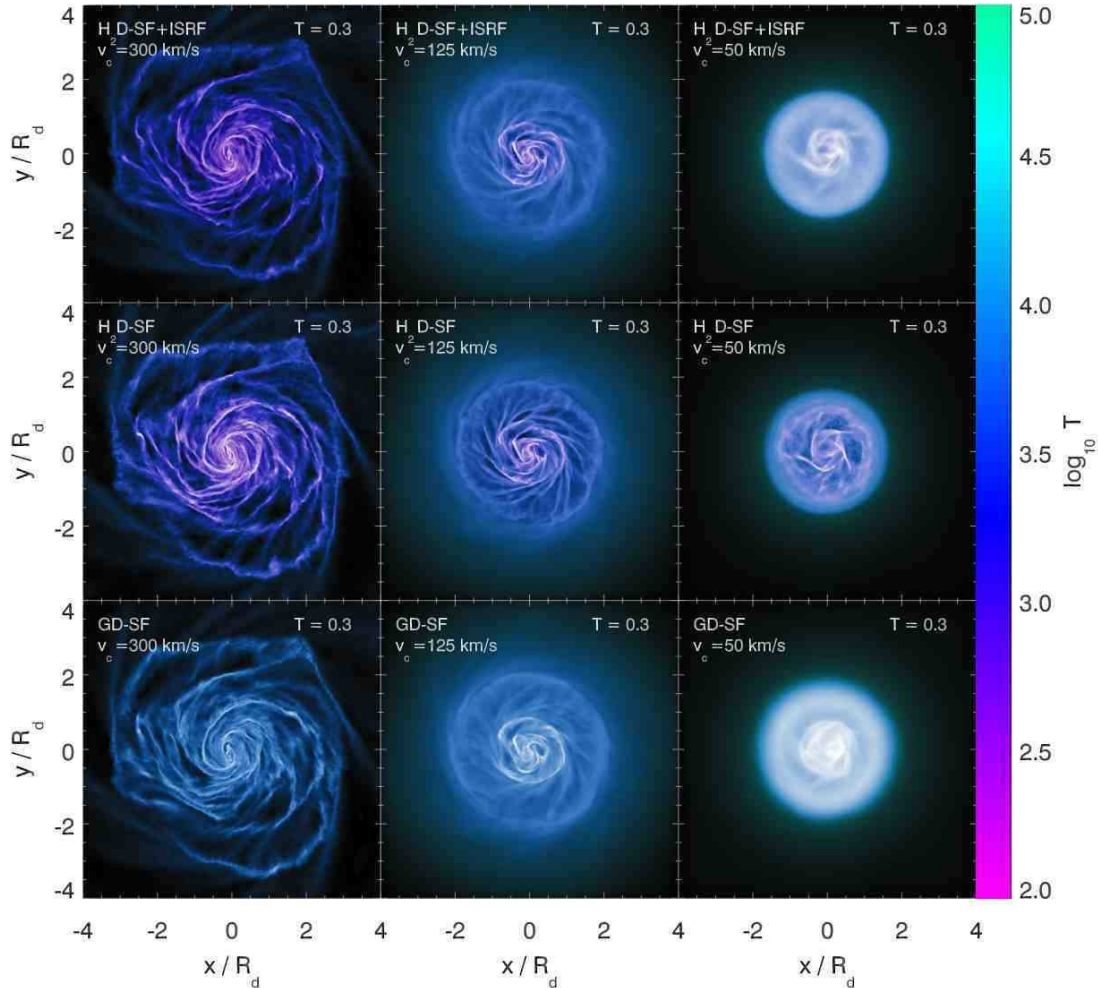


FIG. 4.— Gas distribution in galaxies with circular velocities of $v_{\text{circ}} = 300 \text{ km s}^{-1}$ (left column), $v_{\text{circ}} = 125 \text{ km s}^{-1}$ (middle column), and $v_{\text{circ}} = 50 \text{ km s}^{-1}$ (right column) for differing models of the ISM and star formation. Shown are an atomic cooling model with a $T = 10^4 \text{ K}$ temperature floor and star formation based on the gas density above a threshold of $n_{\text{H}} = 0.1 \text{ cm}^{-3}$ (“GD-SF”, bottom row), an atomic+molecular cooling model with a $T = 10^2 \text{ K}$ temperature floor and star formation based on the molecular gas density (“H₂D-SF”, middle row), and an atomic+molecular cooling model with a $T = 10^2 \text{ K}$ temperature floor, star formation based on the molecular gas density, and H₂-destruction by an interstellar radiation field (“H₂D-SF+ISRF”, top row). The intensity of the images reflect the gas surface density and are color-coded by the local effective gas temperature. The diffuse morphologies of low-mass galaxies in the GD-SF and H₂D-SF+ISRF models owe to the abundance of warm atomic gas with temperatures comparable to the velocity scale of the local potential.

larger than for galaxies with $v_{\text{circ}} \sim 80 \text{ km s}^{-1}$. The disk morphologies of the GD-SF runs are qualitatively consistent with their results.

3.1.1. Molecular Fraction vs. Gas Density

The molecular content of the ISM in models that account for the abundance of H₂ and other molecular gas depends on the physical properties of interstellar gas through Equation 5. Since the temperature and density phase structure of the ISM is dictated by the local cooling time, which is nonlinearly dependent on the temperature, density, metallicity, and ISRF strength, the calculation of the equilibrium molecular fraction as a function of the gas properties is efficiently calculated using hydrodynamical simulations of galaxy evolution. Figure 5 shows the molecular gas fraction f_{H_2} as a function of gas density n_{H} after evolving in ISM models with H₂-destruction by an ISRF (the H₂D-SF+ISRF model, right panel), and without an ISRF (the H₂D-SF model) for $t = 0.3 \text{ Gyr}$. Shown is the molecular content of each particle in the $v_{\text{circ}} = 50\text{--}300 \text{ km s}^{-1}$ disk galaxy simulations for each ISM model. The galaxy-to-galaxy and point-to-point variations in the metallicity, tem-

perature, ISRF strength contribute to the spread in molecular fractions at a given density n_{H} . For dense gas whose molecular fraction is suppressed by the numerical pressurization required to resolve the Jeans scale, typically at densities $n_{\text{H}} > 1 \text{ cm}^{-3}$, the molecular fraction is determined by scaling the $f_{\text{H}_2} - n_{\text{H}}$ relation to higher densities ($n_{\text{H}} > 30 \text{ cm}^{-3}$) (see §2.4). Without H₂-destruction, the molecular hydrogen content of low-density gas calculated using Cloudy is surprisingly large, with $f_{\text{H}_2} = 0.1$ at $n_{\text{H}} = 0.1 \text{ cm}^{-3}$ and $f_{\text{H}_2} \sim 0.35$ at $n_{\text{H}} = 1 \text{ cm}^{-3}$. For the H₂D-SF model (left panel), the atomic-to-molecular transition represents a physical calculation of the star formation threshold density prescription often included in coarse models of star formation in simulations of galaxy formation and evolution.

For the H₂D-SF+ISRF model (right panel), the destruction of H₂ by the ISRF reduces the molecular fraction in the low-density ISM to $f_{\text{H}_2} < 0.05$. The abundance of H₂ in this model is therefore greatly reduced relative to the H₂D-SF model that does not include an ISRF. Star formation in the H₂D-SF model operates in the presence of molecular gas, and the reduction

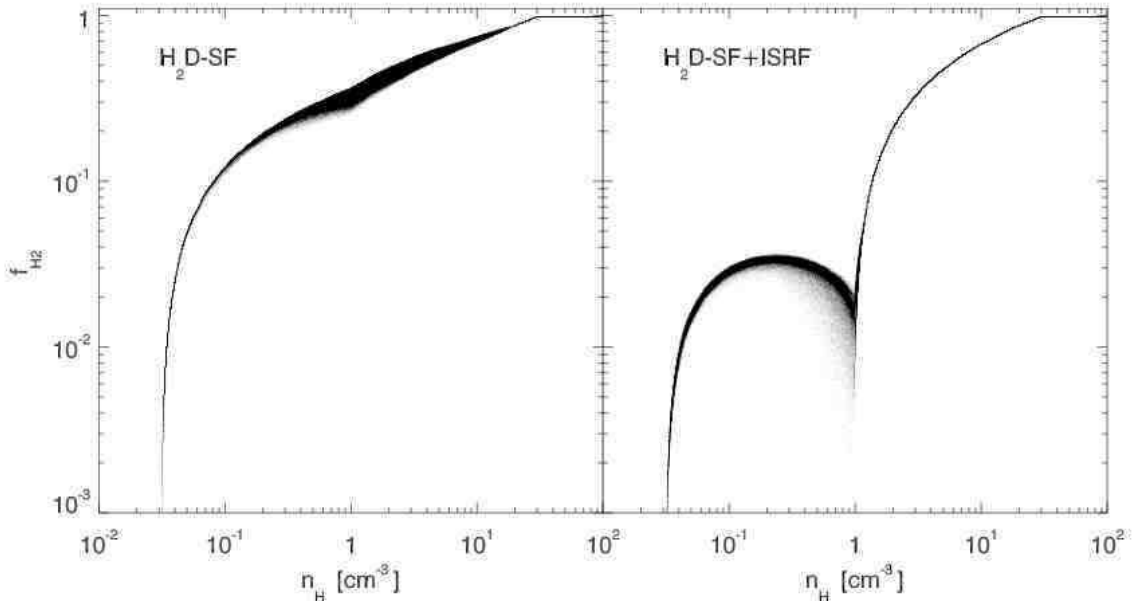


FIG. 5.— Molecular gas fraction f_{H_2} as a function of gas density n_{H} in ISM models with (right panel) and without (left panel) an interstellar radiation field (ISRF). The molecular fraction was calculated using the photoionization code Cloudy (Ferland et al. 1998). The ISRF is responsible for destroying molecular hydrogen at low ISM densities ($n_{\text{H}} \lesssim 1-10 \text{ cm}^{-3}$). For gas that is numerically-pressurized to resolve the Jeans scale, typically at densities $n_{\text{H}} > 1 \text{ cm}^{-3}$, the $f_{\text{H}_2} - n_{\text{H}}$ relation is scaled to higher densities ($n_{\text{H}} > 30 \text{ cm}^{-3}$) to account for the artificially suppressed molecular fraction (see §2.4).

of the molecular fraction to only a few percent of the ISM by mass will produce much lower star formation rates in low density gas ($n_{\text{H}} \lesssim 1 \text{ cm}^{-3}$) compared with either the $\text{H}_2\text{D-SF}$ model (which has a larger molecular fraction at low densities) or the GD-SF model (which allows for star formation in all gas above a density threshold, $n_{\text{H}} > 0.1 \text{ cm}^{-3}$). For denser gas in the $\text{H}_2\text{D-SF+ISRF}$ model (e.g. $n_{\text{H}} \gtrsim 1 \text{ cm}^{-3}$), the numerical pressurization of the ISM required to mitigate artificial Jeans fragmentation prevents much of the gas from reaching high densities where the molecular fraction becomes large ($f_{\text{H}_2} \sim 1$ at $n_{\text{H}} \gtrsim 100 \text{ cm}^{-3}$). As discussed in §2.4, in the absence of an artificial pressure floor the cooling function calculated by Cloudy would allow gas at densities $n_{\text{H}} > 1 \text{ cm}^{-3}$ to quickly condense to low temperatures ($T \sim 100 \text{ K}$) and higher densities ($n_{\text{H}} \gtrsim 100$), but the numerical pressurization prevents dense gas from reaching these equilibrium conditions. To account for this numerical limitation, at densities $n_{\text{H}} > 1 \text{ cm}^{-3}$ the $f_{\text{H}_2} - n_{\text{H}}$ relation of the $\text{H}_2\text{D-SF}$ and $\text{H}_2\text{D-SF+ISRF}$ models are scaled to higher densities ($n_{\text{H}} > 30 \text{ cm}^{-3}$, see §2.4). For simulations with much higher resolution in which the numerical pressurization becomes important at higher densities, this re-scaling of the molecular fraction would become unnecessary. For the $\text{H}_2\text{D-SF}$ model, the gas becomes highly molecular at densities $n_{\text{H}} \gtrsim 0.1 \text{ cm}^{-3}$ and the required numerical pressurization scheme has little effect on the molecular fraction of the ISM.

The density dependence of molecular fraction shown here may not be correct in detail (i.e., the transition to $f_{\text{H}_2} = 1$ may occur at an inaccurately low density). However, for our purposes the primary requirement is that the model captures the fraction of star forming gas as a function of density in a realistic fashion. The gas mass in disks in the $\text{H}_2\text{D-SF+ISRF}$ model at $\Sigma_{\text{gas}} \gtrsim 10 M_{\odot} \text{ pc}^{-2}$ is mostly molecular and the molecular fraction increases realistically with the external ISM pressure (see §3.3), in good agreement with observations (e.g., Wong & Blitz 2002; Blitz & Rosolowsky 2006).

3.1.2. Molecular Fraction vs. Disk Radius

The variations in the molecular fraction f_{H_2} as a function of the gas volume density n_{H} discussed in §3.1.1 map into f_{H_2} gradients with surface density or disk radius on the global scale of a galaxy model. Figure 6 shows azimuthally-averaged molecular fraction f_{H_2} as a function of the fractional disk scale length radius R/R_{d} in the simulated disk galaxies with $v_{\text{circ}} = 50 - 300 \text{ km s}^{-1}$ for molecular ISM models $\text{H}_2\text{D-SF+ISRF}$ and $\text{H}_2\text{D-SF}$, after $t = 0.3 \text{ Gyr}$ of evolution. The average molecular fraction decreases with decreasing rotational velocity, from $f_{\text{H}_2} > 0.6$ within a disk scale length for the $v_{\text{circ}} = 300 \text{ km s}^{-1}$ system (left panel) to $f_{\text{H}_2} < 0.4$ within a disk scale length for the $v_{\text{circ}} = 50 \text{ km s}^{-1}$ system (right column) in the $\text{H}_2\text{D-SF+ISRF}$ model. The radial dependence of the molecular fraction steepens in smaller mass galaxies relative to the $v_{\text{circ}} = 300 \text{ km s}^{-1}$ model since a larger fraction of gas has densities below the atomic-to-molecular transition. The impact of this trend on the global star formation relation is discussed below in §3.2.1.

The influence of H_2 -destruction by the ISRF on the molecular content of the ISM is clearly apparent in Figure 6. The presence of the ISRF in the $\text{H}_2\text{D-SF+ISRF}$ model steepens the dependence of molecular fraction f_{H_2} on the radius R for each galaxy compared with the $\text{H}_2\text{D-SF}$ model. The correlation of the molecular fraction with the structural properties of the disk, such as the mid-plane pressure, is examined in §3.3, but we note here that the variation of the molecular fraction with radius, surface density, or other structural variables provide constraints on the ISRF scaling with the star formation rate density provided in Equation 2. Given that the star formation rate in the molecular ISM models scales with the molecular gas density, the $\text{H}_2\text{D-SF+ISRF}$ model will have a lower star formation efficiency than the $\text{H}_2\text{D-SF}$ model. The implications of such lowered efficiency will be examined in §3.1.3, §3.2.1, and §3.2.2.

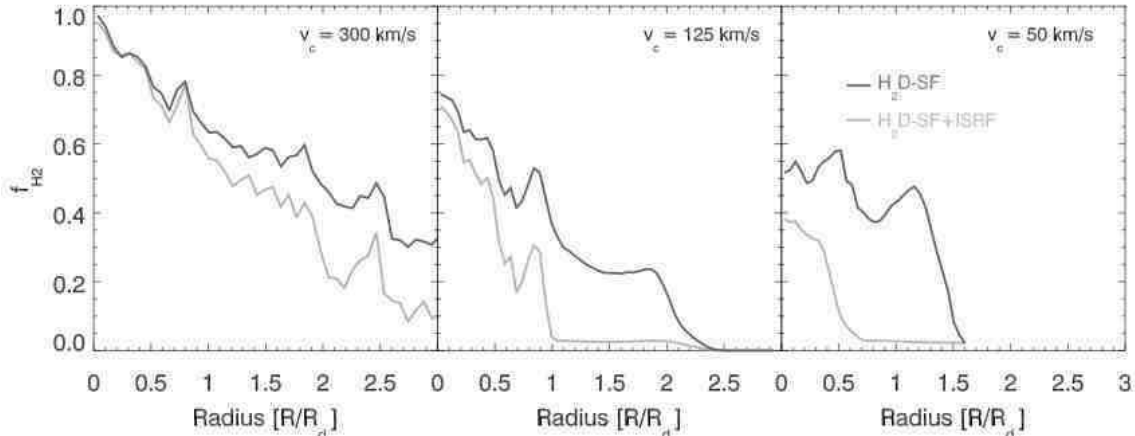


FIG. 6.— Molecular fraction as a function of radius in three simulated disk galaxies with ISM models with (light gray lines) and without (dark gray lines) an interstellar radiation field. The general trend is for molecular fraction to decrease and its dependence on radius to steepen with decreasing mass of the system. This trend is more pronounced in the model with the interstellar radiation field.

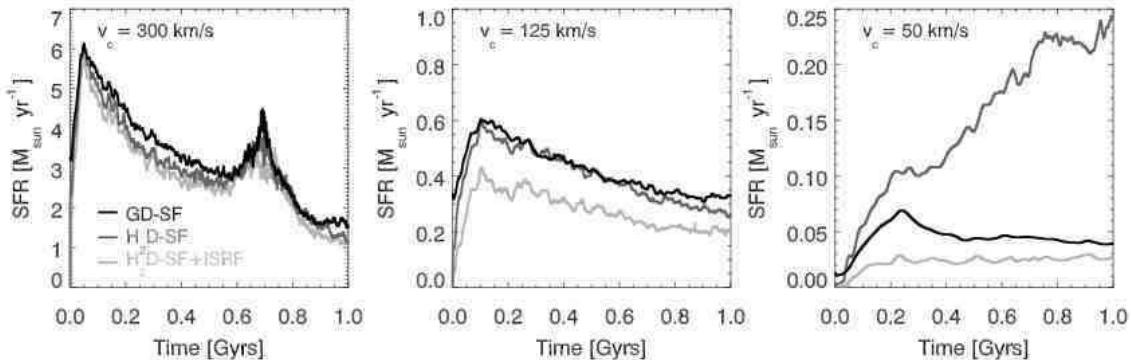


FIG. 7.— Star formation rates (SFRs) as a function of time in isolated disks. Shown are the SFRs for galaxy models with $v_{\text{circ}} = 50 \text{ km s}^{-1}$ (right panel), $v_{\text{circ}} = 125 \text{ km s}^{-1}$ (middle panel), and $v_{\text{circ}} = 300 \text{ km s}^{-1}$ (left panel) calculated from interstellar medium models that allow for cooling at temperatures $T > 10^4 \text{ K}$ (black lines) or cooling at temperatures $T > 10^2 \text{ K}$ with (light gray lines) and without (dark gray lines) destruction of H_2 by a local interstellar radiation field (ISRF). The star formation efficiency of the low-mass systems are strongly influenced by H_2 -destruction from the ISRF.

3.1.3. Star Formation Histories

The star formation histories of the simulated galaxies provide a summary of the efficiency of gas consumption for systems with different disk structures and models for ISM physics. Figure 7 shows the star formation rate (SFR) over the time interval $t = 0 - 1 \text{ Gyr}$ for the isolated galaxy models evolved with the GD-SF, $\text{H}_2\text{D-SF}$, and $\text{H}_2\text{D-SF+ISRF}$ models for the ISM and star formation. In most simulations, the SFR experiences a general decline as the gas is slowly converted into stars. Substantial increases in the SFR with time are driven either by the formation of bar-like structures (e.g., after $t \approx 0.7 \text{ Gyr}$ for the $v_{\text{circ}} = 300 \text{ km s}^{-1}$ galaxy, left panel) or, in one case, fragmentation of the cold ISM (after $t \approx 0.4 \text{ Gyr}$ for the $v_{\text{circ}} = 50 \text{ km s}^{-1}$ galaxy evolved with the $\text{H}_2\text{D-SF}$ model without H_2 -destruction).

For the most massive galaxy, differences in the relative star formation efficiencies of models that tie the SFR to the total gas density (the GD-SF model) or to the molecular gas density (the $\text{H}_2\text{D-SF}$ and $\text{H}_2\text{D-SF+ISRF}$ models) are not large. The ISM in the massive galaxy is dense, and when H_2 abundance is modeled much of the gas becomes molecular (see Figure 6). When H_2 -destruction is included the molecular content of the ISM in this galaxy is reduced at large radii and small surface densities, but much of the mass of the ISM (e.g., interior to a disk scale length) retains a molecular fraction comparable

to the ISM model without H_2 -destruction. The effect of the ISRF on the SFR of this galaxy is fairly small.

The SFR history of the intermediate-mass ($v_{\text{circ}} = 125 \text{ km s}^{-1}$) galaxy model is more strongly influenced by the H_2 -destroying ISRF. While the GD-SF and $\text{H}_2\text{D-SF}$ ISM models produce similar star formation efficiencies, reflecting the substantial molecular fraction in the ISM for the $\text{H}_2\text{D-SF}$ model, the effects of H_2 -destruction in the $\text{H}_2\text{D-SF+ISRF}$ model reduce the SFR by $\sim 30 - 40\%$. The time derivative of the SFR in the $\text{H}_2\text{D-SF+ISRF}$ model is also shallower than for the GD-SF or $\text{H}_2\text{D-SF}$ models, reflecting a reservoir of non-star-forming gas. In each model, the SFR of the whole system is similar to that estimated for M33 ($\text{SFR} \sim 0.25 - 0.7 M_{\odot} \text{ yr}^{-1}$, Kennicutt 1998; Hippelein et al. 2003; Blitz & Rosolowsky 2006; Gardan et al. 2007).

The effects of H_2 -destruction play a crucial role in determining the star formation history of the $v_{\text{circ}} = 50 \text{ km s}^{-1}$ system. The single phase ISM (GD-SF) model of the dwarf produces a SFR history qualitatively similar to the more massive galaxies, but in the $\text{H}_2\text{D-SF}$ model the star formation history changes dramatically. The colder ISM temperature allows the gaseous disk to become substantially thinner in this case compared to the GD-SF model, leading to higher densities and star formation rates. After $t \approx 0.4 \text{ Gyr}$ of evolution, the cold, dense gas in the $\text{H}_2\text{D-SF}$ model allows the ISM in the dwarf to

undergo large-scale instabilities and, quickly thereafter, fragmentation. The dense knots of gas rapidly increase their star formation efficiency compared with the more diffuse ISM of the GD-SF model and the SFR increases to a rate comparable to that calculated for the $v_{\text{circ}} = 125 \text{ km s}^{-1}$ model. In the $\text{H}_2\text{D-SF+ISRF}$ model, the equilibrium temperature of most diffuse (and metal poor) gas in the dwarf is increased and the vertical structure of the disk becomes thicker than in the $\text{H}_2\text{D-SF}$ model. The molecular content of the disk is thus substantially reduced (see the right panel of Figure 6) and the disk remains diffuse. As a result, the SFR drops to a low and roughly constant level. The constancy of the SFR in the $\text{H}_2\text{D-SF+ISRF}$ model is a result of the large gas reservoir that remains atomic and is therefore unavailable for star formation. As the molecular gas, which comprises a small fraction of the total ISM in the dwarf ($f_{\text{H}_2} \lesssim 0.1$ by mass), is gradually consumed it is continually refueled by the neutral gas reservoir.

The star formation history of the dwarf galaxy system in the $\text{H}_2\text{D-SF+ISRF}$ model demonstrates that physics other than energetic supernova feedback can regulate star formation and produce long gas consumption time scales in dwarf galaxies. Star formation rates in real galaxies similar to the $v_{\text{circ}} = 50 \text{ km s}^{-1}$ model fall in the wide range $\text{SFR} \sim 10^{-4} - 0.1 M_{\odot} \text{ yr}^{-1}$ (e.g., Hunter & Elmegreen 2004). While the $\text{H}_2\text{D-SF+ISRF}$ simulation of the dwarf galaxy produces a steady $\text{SFR} \sim 0.025 M_{\odot} \text{ yr}^{-1}$, we note that the galaxy DD0 154 that served as a model for the $v_{\text{circ}} = 50 \text{ km s}^{-1}$ system has a star formation rate of only $\text{SFR} \sim 0.004 M_{\odot} \text{ yr}^{-1}$ (Hunter & Elmegreen 2004).

3.2. Star Formation Relations in Galactic Disks

An important observational determination of the disk-averaged Schmidt-Kennicutt relation in galaxies was presented by Kennicutt (1998), who used $\text{H}\alpha$, HI, and CO data from nearly one hundred normal and starbursting galaxies to measure the Schmidt-Kennicutt relation over roughly four orders of magnitude in total gas surface mass density. Kennicutt (1998) found that

$$\Sigma_{\text{SFR}} = (2.5 \pm 0.7) \times 10^{-4} \times \left(\frac{\Sigma_{\text{gas}}}{1 M_{\odot} \text{ pc}^{-2}} \right)^{1.4 \pm 0.15} M_{\odot} \text{ yr}^{-1} \text{ kpc}^{-2} \quad (11)$$

best described the composite sample that included both normal and starburst galaxies. When bivariate fits were performed to each sample individually, the best-fit power-law indices were found to be $n_{\text{tot}} = 2.47 \pm 0.39$ for the normal galaxy sample and $n_{\text{tot}} = 1.40 \pm 0.13$ for the starburst sample. The molecule-rich starburst sample was found to have considerably less scatter at a fixed density than the normal galaxy sample, and the high-density end of the normal galaxy sample was found to track the disk-averaged Schmidt-Kennicutt relation of the composite galaxy population ($n_{\text{tot}} \approx 1.4$).

As mentioned in §1, spatially-dependent determinations of the Schmidt-Kennicutt relation have instead found a relation for the star formation rate surface density as a function of the total gas surface density that depends on the typical molecular content of the gas, in contrast to the global disk-averaged relations measured for entire galaxy sample of Kennicutt (1998). Molecule-rich systems or regions of galaxies have a relatively weak power-law dependence on the total gas density, similar to the original results for the entire Kennicutt (1998) sample. Such systems include the galaxies observed by Wong & Blitz (2002) ($n_{\text{tot}} = 1.7 \pm 0.3$, corrected

for extinction) or the molecular gas-dominated regions of the galaxy M51a ($n_{\text{tot}} = 1.56 \pm 0.04$, Kennicutt et al. 2007). The Boissier et al. (2003) sample of galaxies with a wide range of circular velocities displays a total gas Schmidt-Kennicutt relation index in the range $n_{\text{tot}} = 1.96 - 3.55$, depending on the fitting method. The detailed examination of star formation and gas density in the comparably small and molecule-poor galaxy M33 ($v_{\text{circ}} \approx 120 \text{ km s}^{-1}$, $f_{\text{H}_2} \approx 0.1$) by Heyer et al. (2004) reveals a total gas Schmidt-Kennicutt relation index of $n_{\text{tot}} = 3.3 \pm 0.1$.

The total gas Schmidt-Kennicutt relation steepens at low gas surface densities where the molecular fraction becomes small ($f_{\text{H}_2} \ll 1$). ISM regions with low molecular fractions are typical of dwarf galaxies, low surface brightness galaxies, and the outskirts of normal galaxies. The steepening of the total gas Schmidt-Kennicutt relation in these regions may be understood if the star formation rate tracks the molecular gas surface density rather than the total gas surface density. Indeed, the observed molecular gas Schmidt-Kennicutt relation has a power-law index that remains approximately constant for the original disk-averaged Kennicutt (1998) starburst sample ($n_{\text{mol}} \approx 1.4$), the Wong & Blitz (2002) molecule-rich sample ($n_{\text{mol}} \approx 1.4$), the molecule-rich regions of M51a ($n_{\text{mol}} = 1.37 \pm 0.03$, Kennicutt et al. 2007), the diverse galaxies of the Boissier et al. (2006) sample ($n_{\text{mol}} \approx 1.3$), and the molecule-poor galaxy M33 ($n_{\text{mol}} = 1.36 \pm 0.08$, Heyer et al. 2004).

3.2.1. The Total Gas Schmidt-Kennicutt Relation

A dichotomy between the total gas and molecular gas Schmidt-Kennicutt relations is currently suggested by the data and should be a feature of models of the ISM and star formation. Figure 8 shows the simulated total gas Schmidt-Kennicutt relation that compares the star formation rate surface density Σ_{SFR} to the total gas surface density Σ_{gas} for different galaxy models. The quantities Σ_{SFR} and Σ_{gas} are azimuthally-averaged in annuli of width $\Delta r = 150 h^{-1} \text{ pc}$ for the $v_{\text{circ}} = 300 \text{ km s}^{-1}$ and $v_{\text{circ}} = 125 \text{ km s}^{-1}$ systems and $\Delta r = 75 h^{-1} \text{ pc}$ for the smaller $v_{\text{circ}} = 50 \text{ km s}^{-1}$ disk. Regions within the radius enclosing 95% of the gas disk mass are shown. The Schmidt-Kennicutt relation is measured in each disk at times $t = 0.3 \text{ Gyr}$ and $t = 1.0 \text{ Gyr}$ to monitor its long-term evolution. Power-law fits to the SFR density as a function of the total gas surface mass densities in the range $\Sigma_{\text{gas}} = 5 - 100 M_{\odot} \text{ pc}^{-2}$ measured at $t = 0.3 \text{ Gyr}$ are indicated in each panel, with the range chosen to approximate regimes that are currently observationally accessible. The simulated relations between Σ_{SFR} and Σ_{gas} are not strict power-laws, and different choices for the range of surface densities or simulation time of the fit may slightly change the inferred power-law index, with lower surface densities typically leading to larger indices and, similarly, later simulation times probing lower surface densities and correspondingly steeper indices. Exceptions are noted where appropriate, but the conclusions of this paper are not strongly sensitive to the fitting method of the presented power-law fits. Disk-averaged SFR and surface mass densities are also measured and plotted for comparison with the non-starburst galaxies of Kennicutt (1998).

Each row of panels in Figure 8 shows results for the three galaxy models evolved with different models for the ISM and star formation. For the traditional GD-SF model, the $\Sigma_{\text{SFR}} - \Sigma_{\text{gas}}$ correlation in massive, thin-disk systems with large circular velocities tracks the input relation for this model, $\dot{\rho}_{\star} \propto \rho_g^{1.5}$, at intermediate surface densities. At low surface densi-

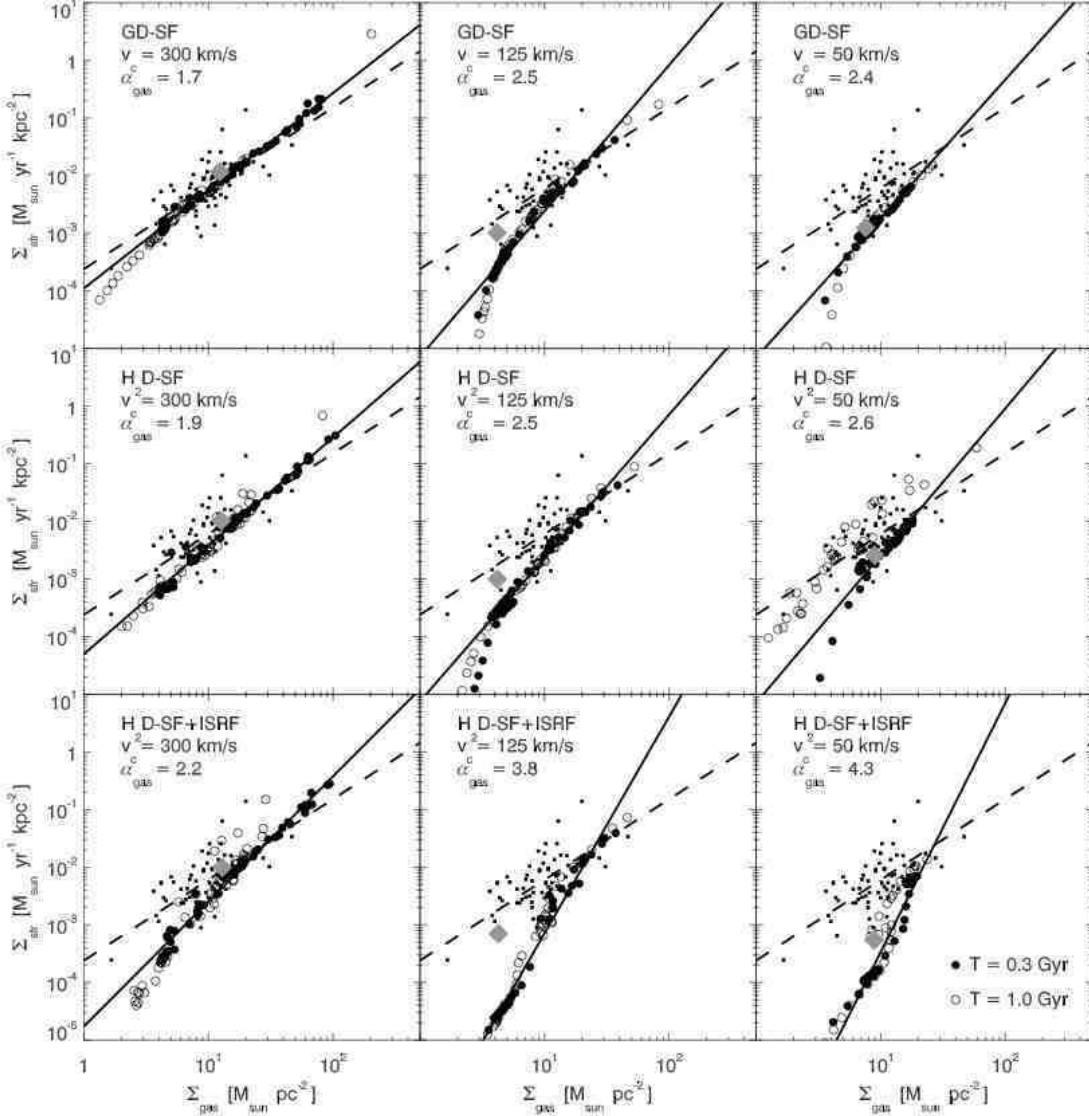


FIG. 8.— Schmidt-Kennicutt relation for total gas surface densities. Shown is the star formation rate surface density Σ_{SFR} as a function of the total gas surface density Σ_{gas} for galaxy models with circular velocities of $v_{\text{circ}} = 50 \text{ km s}^{-1}$ (right column), $v_{\text{circ}} = 125 \text{ km s}^{-1}$ (middle column), and $v_{\text{circ}} = 300 \text{ km s}^{-1}$ (left column) for ISM models that include atomic coolants (upper row), atomic+molecular coolants with (lower row) and without (middle row) H_2 -destruction from a local interstellar radiation field. The surface densities Σ_{SFR} and Σ_{gas} are measured in annuli from the simulated disks after evolving for $t = 0.3 \text{ Gyr}$ (solid circles) and $t = 1 \text{ Gyr}$ (open circles) in isolation. The disk-averaged data from Kennicutt (1998) is shown for comparison (small dots). The best power-law fits to the individual galaxies have indices in the range $\alpha \approx 1.7 - 4.3$ (solid lines). Deviations from the $\Sigma_{\text{SFR}} \propto \Sigma_{\text{gas}}^{1.5}$ relation are caused by the radial variation in the molecular gas fraction f_{H_2} , the scale height of star-forming gas h_{SFR} , and the scale height of the total gas distribution h_{gas} . The total disk averaged surface densities (grey diamonds) are consistent with the Kennicutt (1998) normalization for normal, massive star-forming galaxies (dashed lines).

ties, massive disks deviate from the $\Sigma_{\text{SFR}} \propto \Sigma_{\text{gas}}^{1.5}$ relation as the imposed density threshold is increasingly probed in the disk interior and disk flaring begins to steepen the relation between the three-dimensional density ρ_g and the gas surface density Σ_{gas} . At large surface densities, secular processes, such as angular momentum transport via bars, can steepen the $\Sigma_{\text{SFR}} - \Sigma_{\text{gas}}$ relation averaged on $\sim 100 \text{ pc}$ scales by creating dense central gas concentrations. In lower mass galaxies, the disks are thicker at a given gas surface density, as dictated by hydrostatic equilibrium (e.g., Kaufmann et al. 2007), with a correspondingly lower average three-dimensional density. The Schmidt-Kennicutt relation therefore steepens somewhat between galaxies with $v_{\text{circ}} = 300 \text{ km s}^{-1}$ and $v_{\text{circ}} = 125 \text{ km s}^{-1}$ in this star formation model, but does not fully capture the mass-dependence of the Schmidt-Kennicutt relation apparent

in the observations.

The middle row of Figure 8 shows the total gas Schmidt-Kennicutt relation measured in disks evolved with the $\text{H}_2\text{D-SF}$ model. Recall that star formation in this model is explicitly tied to the local H_2 fraction (see Equation 4) without an imposed star formation density threshold. The Schmidt-Kennicutt relation results of this model are generally similar to the more prescriptive GD-SF model. The power-law index increases from $n_{\text{tot}} \approx 1.9$ for large- v_{circ} galaxies to $n_{\text{tot}} \approx 2.6$ for the smallest galaxy examined, but are similar to the GD-SF model results at intermediate to large surface densities. The arbitrary density threshold for star formation included in the GD-SF model roughly mimics the physics of the atomic-to-molecular gas transition calculated by Cloudy for the $\text{H}_2\text{D-SF}$ model, as molecular transition begins at densities of $n_{\text{H}} \sim$

0.1cm^{-3} when the effects of H_2 -destruction by an ISRF are *not* included (see Figure 5). The $\text{H}_2\text{D-SF}$ model has the additional feature that molecular ISM gas can reach considerably lower temperatures than in the atomic cooling-only GD-SF model, and, over time, the ISM gas in the $v_{\text{circ}} = 50\text{km s}^{-1}$ galaxy can become cold enough to reach high-densities and molecular fractions. In this case, the relevant temperature scale for hydrostatic equilibrium decreases to $T < 10^4\text{K}$ allowing the very large gas reservoir in the low-mass dwarf to cool into a thin disk. While the density threshold for star formation included in the GD-SF model roughly captures the atomic-to-molecular gas transition, it simply fails (and was not designed) to replicate changes in the thermal properties of the ISM that can be accompanied by the presence of low-temperature coolants. The increase in the molecular content of the disk contributes to the increase in the star formation efficiency in the dwarf galaxy during its evolution seen in the middle right panel of Figure 8. However, observed $v_{\text{circ}} \approx 50\text{km s}^{-1}$ galaxies have *very low* molecular fractions and the high molecular content of the dwarf at $t = 1\text{Gyr}$ is a potential deficit of the $\text{H}_2\text{D-SF}$ model.

The bottom row of Figure 8 shows the Schmidt-Kennicutt relation for the most complete ISM model examined (the " $\text{H}_2\text{D-SF+ISRF}$ " model), which includes the features of the $\text{H}_2\text{D-SF}$ model and the additional effect of a local interstellar radiation field whose strength scales with the local star formation rate density. In this model, the Schmidt-Kennicutt relation power-law index increases steadily from $n_{\text{tot}} = 2.2$ for the $v_{\text{circ}} = 300\text{km s}^{-1}$ galaxy to $n_{\text{tot}} = 4.3$ for the $v_{\text{circ}} = 50\text{km s}^{-1}$ dwarf. The decreased abundance of H_2 at low densities has steepened the Schmidt-Kennicutt relation at low gas surface densities compared with either the GD-SF or $\text{H}_2\text{D-SF}$ models. The ISM in the dwarf galaxy is prevented from becoming fully molecular and maintains an extremely steep Schmidt-Kennicutt relation over its evolution from $t = 0.3\text{Gyr}$ to $t = 1\text{Gyr}$. Consequently, the global star formation rate of the model dwarf galaxy in this case stays low and approximately constant. The global gas consumption time scale is also much longer than in the other two models.

Note that while the disk-averaged Schmidt-Kennicutt relation determination for the galaxies have a lower star formation efficiency in the $\text{H}_2\text{D-SF+ISRF}$ model than in the other models of the ISM, the values are still consistent with the observational determinations by Kennicutt (1998), Wong & Blitz (2002), Boissier et al. (2003), and Boissier et al. (2006).

3.2.2. The Molecular Gas Schmidt-Kennicutt Relation

For the ISM models that explicitly track the molecular content of interstellar gas, the molecular gas Schmidt-Kennicutt relation correlating the SFR surface density Σ_{SFR} and the molecular gas surface density Σ_{H_2} provides an important observational constraint unavailable to coarse treatments of the ISM that do not model molecular gas. As discussed in §3.2, the two-sigma range in observational estimates of the molecular gas Schmidt-Kennicutt relation power-law index is $n_{\text{mol}} \approx 1.2 - 1.7$. This variation is considerably smaller than the variation in the slope of the $\Sigma_{\text{SFR}} - \Sigma_{\text{gas}}$ relation. Figure 9 shows the molecular gas Schmidt-Kennicutt relation measured in galaxies evolved with the two molecular ISM models considered in this paper. The SFR and molecular gas surface densities are measured from the simulations as described in §3.2.1 and the reported power-law indices were fit to molecular gas surface densities in the range $\Sigma_{\text{H}_2} = 0.1 - 100M_{\odot}\text{pc}^{-2}$.

The results of the $\text{H}_2\text{D-SF}$ model are shown in the upper

panel of Figure 9. The disk-averaged SFR and molecular gas surface densities are consistent with the observational determination of the molecular gas Schmidt-Kennicutt relation by Kennicutt (1998). The molecular gas Schmidt-Kennicutt relation power-law index of this model is similar for galaxies of different mass $n_{\text{mol}} = 1.4 - 1.5$. Unlike the $\Sigma_{\text{SFR}} - \Sigma_{\text{gas}}$ relation, the molecular gas Schmidt-Kennicutt relation is well-described by a power-law over a wide range in surface densities in the $\text{H}_2\text{D-SF}$ model. As we discussed in the previous section, the low-mass dwarf galaxy experiences an increase in the star formation efficiency at a fixed surface density during the evolutionary period between $t = 0.3\text{Gyr}$ and $t = 1.0\text{Gyr}$ owing to a nearly complete conversion of its ISM to molecular gas in the $\text{H}_2\text{D-SF}$ model.

Panels in the bottom row of Figure 9 show that the effect of H_2 -destruction by a local interstellar radiation field in the $\text{H}_2\text{D-SF+ISRF}$ model is to control the amplitude of the $\Sigma_{\text{SFR}} - \Sigma_{\text{H}_2}$ relation. The power-law slope of the relation remains the same, $n_{\text{mol}} \approx 1.2 - 1.3$, for systems of all masses. The normalization and power-law index of the molecular gas Schmidt-Kennicutt relation in this model is quite stable with time, reflecting how the equilibrium temperature and molecular fractions of the ISM in the $\text{H}_2\text{D-SF+ISRF}$ are maintained between simulation times $t = 0.3\text{Gyr}$ and $t = 1.0\text{Gyr}$. Only the most massive galaxy experiences noticeable steepening of the $\Sigma_{\text{SFR}} - \Sigma_{\text{H}_2}$ correlation at high surface densities. The disk-averaged observations of the molecular gas Schmidt-Kennicutt relation by Kennicutt (1998) are well-matched by the simulations and remain approximately constant over their duration.

3.2.3. Structural Schmidt-Kennicutt Relation

While the observational total and molecular gas Schmidt-Kennicutt relations are well-reproduced by the simulated galaxy models, local deviations from a power-law $\Sigma_{\text{SFR}} - \Sigma_{\text{gas}}$ or $\Sigma_{\text{SFR}} - \Sigma_{\text{H}_2}$ correlation are abundant. Although these deviations are physical, exhibited by real galaxies, and are well-understood within the context of the simulations, a question remains as to whether a relation that trivially connects the SFR density Σ_{SFR} and the properties of the disks exists.

Dynamical Schmidt-Kennicutt-like relations that incorporate information about global dynamical processes in the disk, such as $\Sigma_{\text{SFR}} \propto \Sigma\Omega$, have been examined thoroughly in the literature, but, as we show in §3.4 and the Appendix, these relations are likely secondary correlations between more fundamental properties of the disk galaxy models. The primary relation between the star formation rate and the gas properties in the simulations are encapsulated by Equation 4, which relates the three-dimensional star formation rate density, $\dot{\rho}_{\star}$, to the ratio of the molecular gas density and the dynamical time scaling with density, $f_{\text{H}_2}\rho_g^{1.5}$. For the $\text{H}_2\text{D-SF}$ and $\text{H}_2\text{D-SF+ISRF}$ models where the molecular gas density is tracked, f_{H_2} is calculated via Equation 5. In the single phase ISM (GD-SF) model, the molecular fraction is set to $f_{\text{H}_2} = 1$ at gas densities above the star formation threshold density $n_{\text{H}} = 0.1\text{cm}^{-3}$. We can relate the three-dimensional properties in the ISM to the observed two-dimensional surface densities through the characteristic scale heights of the disks. The SFR surface density is simply related to an average local star formation rate volume density $\langle\dot{\rho}_{\star}\rangle$ through the scale height of star-forming gas h_{SFR} as

$$\Sigma_{\text{SFR}} \propto \langle\dot{\rho}_{\star}\rangle h_{\text{SFR}} \quad (12)$$

Here, the averaging of the three-dimensional density is under-

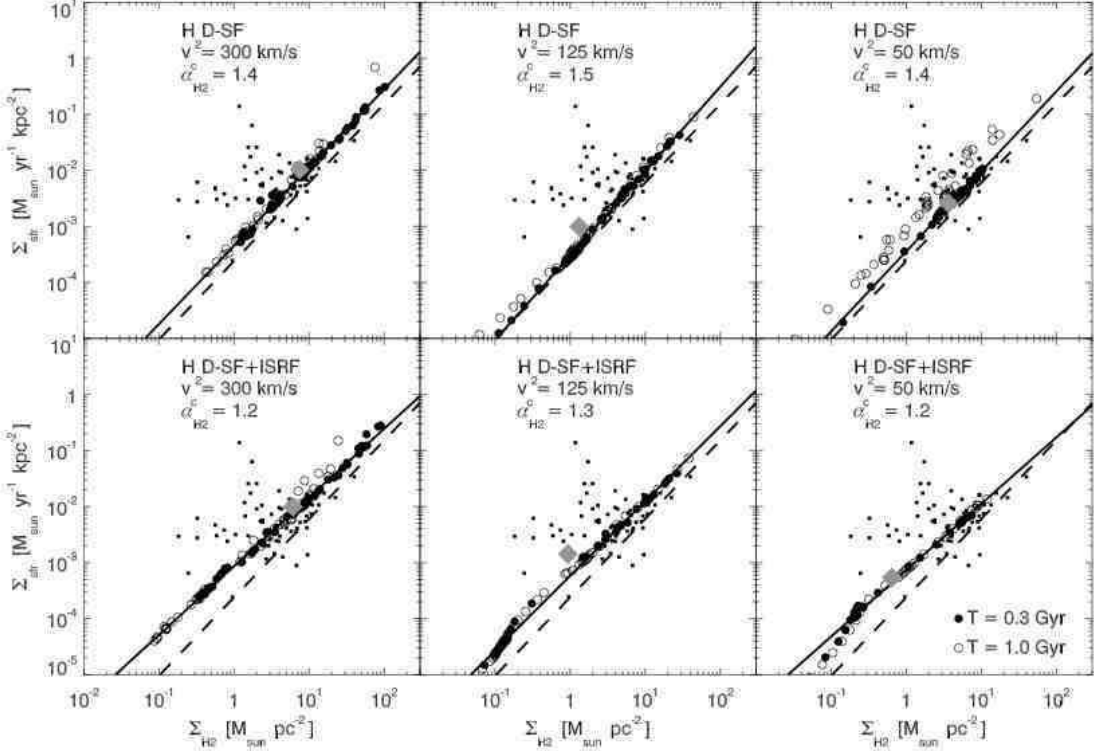


FIG. 9.— Schmidt-Kennicutt relation for molecular gas surface densities. Shown is the star formation rate surface density Σ_{SFR} as a function of the molecular gas surface density Σ_{H_2} for galaxy models with circular velocities of $v_{\text{circ}} = 50 \text{ km s}^{-1}$ (right panels), $v_{\text{circ}} = 125 \text{ km s}^{-1}$ (middle panels), and $v_{\text{circ}} = 300 \text{ km s}^{-1}$ (left panels) and ISM models that include atomic+molecular coolants with (lower panels) and without (upper panels) H_2 -destruction from a local interstellar radiation field. The surface densities Σ_{SFR} and Σ_{H_2} are measured in annuli (dark circles) from the simulated disks after evolving for $t = 0.3 \text{ Gyr}$ (solid circles) and $t = 1 \text{ Gyr}$ (open circles) in isolation. The disk-averaged data from Kennicutt (1998) is shown for comparison (small dots). The best power-law fits to the individual galaxies have indices in the range $\alpha \approx 1.2 - 1.5$ (solid lines). The total disk averaged surface densities (grey diamonds) are consistent with the Kennicutt (1998) relation for normal, massive star-forming galaxies (dashed lines).

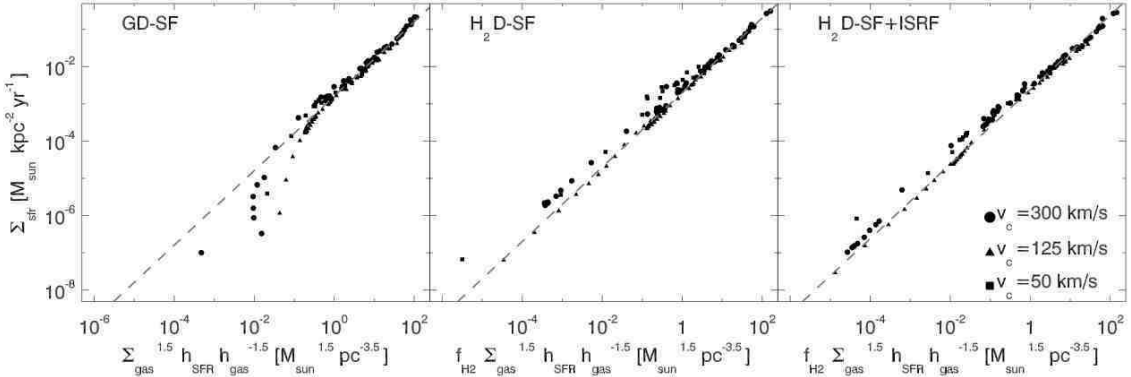


FIG. 10.— A predicted star formation correlation for disk galaxies. The star formation rate density in the simulations is calculated as $\dot{\rho}_* = f_{\text{H}_2} \rho_g / t_* \propto f_{\text{H}_2} (\rho_g) \rho_g^{1.5}$, where f_{H_2} is the molecular fraction, ρ_g is the gas density, and t_* is a star formation time-scale that varies with the local gas dynamical time. The local star formation rate surface density should scale as $\Sigma_{\text{SFR}} \propto \dot{\rho}_* h_{\text{SFR}}$, where h_{SFR} is the scale height of star-forming gas. Similarly, $\Sigma_{\text{gas}} \propto \rho_g h_{\text{gas}}$, where h_{gas} is the total gas scale height. The simulations predict that the star formation rate density in disks should correlate with the gas surface density as $\Sigma_{\text{SFR}} \propto f_{\text{H}_2} h_{\text{SFR}} h_{\text{gas}}^{-1.5} \Sigma_{\text{gas}}^{1.5}$ (dashed lines).

stood to operate over the region of the disk where the two-dimensional surface density is measured. Similarly, the gas surface and volume densities are related by the proportionality

$$\Sigma_{\text{gas}} \propto \langle \rho_g \rangle h_g. \quad (13)$$

If Equation 4 that determines the star formation density is averaged over the scale on which Σ_{SFR} is measured as

$$\langle \dot{\rho}_* \rangle \propto \langle f_{\text{H}_2} \rangle \langle \rho_g \rangle^{1.5}, \quad (14)$$

then the proportionalities can be combined to give

$$\Sigma_{\text{SFR}} \propto \langle f_{\text{H}_2} \rangle \frac{h_{\text{SFR}}}{h_g^{1.5}} \Sigma_{\text{gas}}^{1.5}. \quad (15)$$

Equation 15 can be interpreted as a Schmidt-Kennicutt-like correlation that incorporates information about the molecular gas abundance and the structural properties of disks through their characteristic scale heights.

Figure 10 shows the predicted structural Schmidt-Kennicutt relation for the simulated disk galaxies. The star formation,

and surface densities are azimuthally-averaged in annuli, as described in §3.2.1 and §3.2.2, and limited to regions of the disk where star formation is active. The characteristic gas scale height h_{gas} is determined as a mass-weighted average of the absolute value of vertical displacement for the annular gas distributions. The characteristic star-forming gas scale height h_{SFR} is determined in a similar manner, but for gas that satisfies the condition for star formation (e.g. $f_{\text{H}_2} > 0$ for the H₂D-SF and H₂D-SF+ISRF models or $n_{\text{H}} > 0.1$ for the GD-SF model). Measurements from the simulations are presented after evolving the systems for $t = 0.3\text{Gyr}$ with the GD-SF (left panel), H₂D-SF (middle panel), and H₂D-SF+ISRF (right panel) ISM models. In each case, the star formation rate density Σ_{SFR} in disks linearly correlates with quantity $f_{\text{H}_2} h_{\text{SFR}} h_{\text{gas}}^{-1.5} \Sigma_{\text{gas}}^{1.5}$.

This relation shows explicitly that the behavior of the $\Sigma_{\text{SFR}} - \Sigma_{\text{gas}}$ relation can be understood in terms of the dependence of f_{H_2} and h_{gas} on Σ_{gas} . For example, the Schmidt-Kennicutt relation can have a fixed power law $\Sigma_{\text{SFR}} \propto \Sigma_{\text{gas}}^{1.5}$ when f_{H_2} and h_{gas} are roughly independent of Σ_{gas} (e.g., M51a, Kennicutt et al. 2007), but then steepen when the molecular fraction becomes a strong function of gas surface density in a manner characteristic of dwarf galaxies, large low surface brightness galaxies, or the outskirts of normal galaxies. Deviations from the $\Sigma_{\text{gas}}^{1.5}$ relation can also occur when h_{gas} changes quickly with decreasing Σ_{gas} in the flaring outer regions of the disks. Such flaring is observed for the Milky Way at $R \gtrsim 10$ kpc (e.g., Wolfire et al. 2003, and references therein).

3.3. Local Pressure, Stellar Radiation, and H₂-Fraction

Elmegreen (1993b) calculated the dependence of the ISM molecular fraction f_{H_2} on the local pressure and radiation field strength, including the effects of H₂ self-shielding and dust extinction. The calculations of Elmegreen (1993b) suggested that

$$f_{\text{H}_2} \propto P_{\text{ext}}^{2.2} j^{-1}, \quad (16)$$

where P_{ext} is the external pressure and j is the volume emissivity of the radiation field. Wong & Blitz (2002) used observations to determine the correlation between molecular fraction f_{H_2} and the hydrostatic equilibrium mid-plane pressure in galaxies, given by

$$P_{\text{ext}} \approx \frac{\pi}{2} G \Sigma_{\text{gas}} \left(\Sigma_{\text{gas}} + \frac{\sigma}{c_*} \Sigma_* \right), \quad (17)$$

where c_* is the stellar velocity dispersion and σ is the gas velocity dispersion (see Elmegreen 1989). From observations of seven disk galaxies and the Milky Way, Wong & Blitz (2002) determined that the observed molecular fraction scaled with pressure as

$$\Sigma_{\text{H}_2} / \Sigma_{\text{HI}} \propto P_{\text{ext}}^{0.8}. \quad (18)$$

Subsequently, Blitz & Rosolowsky (2004) and Blitz & Rosolowsky (2006) studied these correlations in a larger sample of 28 galaxies. Blitz & Rosolowsky (2006) found that if the mid-plane pressure was defined as

$$\begin{aligned} \frac{P_{\text{ext}}}{k} &= 272 \text{ cm}^{-3} \text{ K} \left(\frac{\Sigma_{\text{g}}}{M_{\odot} \text{ pc}^{-2}} \right) \left(\frac{\Sigma_*}{M_{\odot} \text{ pc}^{-2}} \right)^{0.5} \\ &\times \left(\frac{\sigma}{\text{km s}^{-1}} \right) \left(\frac{h_*}{\text{pc}} \right)^{-0.5}, \end{aligned} \quad (19)$$

⁵ Small deviations in the GD-SF model at low surface densities owe to the sharp density threshold for star formation adopted in this model (see Schaye & Dalla Vecchia 2007, for a related discussion).

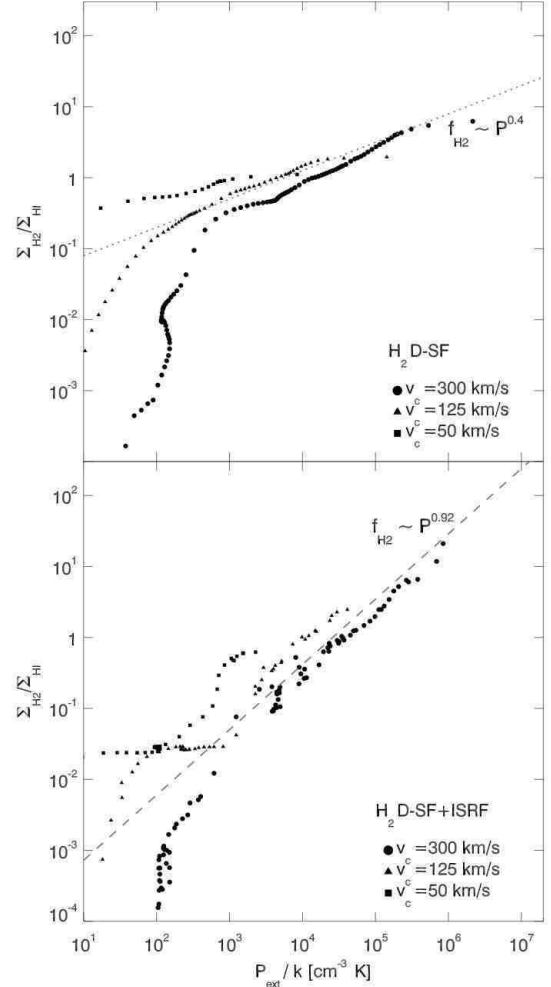


FIG. 11.— Molecular fractions as a function of external pressure in isolated disks. Shown are the molecular-to-atomic gas surface density ratios $\Sigma_{\text{H}_2}/\Sigma_{\text{HI}}$ measured in radial bins as a function of the local external pressure P_{ext} defined by Blitz & Rosolowsky (2004) for galaxies with $v_{\text{circ}} \approx 300 \text{ km s}^{-1}$ (circles), $v_{\text{circ}} \approx 125 \text{ km s}^{-1}$ (triangles), and $v_{\text{circ}} \approx 50 \text{ km s}^{-1}$ (squares) circular velocities. The simulations that include H₂-destruction by an ISRF (lower panel) follow the observed $\Sigma_{\text{H}_2}/\Sigma_{\text{HI}} \propto P_{\text{ext}}^{0.9}$ power-law scaling (dashed line), while the simulations that do not include an ISRF (upper panel) have a weaker scaling than that found observationally ($\Sigma_{\text{H}_2}/\Sigma_{\text{HI}} \sim P_{\text{ext}}^{0.4}$, dotted line).

where h_* is the stellar scale height, then the molecular fraction scaled with P_{ext} as

$$\Sigma_{\text{H}_2}/\Sigma_{\text{HI}} \propto P_{\text{ext}}^{0.92}. \quad (20)$$

Wong & Blitz (2002) state that if the ISRF volume emissivity $j \propto \Sigma_* \propto \Sigma_{\text{g}}$ and the stellar velocity dispersion was constant, then the Elmegreen (1993b) calculations would provide a relation $f_{\text{H}_2} \propto P_{\text{ext}}^{1.7}$ much steeper than observed. Blitz & Rosolowsky (2006) suggested that if the stellar velocity dispersion scales as $c_* \propto \Sigma_*^{0.5}$ and $j \propto \Sigma_*$, then the predicted scaling is closer to the observed scaling. These assumptions provide $f_{\text{H}_2} \propto P_{\text{ext}}^{1.2}$.

The relation between $\Sigma_{\text{H}_2}/\Sigma_{\text{HI}}$ and P_{ext} can be measured for the simulated disks. Figure 11 shows $\Sigma_{\text{H}_2}/\Sigma_{\text{HI}}$ as a function of P_{ext} , measured from the simulations according to Equation 19 in annuli, for simulated disks with (bottom panel) and without (top panel) H₂-destruction by an ISRF. The simulations with an ISRF scale in a similar way to the systems observed by Blitz & Rosolowsky (2006), while the simulated

disks without an ISRF have a weaker scaling. The simulated galaxies have $c_* \propto \Sigma_*^{0.5}$ and roughly constant gas velocity dispersions.

Given the scaling of the ISRF strength in the simulations, for which $U_{\text{isrf}} \propto \Sigma_{\text{SFR}} \propto \Sigma_{\text{gas}}^{n_{\text{tot}}}$ with $n_{\text{tot}} \sim 2-4$ according to the total gas Schmidt-Kennicutt relations measured in §3.2.1, and the scale-dependent star formation efficiency, which will instill the proportionality $\Sigma_* \propto \Sigma_{\text{gas}}^\beta$ with $\beta \neq 1$ in general, the scaling between the molecular fraction and pressure $f_{\text{H}_2} \propto P_{\text{ext}}^{0.9}$ is not guaranteed to be satisfied in galaxies with greatly varying Schmidt-Kennicutt relations. However, given the relation $f_{\text{H}_2} \propto P_{\text{ext}}^{2.2} j^{-1}$ calculated by Elmegreen (1993b), a general relation between the molecular fraction and interstellar pressure can be calculated in terms of the power-law indices n of the total gas Schmidt-Kennicutt relation and β that describes the relative distribution gas and stars in the disk.

Assuming a steady state, the volume emissivity in the simulated ISM then scales with the gas surface density as

$$j \propto U_{\text{isrf}} \propto \Sigma_{\text{gas}}^{n_{\text{tot}}}. \quad (21)$$

Given the ISRF strength in the simulations and a proportionality of the stellar surface density with the total gas surface density of the form $\Sigma_* \propto \Sigma_{\text{gas}}^\beta$, we find that, with the scaling between the molecular fraction, pressure, and ISRF volume emissivity calculated by Elmegreen (1993b), the $f_{\text{H}_2} - \Sigma_{\text{gas}}$ relation should follow

$$f_{\text{H}_2} \propto \Sigma_{\text{gas}}^{2.2(1+\beta/2)-n}. \quad (22)$$

If the molecular fraction scales with the mid-plane pressure as $f_{\text{H}_2} \propto P^\alpha$, then the index α can be expressed in terms of the power-law dependences of the Schmidt-Kennicutt relation and the $\Sigma_* - \Sigma_{\text{gas}}$ correspondence as

$$\alpha = \frac{2.2(1+\beta/2)-n}{1+\beta/2}. \quad (23)$$

The largest galaxy simulated, with a circular velocity of $v_{\text{circ}} \approx 300 \text{ km s}^{-1}$, has a total gas Schmidt-Kennicutt relation with a scaling $\Sigma_{\text{SFR}} \propto \Sigma_{\text{gas}}^2$ (see Figure 8) and a nearly linear scaling of the stellar and gas surface densities ($\beta \approx 0.97$). According to Equation 23, power-law index for this system is then expected to follow $\alpha = 0.85$. At the opposite end of the mass spectrum, the $v_{\text{circ}} = 50 \text{ km s}^{-1}$ dwarf galaxy, which obeys a very different Schmidt-Kennicutt relation ($n_{\text{tot}} \approx 4$) and $\Sigma_* - \Sigma_{\text{gas}}$ scaling ($\beta \sim 4$), has an expected $\alpha \approx 0.87$. These α values are remarkably close to the relation observed by Blitz & Rosolowsky (2006), who find $\alpha \approx 0.92$. That the ISRF model reproduces the observed correlation in galaxies of different masses then owes to the opposite compensating effects of the scaling of j with Σ_{gas} and the $\Sigma_* - \Sigma_{\text{gas}}$ scaling.

For the simulations that do not include an ISRF, the scaling between molecular fraction and pressure must be independent of the ISRF volume emissivity. We find that $f_{\text{H}_2} \sim \Sigma_{\text{gas}}^{0.6}$ in these galaxies, with significant scatter, which provides the much weaker relation $\Sigma_{\text{H}_2}/\Sigma_{\text{HI}} \sim P_{\text{ext}}^{0.4}$. The simulations without an ISRF have $f_{\text{H}_2} - P_{\text{ext}}$ scalings similar to this estimate or intermediate between this estimate and the observed relation.

The good agreement between the $f_{\text{H}_2} - P_{\text{ext}}$ scaling in the simulations with an ISRF and the observations provide an *a posteriori* justification for the chosen scaling of the ISRF strength in the simulations (Equation 2), even as the ISRF strength was physically motivated by the generation of soft UV photons by young stellar populations. The robustness of the $f_{\text{H}_2} - P_{\text{ext}}$ may be a consequence of the regulatory effects of

H_2 -destruction by the ISRF, which motivated in part the original calculations by Elmegreen (1993b), in concert with the influence of the external pressure (Elmegreen & Parravano 1994). However, we note that systems with a steep total gas Schmidt-Kennicutt relation, such as the $v_{\text{circ}} \sim 50 \text{ km s}^{-1}$ and $v_{\text{circ}} \sim 125 \text{ km s}^{-1}$ systems, do break from the $f_{\text{H}_2} - P_{\text{ext}}$ relation in the very exterior of the disk where the molecular fraction quickly declines. Observations of M33, the real galaxy analogue to the $v_{\text{circ}} \sim 125 \text{ km s}^{-1}$ simulated galaxy, indicate that the system may deviate from the observed $f_{\text{H}_2} - P_{\text{ext}}$ relation determined at higher surface densities in the very exterior of the disk (Gardan et al. 2007). The high-surface density regions of M33 do satisfy the $f_{\text{H}_2} - P_{\text{ext}}$ relation (Blitz & Rosolowsky 2006), as does the simulated M33 analogue. We delay a more thorough examination of the exterior disk regions until further work. In passing, we note that simulations of the molecular ISM using a sink particle method to represent dense clouds apparently can also reproduce the Blitz & Rosolowsky (2006) scaling (Booth et al. 2007), but as those simulations did not explicitly include an ISRF the interpretation of that simulated relation must differ than the interpretation provided above.

3.4. Star Formation and Angular Velocity

The star formation rate surface density Σ_{SFR} has been shown to correlate with the product of the gas surface density Σ_{gas} and the disk angular frequency Ω as

$$\Sigma_{\text{SFR}} \simeq C_{\Sigma\Omega} \Sigma_{\text{gas}} \Omega \quad (24)$$

with the constant $C_{\Sigma\Omega} = 0.017$ (Kennicutt 1998) and where the angular frequency is defined as

$$\Omega^2 = \frac{1}{R} \frac{d\Phi}{dR} \quad (25)$$

(e.g., §3.2.3 of Binney & Tremaine 1987). Star formation relations of this form have been forwarded to connect the star formation rate to the cloud-cloud collision time-scale (e.g., Wyse 1986; Wyse & Silk 1989; Tan 2000), to tie the gas consumption time-scale to the orbital time-scale (e.g., Silk 1997; Elmegreen 1997), or to reflect the correlation between the ISM density and the tidal density (Elmegreen 2002). These ideas posit that the $\Sigma_{\text{SFR}} - \Sigma_{\text{gas}} \Omega$ correlation provides a reasonable physical interpretation of the $\Omega \propto \sqrt{\rho}$ scaling. The correlation between star formation, surface density, and angular frequency can be examined in the simulated disk galaxies and compared with the star formation prescription used to determine the SFR during the disk evolution.

Figure 12 shows the star formation rate surface density Σ_{SFR} as a function of the total gas surface density consumed per orbit $0.017 \Sigma_{\text{gas}} \Omega$ and molecular gas surface density consumed per orbit $0.017 \Sigma_{\text{H}_2} \Omega$, compared to the observed $\Sigma_{\text{SFR}} = 0.017 \Sigma_{\text{gas}} \Omega$ relation Kennicutt (1998). The local values of Σ_{gas} and Σ_{H_2} are measured in radial annuli from the gas properties, while Ω is measured from the rotation curve at the same location. The normalization of the star formation rate in the simulations is effectively set by the choice of the star formation time-scale t_* , which is calibrated to recover star formation efficiency on the scale of molecular cloud complexes (Krumholz & McKee 2005; Krumholz & Tan 2007), and subsequently matches the observed disk-averaged Schmidt-Kennicutt relation (see §2.2).

Figure 12 shows that star formation surface density indeed scales as $\Sigma_{\text{gas}} \Omega$ at $\Sigma_{\text{SFR}} \gtrsim 5 \times 10^{-3} \text{ M}_\odot \text{ yr}^{-1} \text{ kpc}^{-2}$. The offset between the disk-averaged $\Sigma_{\text{SFR}} - \Sigma_{\text{gas}} \Omega$ relation found

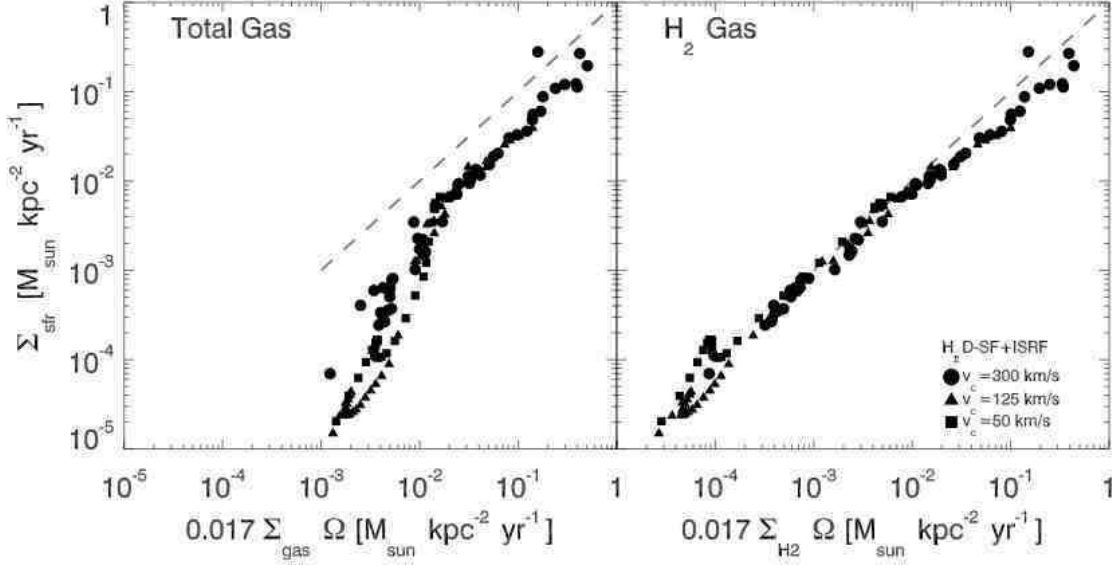


FIG. 12.— Star formation rate surface density Σ_{SFR} as a function of the total gas surface density consumed per orbit $C_{\Sigma\Omega}\Sigma_{\text{gas}}\Omega$ (left panel) and molecular gas surface density consumed per orbit $C_{\Sigma\Omega}\Sigma_{\text{H}_2}\Omega$ (right panel), where Ω is the orbital frequency and the efficiency $C_{\Sigma\Omega} = 0.017$ was determined from observations by Kennicutt (1998) (represented by the *dashed* line which extends over the range probed by observations). Shown are the local values of Σ_{gas} , Σ_{H_2} and Ω in annuli for galaxy models with circular velocities of $v_{\text{circ}} = 50 \text{ km s}^{-1}$ (squares), $v_{\text{circ}} = 125 \text{ km s}^{-1}$ (triangles), and $v_{\text{circ}} = 300 \text{ km s}^{-1}$ (circles) evolved with atomic+molecular cooling and destruction of H_2 by a local interstellar radiation field for $t = 0.3 \text{ Gyr}$. The star formation rate in the simulations display the correlations $\Sigma_{\text{SFR}} \propto \Sigma_{\text{H}_2}\Omega$ and, in the high surface density region where the molecular gas and total gas densities are comparable, $\Sigma_{\text{SFR}} \propto \Sigma_{\text{gas}}\Omega$.

by Kennicutt (1998) and the simulated relation may owe in part to the typically higher values of Ω in the disk interior that can affect the normalization of the azimuthally-averaged $\Sigma_{\text{SFR}} - \Sigma_{\text{gas}}\Omega$ relation. We note that this offset is comparable to the observed offset between the disk-averaged relation of Kennicutt (1998) and the spatially-resolved $\Sigma_{\text{SFR}} - \Sigma_{\text{gas}}\Omega$ relation found in M51a by Kennicutt et al. (2007). As in the previous sections, scaling $\Sigma_{\text{SFR}} - \Sigma_{\text{H}_2}\Omega$ works throughout the disk, while the $\Sigma_{\text{SFR}} - \Sigma_{\text{gas}}\Omega$ scaling steepens significantly at lower surface densities where the molecular fraction is declining.

That the star formation rate in the simulated disks correlates well with the quantity $\Sigma_{\text{gas}}\Omega$, even though the star formation rate in the simulations is determined directly from the *local* molecular gas density and the local gas dynamical time without direct knowledge of Ω , may be surprising. The correlation suggests that local gas density should scale with Ω , although the physical reason for such a correlation in our simulations is unclear. While previous examinations of the $\Sigma_{\text{SFR}} - \Sigma_{\text{gas}}\Omega$ correlation have developed explanations of why $\Omega \propto \sqrt{\rho_d}$, these simulations have a coarser treatment of the ISM than is invoked in such models; the molecular fraction and star formation rate are primarily functions of the local density. The $\Omega \sim \sqrt{\rho_d}$ correlation should then reflect the structural properties galaxy models rather than the detailed properties of the ISM that are somehow influenced by global processes in the disk.

The galaxy models used in the simulations remain roughly axisymmetric after their evolution, modulo spiral structure and disk instabilities. Hence, the fundamental equation that describes the gravitational potential Φ of the galaxies is the Poisson equation

$$\frac{d^2\Phi}{dz^2} + \frac{d^2\Phi}{dR^2} + \Omega^2 = 4\pi G\rho_{\text{total}}. \quad (26)$$

where the density ρ_{total} reflects the total density of the multi-component system. If the form of the potential generated by

ρ_{total} has the property that $\Omega^2 = (1/R)d\Phi/dR \propto \rho_d$, then the quantity $\Sigma_{\text{gas}}\Omega$ will mimic the scaling of Σ_{SFR} . In the second Appendix, we examine the solutions for Ω determined from Equation 26 for the limiting cases of locally disk-dominated ($\rho_{\text{total}} \approx \rho_{\text{disk}}$) and halo-dominated ($\rho_{\text{total}} \approx \rho_{\text{DM}}$) potentials, and show that typically $\Omega \propto \sqrt{\rho_d}B(\rho_d)$ where $B(\rho_d) \sim \mathcal{O}(1)$ is a weak function of density if the disk density is exponential with radius. This behavior suggests that whether the disk dominates the local potential, as is the case for massive galaxies, or the dark matter halo dominates the potential as it does in low-mass dwarfs, the angular frequency scales as $\Omega \propto \sqrt{\rho_d}$ throughout most of the disk. Based on these calculations, we conclude that the correlation $\Sigma_{\text{SFR}} \propto \Sigma_{\text{gas}}\Omega$ in the simulations is likely a consequence of the density-dependent star formation relation (Equation 4) and the galaxy structure inducing the correlation $\Omega \propto \sqrt{\rho_d}$. In other words, this correlation may be established during the formation of the exponential disk in the extended dark matter halo, and the correlation observed in real galaxies therefore may have a similar origin. Star formation may then correlate with $\Sigma_{\text{gas}}\Omega$, but this correlation does not necessarily mean that star formation is directly controlled or influenced by the global kinematics of the disk at the present time.

3.5. Star Formation and Critical Surface Density Thresholds

The connection between disk surface density, dynamical instabilities, and the formation of molecular clouds and stars has been thoroughly examined in the literature. A single-component thin disk will experience growing axisymmetric instabilities if its surface mass density exceeds the critical value Σ_Q , given by

$$\Sigma_Q(\sigma) \approx \frac{\alpha_Q \kappa \sigma}{\pi G}, \quad (27)$$

where κ is the epicyclic frequency

$$\kappa^2 = 2 \left(\frac{v^2}{R^2} + \frac{v}{R} \frac{dv}{dR} \right), \quad (28)$$

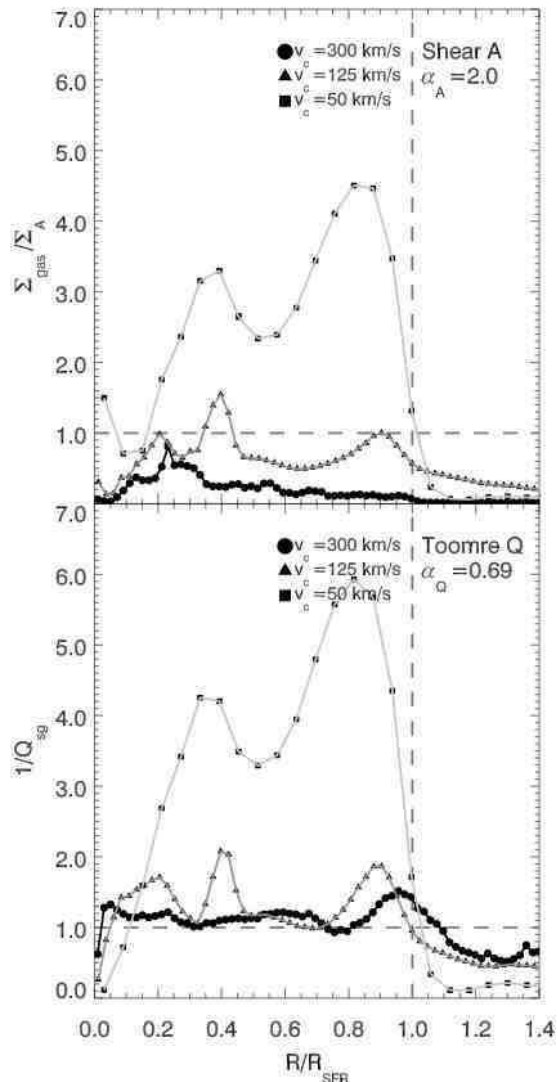


FIG. 13.— Stability parameters for two-fluid Toomre instability (Q_{sg}^{-1} , bottom panel) or shear instability ($\Sigma_{\text{gas}}/\Sigma_A$, top panel) as a function of radius normalized to the radius R_{SFR} containing 99.9% of the total active disk star formation. Shown are the parameters Q_{sg}^{-1} and $\Sigma_{\text{gas}}/\Sigma_A$ for galaxy models with circular velocities of $v_{\text{circ}} = 50 \text{ km s}^{-1}$ (squares, light gray lines), $v_{\text{circ}} = 125 \text{ km s}^{-1}$ (triangles, dark gray lines), and $v_{\text{circ}} = 300 \text{ km s}^{-1}$ (circles, black lines). The proportionality constants $\alpha_Q = 0.69$ and $\alpha_A = 2$ are taken to match the values used by Martin & Kennicutt (2001). For each simulated galaxy, the parameter Q_{sg}^{-1} approaches the transition to stability at the radius R_{SFR} beyond which only very little star formation operates. An increase in the stability against growing shearing modes also occurs near R_{SFR} for the simulated disks, but the transition is less uniform than for Toomre instability.

σ is the characteristic velocity dispersion of the fluid, and the parameter $\alpha_Q \sim \mathcal{O}(1)$ (Safronov 1960; Toomre 1964). For a two component system, consisting of stars with surface mass density Σ_* and velocity dispersion c_* , and gas with surface mass density Σ_{gas} and velocity dispersion σ , the instability criterion for axisymmetric modes with a wavenumber k can be expressed in terms of the normalized wavenumber $q \equiv kc_*/\kappa$ and the ratio of velocity dispersions $R \equiv \sigma/c_*$ as

$$Q_{\text{sg}}^{-1} \equiv \frac{2}{Q_s} \frac{q}{1+q^2} + \frac{2}{Q_g} R \frac{q}{1+q^2 R^2} > 1 \quad (29)$$

(Jog & Solomon 1984; Rafikov 2001), where $Q_s = \Sigma_Q(c_*)/\Sigma_*$ and $Q_g = \Sigma_Q(\sigma)/\Sigma_{\text{gas}}$. The most unstable wavenumber q can

be determined by maximizing this relation.

Elmegreen (1993a) considered another critical surface density Σ_A , given by

$$\Sigma_A \approx \frac{\alpha_A A \sigma}{\pi G} \quad (30)$$

where the parameter $\alpha_A \sim \mathcal{O}(1)$, and the Oort constant A is

$$A = -0.5R \frac{d\Omega}{dR} \quad (31)$$

(e.g., Binney & Tremaine 1987), above which shearing instabilities can grow by a large factor ($\gtrsim 100$) over a time interval $\Delta t \sim 2/A$.

Both axisymmetric and shearing instabilities can lead to a compression of the gas and, possibly, molecular cloud and star formation. Understanding the connection and interplay between global instabilities and star formation is important for understanding the complex dynamical processes operating in galactic disks (see, e.g., Elmegreen 2002, for a review). Observational evidence for such a connection has been a matter of debate. Kennicutt (1989) and Martin & Kennicutt (2001) found that the sites of active star formation corresponded to Toomre-unstable regions of the disks, and interpreted this observational correspondence as evidence that star formation is connected with disk instabilities on global scales. While Hunter et al. (1998) found the observed-to-critical surface density ratio for shearing instabilities provided a better indicator of star formation in low-mass (Im) galaxies than the one- and two-fluid axisymmetric instability parameters, they concluded that none of the instability criteria were particularly successful in predicting the locations of active star formation in such low-mass systems. Boissier et al. (2003) found that Q_g had uneven applicability as an indicator of star formation, even though a majority of their observational sample overlapped with that of Martin & Kennicutt (2001). However, when the stellar distribution was accounted for following Wang & Silk (1994), most of their sample had supercritical surface densities. Combining GALEX and IRAS observations with radio observations of gas and metal-abundance gradient determinations, Boissier et al. (2006) found that extinction-corrected UV emission was typically more extended than $\text{H}\alpha$ emission and considered this result evidence that observationally-inferred star formation thresholds are possibly affected by the identification of only $\text{H}\alpha$ -luminous regions as the sites of star formation. Kennicutt et al. (2007) examined the distribution Q_g in the star-forming regions of M51a and found the determination of “subcritical” regions may be influenced by gas detection limits. Recently, Yang et al. (2007) found that $\sim 85\%$ of young stellar objects in the LMC are found in regions that are Toomre-unstable given the two-component instability parameter Q_{sg} , and interpret this finding as evidence that instability “drives” star formation on global scales.

Given the differing conclusions determined from observations, it is interesting to use model galaxies to explore the role of critical surface densities in star formation. While proper radiative transfer calculations are needed to assign either $\text{H}\alpha$ or UV emissivities to the simulated disk galaxies, an indirect comparison between simulations and observations can be made by measuring surface mass densities, velocity dispersions, dynamical properties, and a characteristic extent of star formation in the model disks. These comparisons are presented in Figure 13, where the instability parameters Q_{sg}^{-1} and $\Sigma_{\text{gas}}/\Sigma_A$ are plotted as a function of radius in

the disk galaxies simulated with the H₂D-SF+ISRF molecular ISM and star formation model. For comparison with the two-fluid Toomre axisymmetric instability criterion, the parameter Q_{sg} is measured by determining the locally most unstable wavenumber q from Q_s and Q_g with $\alpha = 0.69$ to approximate the observational results of Kennicutt (1989) and Martin & Kennicutt (2001). When examining the shearing instability criterion, the parameter $\alpha_A = 2$ is chosen for comparison with the observational estimation of critical surface densities by Martin & Kennicutt (2001) and only the gas surface density is utilized. A “critical” radius R_{SFR} containing 99.9% of the total star formation in each simulated disk is measured and used as a proxy for the star formation threshold radius observationally determined from, e.g., the H α emission.

The shearing instability criterion (upper panel Figure 13) is supercritical ($\Sigma_{\text{gas}}/\Sigma_A > 1$) over the extent of star formation in the low-mass galaxy, but the larger galaxies are either marginally supercritical or subcritical. Given the large gas content in this dwarf system and that this comparison only uses the gas surface mass density Σ_{gas} , the result is unsurprising. While the $v_{\text{circ}} \sim 125 \text{ km s}^{-1}$ and $v_{\text{circ}} \sim 300 \text{ km s}^{-1}$ galaxies are subcritical at $R = R_{\text{SFR}}$, we note that there is still a noticeable drop in $\Sigma_{\text{gas}}/\Sigma_A$ near $R = R_{\text{SFR}} \sim 1$ for these systems.

Interestingly, with the chosen definition of R_{SFR} , the bottom panel of Figure 13 shows that the two-component Toomre instability parameter Q_{sg} is a remarkably accurate indicator of where the majority of star formation operates in the simulated disk galaxies. Each galaxy approaches the $Q_{\text{sg}} \sim 1$ transition near R_{SFR} , demonstrating that much of the star formation is operating within Toomre-unstable regions of the disks. These results appear most consistent with the observations by Kennicutt (1989), Martin & Kennicutt (2001), and Yang et al. (2007), who find that star formation operates most efficiently in regions that are gravitationally unstable.

Our simulations are also qualitatively consistent with the theoretical findings of Li et al. (2005a,b, 2006), who used hydrodynamical simulations of isolated galaxies with sink particles to represent dense molecular gas and star clusters. They found that if the accretion onto the sink particles resulted in star formation with some efficiency, the two-component Toomre parameter was $Q_{\text{sg}} < 1.6$ in regions of active star formation. Although a direct comparison is difficult given their use of sink particles, we similarly find that the majority of star formation in our simulations occurs in regions of the disk where $Q_{\text{sg}} \lesssim 1$.

In related theoretical work, a gravothermal instability criterion for star formation was explored by Schaye (2004), who suggested that the decrease in thermal velocity dispersion associated with the atomic-to-molecular transition in the dense ISM may induce gravitational instability and the corresponding connection between critical surface densities and star formation. The simulated galaxies do experience a decline in thermal sound speed near the $Q_{\text{sg}} \sim 1$ transition, consistent with the mechanism advocated by Schaye (2004). However, the sharp decline in Q_{sg} at the critical radius in the semi-analytical calculations of Schaye (2004) implies that the development of the cold phase triggers gravitational instability. Of our H₂D-SF+ISRF simulations, only the dwarf galaxy model displays a sharp transition in Q_{sg} near the critical radius while the stability of the other, more massive galaxies are more strongly influenced by the turbulent gas velocity dispersion and have more modest increases in Q_{sg} . The role of ther-

mal instability in driving gravitational instability is therefore not as pronounced in our simulations than in the analytical models of Schaye (2004), even though simulations do include physics required for modeling it. Further, we note that the gravothermal mechanism suggested by Schaye (2004) does not operate in isothermal treatments of the ISM such as those presented by Li et al. (2005a,b, 2006). Similarly our GD-SF simulations, which are effectively isothermal ($T \approx 10^4 \text{ K}$) at ISM densities, display similar transitions to $Q_{\text{sg}} \lesssim 1$ at the critical radius even as such simulations do not include a cold phase to drive gravitational instability.

We stress that the definition of R_{SFR} may affect conclusions about the importance of threshold surface densities. For instance, if a 90% integrated star formation threshold was used R_{SFR} would be lowered to 0.3–0.6 of the chosen value and the subsequent interpretations about the applicability of the instability parameter Q_{sg} could be quite different. Detailed radiative transfer calculations may therefore be necessary to determine the integrated star formation fraction that brings R_{SFR} in the best agreement with observationally-determined critical radii. We also note that the Schmidt-Kennicutt relations of the simulated galaxies (§3.2.1 and §3.2.2) are entirely consistent with the Boissier et al. (2006) Schmidt-Kennicutt relation determinations, even as their observations do not show evidence for critical surface density thresholds for star formation.

3.6. Temperature and Density Structure of the ISM

The temperature and density structure of interstellar gas is determined by a variety of processes including radiative heating, cooling, and, importantly, turbulence (see, e.g., Elmegreen 2002). Many theoretical calculations that model the cold, dense medium that hosts star formation as a turbulent gas have provided important insights about the process of star formation in molecular clouds. For instance, the calculation of the density probability distribution function (PDF) of an isothermal gas, defined as a volume fraction of gas with a given density, suggests that the PDF will resemble a lognormal distribution with a dispersion σ that scales linearly with the mean gas Mach number $\sigma \propto \beta \mathcal{M}$. The origin of the lognormal form is discussed in detail in Padoan et al. (1997) and Passot & Vázquez-Semadeni (1998), and primarily owes to the random sequence of shocks and rarefactions in the pressure-regulated isothermal ISM that leads to a logarithmically-symmetric distribution of densities. For a non-isothermal gas, however, the density PDF may more generally follow a power-law distribution (Passot & Vázquez-Semadeni 1998; Scalo et al. 1998).

Although the lognormal PDF was initially discussed in the context of molecular clouds, Wada & Norman (2001) found that two-dimensional numerical simulations of a multiphase ISM on galactic scales produced a lognormal density PDF for dense gas (at low densities gas followed a flatter distribution in $\log \rho$). A similar PDF was found in a cosmological simulation of galaxy formation at $z \approx 4$ by Kravtsov (2003). Motivated by the result of Wada & Norman (2001), Elmegreen (2002) suggested that the Schmidt-Kennicutt relation could be explained in terms of the density PDF of ISM gas if a fraction f_c of gas that resides above some critical density threshold ρ_c converts into stars with a constant efficiency and ρ_c scales linearly with the average ISM density $\langle \rho \rangle$.

Subsequent theoretical studies of the density PDF in the ISM have examined the connection between the abundance of dense gas and the scaling of the Schmidt-Kennicutt relation. For instance, Kravtsov (2003) found that the fraction of

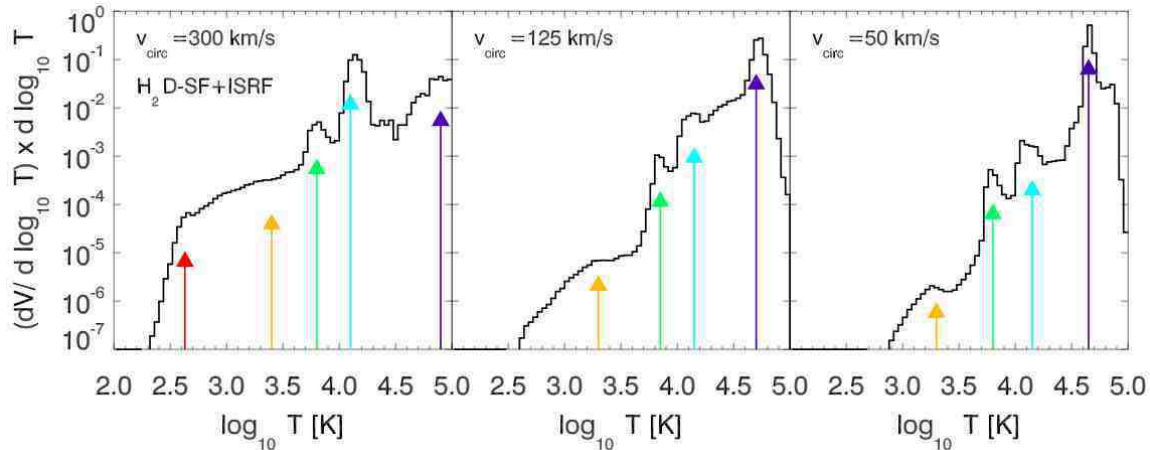


FIG. 14.— Temperature structure of the interstellar medium in galaxies with different masses. Shown is the probability distribution function (PDF) of the fractional volume of the ISM with a temperature T (black histograms), for systems with circular velocities of $v_{\text{circ}} = 300 \text{ km s}^{-1}$ (left panel), $v_{\text{circ}} = 125 \text{ km s}^{-1}$ (middle panel), and $v_{\text{circ}} = 50 \text{ km s}^{-1}$ (right panel). The simulations use an ISM and star formation model that follows the molecular hydrogen abundance, low-temperature ($T > 10^2 \text{ K}$) cooling, and H_2 -destruction by an interstellar radiation field (the $\text{H}_2\text{D-SF+ISRF}$ model) to evolve the systems in isolation for $t = 0.3 \text{ Gyr}$. The peaks in the temperature PDF correspond to regions of density-temperature phase space where the cooling time t_{cool} has local maxima (i.e., where t_{cool} is locally a weak function of density). These peaks in the temperature PDF correspond to features in the density PDF, and the colored arrows highlight regions that can be modeled roughly as separate isothermal phases (i.e., lognormals) in the density PDF (see Figure 15 and §3.6 the text for details).

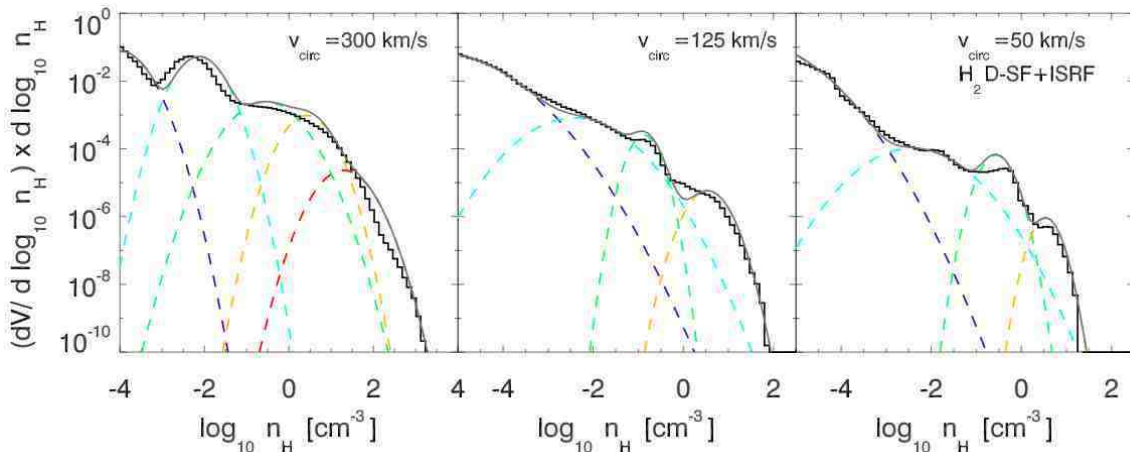


FIG. 15.— Density structure of the interstellar medium in galaxies with different masses. Shown is the probability distribution function (PDF) of the fractional volume of the ISM with a density n_{H} (black histograms), for systems with circular velocities of $v_{\text{circ}} = 300 \text{ km s}^{-1}$ (left panel), $v_{\text{circ}} = 125 \text{ km s}^{-1}$ (middle panel), and $v_{\text{circ}} = 50 \text{ km s}^{-1}$ (right panel) for the $\text{H}_2\text{D-SF+ISRF}$ model at $t = 0.3 \text{ Gyr}$. The features in the density PDF correspond to regions of density-temperature phase space where the cooling time t_{cool} has local maxima (i.e., where t_{cool} is locally a weak function of density). The density PDF of the ISM in these simulated galaxies is not well-modeled by an isothermal gas (i.e., a single lognormal), except at the high-density tail, which reflects its multiphase structure. The density PDF may be modeled approximately as a collection of isothermal phases (i.e., lognormal PDFs in density, colored dashed lines), where the characteristic density of each phase is determined by using the ISM equation-of-state to find the typical density of peaks in the temperature PDF (see Figure 14 and §3.6 the text for details).

dense gas in cosmological simulations of disk galaxy formation at redshifts $z \gtrsim 4$ varied with the surface density in a manner to produce the $\Sigma_{\text{SFR}} \propto \Sigma_{\text{gas}}^{1.4}$ Schmidt-Kennicutt relation at high surface densities. Recently, further hydrodynamical simulations on galactic scales have been used to examine the temperature and density structure of the ISM. Tasker & Bryan (2006) used simulations of isolated disk galaxies to show that the multiphase ISM that developed obtained a pressure equilibrium, with a characteristic pressure that varied throughout the disks. Joungh & Mac Low (2006) used three-dimensional models of the stratified ISM to demonstrate that supernovae explosions can act to regulate star formation by inputting energy on small scales. Their scheme produced temperature and density structures consistent with those observed in the real ISM, with density and temperature PDFs that contain multiple peaks. Wada & Norman (2007) revisited their previous calcu-

lations with updated, three-dimensional simulations of galactic disks and found that the ISM densities in their simulated galaxies were well-described by a single lognormal distribution over roughly six orders of magnitude in density, although at smaller densities PDF is flat and exhibits broad peaks. They also argue that width of the lognormal increases with the increasing gas fraction of the disk, but the presented results span only a fraction of the disk rotational period and it is not clear whether the PDF has reached a steady state. Based on their simulation results they develop a model for the star formation efficiency in disks of different masses, assuming these disks are well-approximated by a single lognormal density distribution (see also the original model by Elmegreen 2002). Tasker & Bryan (2007) found the density PDF in their multiphase simulations could be approximated by a single lognormal at high densities, but exhibited deviations from the

lognormal in the form of peaks and dips at smaller densities.

Figure 14 shows the probability distribution function (PDF) of the fractional volume in the ISM at a temperature T in the $\text{H}_2\text{D-SF+ISRF}$ simulations at $t = 0.3\text{Gyr}$. The temperature PDF is measured by assigning an effective volume to each particle based on its mass and density, counting the particles in bins of fixed width in $\log_{10} T$, and then normalizing by the total effective volume of the ISM. The temperature PDF displays structure corresponding to gas at several phases. These temperature peaks correspond to features in the density-temperature phase diagram of the ISM, set by the cooling and heating processes. The abundance of gas in different regions of this diagram depend on the local cooling time, with regions corresponding to long local cooling times becoming more populated. The overall gravitational potential of the system also influences the density of gas in the disks and thus indirectly influences cooling and abundance of cold, dense gas, as denser ISM gas can reach lower equilibrium temperatures. Figure 14 shows that the temperature PDFs of the galaxies do differ, with more massive galaxies containing more volume at low ISM temperatures. In smaller mass galaxies, the ISM densities are lower, gas distributions are more extended, and the abundance of cold gas is greatly decreased.

Generally, the temperature and density structure of the ISM should be connected. As discussed above, the functional form of the density PDF reflects the temperature distribution of the gas, with isothermal gas maintaining a lognormal distribution (e.g., Padoan et al. 1997; Passot & Vázquez-Semadeni 1998) or, more generally, power-law-like distributions (e.g., Passot & Vázquez-Semadeni 1998; Scalo et al. 1998). Figure 15 shows the PDF of gas densities for each model galaxy in the $\text{H}_2\text{D-SF+ISRF}$ model at $t = 0.3\text{Gyr}$. The density PDFs are measured in the same manner as the temperature PDFs, but the particles are binned according to the $\log_{10} n_{\text{H}}$. Each galaxy has a PDF with noticeable features that change depending on the galaxy mass scale. None of the density PDFs are well represented by a single lognormal distribution, reflecting the multiple peaks apparent in the temperature PDFs (Figure 14).

Motivated by the multiple temperature structure of the ISM displayed in Figure 14, a rough model of the density PDFs can be constructed by identifying characteristic temperature peaks in the temperature PDF and assigning separate lognormal distributions to represent each gas phase, which are approximately isothermal for their respective temperatures. The colored arrows in Figure 14 identify characteristic temperatures in the ISM of each galaxy. The characteristic density corresponding to each selected temperature, determined by the median equation-of-state calculated using Cloudy, is employed as the mean of a lognormal distribution used to model a feature in the density PDF (colored dashed lines in Figure 15). The heights and widths of the lognormals are constrained to provide the same relative volume fraction in the density PDFs as the phase occupies in the temperature PDF, resulting in a model shown by the solid gray lines in Figure 15.

Clearly the ISM is best understood in terms of a continuous distribution of temperatures, represented in the simulations by Figure 14, but the multiphase model of the density PDFs provides some conceptual insight into the ISM phase structure. First, the model of separate isothermal ISM phases can capture the prominent features of the density PDFs. Second, the galaxies share common features in the density (and temperature) PDFs, such as a warm neutral phase ($\log_{10} T \sim 3.8$) and the mix of cold neutral and molecular gas at low tem-

peratures ($\log_{10} T \lesssim 3.5$). Third, the relative widths of the lognormal distributions representing the dense ISM in each galaxy increase with increasing galaxy mass (i.e., the orange lognormals centered near $\log_{10} n_{\text{H}} \sim 0.5$), as do their normalizations. The increasing widths of the lognormals mimic the increasing velocity dispersions (and turbulent Mach numbers) of the dense gas in the more massive galaxy models.

Note that for the ISM of the $v_{\text{circ}} = 300\text{km s}^{-1}$ system the cold dense phase contributes the majority of the ISM by mass, while shock heated gas at $T \sim 10^5\text{K}$ contributes the largest ISM fraction by volume. We note that this result qualitatively resembles the effect of the volume-averaged equation-of-state utilized in subgrid models of the multiphase ISM (e.g. Springel & Hernquist 2003a).

For purposes of calculating the overall efficiency of star formation of galaxies, our results suggest that approximating the density PDF by a single lognormal distribution may be overly simplistic. The detailed shape of the PDF is set by global properties of galaxies and heating and cooling processes in their ISM and can therefore be expected to vary from system to system. Nevertheless, a single PDF modeling may be applicable for the cases when most of the ISM mass is in one dominant gas phase (e.g., dense cold gas), as is the case for the massive galaxy in our simulations. We leave further exploration of this subject for future work.

4. DISCUSSION

Results presented in the previous sections indicate that star formation prescriptions based on the local abundance of molecular hydrogen lead to interesting features of the global star formation relations.

Our study is complementary to other recent theoretical models of H_2 -based star formation. Pelupessy et al. (2006) study formation of molecular gas in dwarf galaxies using a dynamical, non-equilibrium model of molecular hydrogen formation with a subgrid model for the formation of molecular clouds. However, they do not focus on global star formation relations, which is the main focus on our study.

Booth et al. (2007) present a model of star formation based on a subgrid model for the formation of molecular clouds from thermally unstable gas in a multiphase ISM. In their model, molecular clouds are represented as ballistic particles which can coagulate through collisions. This treatment differs from our model, as we do not attempt to model molecular clouds as special objects. Instead, our goal is to follow the dynamics and thermodynamics of the gas self-consistently and calculate the equilibrium abundance of molecular hydrogen using the local gas properties. The global Schmidt-Kennicutt relation in simulations of Booth et al. (2007) does not show a break or steepening down to very small surface densities ($\Sigma \approx 10^{-2} \text{M}_{\odot} \text{pc}^{-2}$; see their Fig. 15). Their simulations results differ from the results of our model that generally predict strong deviations from Schmidt-Kennicutt relation at low surface densities and declining molecular fractions. Also, Booth et al. (2007) show that their simulations also reproduce the molecular fraction-pressure relation of Blitz & Rosolowsky (2004, 2006). However, as we note in § 3.3, the interpretation of this relation in their model must be different from our interpretation involving the relation between the gas surface density, the stellar surface density, and the ISRF strength. Given the differences, it will be interesting to compare results of different models of H_2 -based star formation in more detail in future studies.

We show that the inclusion of an interstellar radiation field

is critical to control the amount of diffuse H_2 at low gas densities. For instance, without a dissociating ISRF the low mass dwarf galaxy eventually becomes almost fully molecular, in stark contrast with observations. We also show that without the dissociating effect of the ISRF our model galaxies produce a much flatter relation between molecular fraction f_{H_2} and pressure P_{ext} , as can be expected from the results of Elmegreen (1993a). Including H_2 -destruction by an ISRF results in a $f_{H_2} - P_{\text{ext}}$ relation in excellent agreement with the observations of Wong & Blitz (2002) and Blitz & Rosolowsky (2004, 2006).

Our model also predicts that the relation between Σ_{SFR} and Σ_{gas} should not be universal and can be considerably steeper than the canonical value of $n_{\text{tot}} = 1.4$, even if the three-dimensional Schmidt relation in molecular clouds is universal. The slope of the relation is controlled by the dependence of molecular fraction (i.e., fraction of star forming gas) on the total local gas surface density. This relation is non-trivial because the molecular fraction is controlled by pressure and ISRF strength, and can thus vary between different regions with the same total gas surface density. The relation can also be different in the regions where the disk scale-height changes rapidly (e.g., in flaring outer regions of disks), as can be seen from equation 15 (see also Schaye & Dalla Vecchia 2007). We show that the effect of radial variations in the molecular fraction f_{H_2} and gas scale heights (h_{SFR} and h_{gas}) on the star formation rate can be accounted for in terms of a structural, Schmidt-Kennicutt-like correlation, $\Sigma_{\text{SFR}} \propto f_{H_2} h_{\text{SFR}} h_{\text{gas}}^{-1.5} \Sigma_{\text{gas}}^{1.5}$, that trivially relates the local star formation rate to the consumption of molecular gas with an efficiency that scales with the local dynamical time.

A generic prediction of our model is that deviations from the Schmidt-Kennicutt $\Sigma_{\text{SFR}} - \Sigma_{\text{gas}}$ relation are expected in galaxies or regions of galaxies where the molecular fraction is declining or much below unity. As we discussed above, star formation in the molecule-poor ($f_{H_2} \sim 0.1$) galaxy M33 supports this view as its total gas Schmidt-Kennicutt power-law index is $n_{\text{tot}} \approx 3.3$ (Heyer et al. 2004). While our simulations of an M33 analogue produce a steep Schmidt-Kennicutt power-law, the overall star formation efficiency in our model galaxies lies below that observed for M33. However, as recently emphasized by Gardan et al. (2007), the highest surface density regions of M33 have unusually efficient star formation compared with the normalization of the Kennicutt (1998) relation and so the discrepancy between the normalization of star formation in our simulations and in observations of M33 is not surprising. Given that dwarf galaxies generally have low surface densities and are poor in molecular gas, it will be interesting to examine Schmidt-Kennicutt relation in other small-mass galaxies.

Another example of a low-molecular fraction galaxy close to home is M31, which has only a fraction $f_{H_2} \approx 0.07$ of its gas in molecular form within 18 kpc of the galactic center (Nieten et al. 2006). Our model would predict that this galaxy should deviate from the total gas Schmidt-Kennicutt relation found for molecular-rich galaxies. Observationally, the Schmidt-Kennicutt relation of M31 measured by Boissier et al. (2003) is rather complicated and even has an increasing SFR with decreasing gas density over parts of the galaxy. Low molecular fractions can also be expected in the outskirts of normal galaxies and in the disks of low surface brightness galaxies. The latter have molecular fractions of only $f_{H_2} \lesssim 0.10$ (Matthews et al. 2005; Das et al. 2006), and we therefore predict that they will not follow the total gas

Schmidt-Kennicutt relation obeyed by molecule-rich, higher surface density galaxies. At the same time, LSBs do lie on the same relation between H_2 mass and far infrared luminosity as higher surface brightness (HSB) galaxies (Matthews et al. 2005), which suggests that the dependence of star formation on molecular gas may be the same in both types of galaxies. Our model predicts that the $\Sigma_{\text{SFR}} - \Sigma_{H_2}$ correlation will have a consistent value of $n_{\text{mol}} \sim 1.4$ between LSB and HSB galaxies.

An alternative formulation of the global star formation relation is based on the angular frequency of disk rotation: $\Sigma_{\text{SFR}} \propto \Sigma_{\text{gas}} \Omega$. That this relation works in real galaxies is not trivial, because star formation and dynamical time-scale depend on the local gas density, while Ω depends on the total mass distribution *within* a given radius. Although several models were proposed to explain such a correlation (see, e.g., Kennicutt 1998; Elmegreen 2002, for reviews), we show in §3.4 and the second Appendix that the star formation correlation with Ω can be understood as a fortuitous correlation of Ω with gas density of $\Omega \propto \rho_{\text{gas}}^\alpha$, where $\alpha \approx 0.5$, for self-gravitating exponential disks or exponential disks embedded in realistic halo potentials. Moreover, we find that $\Sigma_{\text{SFR}} \propto \Sigma_{\text{gas}} \Omega$ breaks down at low values of $\Sigma_{\text{gas}} \Omega$ where the molecular fraction declines, similarly to the steepening of the Schmidt-Kennicutt relation. Our models therefore predict that the $\Sigma_{\text{SFR}} \propto \Sigma_{H_2} \Omega$ relation is more robust than the $\Sigma_{\text{SFR}} \propto \Sigma_{\text{gas}} \Omega$ relation.

An important issue related to the global star formation in galaxies is the possible existence of star formation thresholds (Kennicutt 1998; Martin & Kennicutt 2001). Such thresholds are expected to exist on theoretical grounds, because the formation of dense, star-forming gas is thought to be facilitated by either dynamical instabilities (see, e.g., Elmegreen 2002; McKee & Ostriker 2007, for comprehensive reviews) or gravithermal instabilities (Schaye 2004). We find that the two-component Toomre instability threshold that accounts for both stars and gas, $Q_{\text{sg}} < 1$, works well in predicting the transition from atomic gas, inert to star formation, to the regions where molecular gas and star formation occur in our simulations. Our results are in general agreement with Li et al. (2005b,a, 2006), who used sink-particle simulations of the dense ISM in isolated galaxies to study the relation between star formation and the development of gravitational instabilities, and with observations of star formation in the LMC (Yang et al. 2007). Our simulations further demonstrate the importance of accounting for all mass components in the disk to predict correctly which regions galactic disks are gravitationally unstable.

Given that our star formation prescription is based on molecular hydrogen, the fact that Q_{sg} is a good threshold indicator may imply that gravitational instabilities strongly influence the abundance of dense, molecular gas in the disk. Conversely, the gas at radii where the disk is stable remains at low density and has a low molecular fraction. We find that in our model galaxies, the shear instability criterion of Elmegreen (1993a) does not work as well as the Toomre Q_{sg} -based criterion. Almost all of the star formation in our model galaxies occurs at surface densities $\Sigma_{\text{gas}} \gtrsim 3 M_\odot \text{pc}^{-2}$, which is formally consistent with the Schaye (2004) constant surface density criterion for gravithermal instability. However, as Figure 8 shows, we do not see a clear indication of threshold at a particular surface density and our GD-SF models that have an effectively isothermal ISM with $T \approx 10^4 \text{K}$ (and hence do not have a gravithermal instability) still show a good corre-

lation between regions where $Q_{\text{sg}} < 1$ and regions where star formation operates.

Our results have several interesting implications for interpretation of galaxy observations at different epochs. First, low molecular fractions in dwarf galaxies mean that only a small fraction of gas is participating in star formation at any given time. This connection between star formation efficiency and molecular hydrogen abundance may explain why dwarf galaxies are still gas rich today compared to larger mass galaxies (Geha et al. 2006), without relying on mediation of star formation or gas blowout by supernovae. Note that a similar reasoning may also explain why large LSBs at low redshifts are gas rich but anemic in their star formation. Understanding star formation and evolution of dwarf galaxies is critical because they serve as the building blocks of larger galaxies at high redshifts. Such small-mass galaxies are also expected to be the first objects to form large masses of stars and should therefore play an important role in enrichment of primordial gas and the cosmic star formation rate at high redshifts (Hopkins 2004; Hopkins & Beacom 2006).

At early epochs, the star-forming disks at $z \sim 2$ that may be progenitors of low-redshift spiral galaxies are observed to lack centrally-concentrated bulge components (Elmegreen et al. 2007). Given that galaxies are expected to undergo frequent mergers at $z > 2$, bulges should have formed if a significant fraction of baryons are converted into stars during such mergers (e.g., Gnedin et al. 2000). The absence of the bulge may indicate that star formation in the gas rich progenitors of these $z \sim 2$ systems was too slow to convert a significant fraction of gas into stars. This low star formation efficiency can be understood if the high cosmic UV background, low-metallicities, and low dust content of high- z gas disks keep their molecular fractions low (Pelupessy et al. 2006), thereby inhibiting star formation over most of gas mass and keeping the progenitors of the star-forming $z \sim 2$ disks mostly gaseous. Gas-rich progenitors may also help explain the prevalence of extended disks in low-redshift galaxies despite the violent early merger histories characteristic of Λ CDM universes, as gas-rich mergers can help build high-angular momentum disk galaxies (Robertson et al. 2006a). Mergers of mostly stellar disks, on the other hand, would form spheroidal systems.

Our results may also provide insight into the interpretation of the results of Wolfe & Chen (2006), who find that the star formation rate associated with neutral atomic gas in damped Lyman alpha (DLA) systems is an order of magnitude lower than predicted by the local Kennicutt (1998) relation. The DLAs in their study sample regions with column densities $N_{\text{H}} \approx 2 \times 10^{21} \text{ cm}^{-2}$, or surface gas densities of $\Sigma_{\text{DLA}} \approx 20 M_{\odot} \text{ pc}^{-2}$, assuming a gas disk with a thickness of $h \approx 100 \text{ pc}$. Suppose the local Schmidt-Kennicutt relation steepens from the local relation with the slope $n_0 = 1.4$ to a steeper slope n_1 below some surface density $\Sigma_{\text{b}} > \Sigma_{\text{DLA}}$. Then for $\Sigma_{\text{gas}} < \Sigma_{\text{b}}$, the star formation rate density will be lower than predicted by the local relation by a factor of $(\Sigma_{\text{gas}}/\Sigma_{\text{b}})^{n_1-n_0}$. For $n_0 = 1.4$ and $n_1 = 3$ the star formation rate will be suppressed by a factor of > 10 for $\Sigma_{\text{gas}}/\Sigma_{\text{b}} < 0.25$. Thus, the results Wolfe & Chen (2006) can be explained if the total gas Schmidt-Kennicutt relation at $z \sim 3$ steepens below $\Sigma_{\text{gas}} \lesssim 100 M_{\odot} \text{ pc}^{-2}$.

Our results also indicate that the thermodynamics of the ISM can leave an important imprint on its density probability distribution. Each thermal phase in our model galaxies has its own lognormal-like density distribution. The density PDF and its dependence on the local conditions ultimately

control the relation between fraction of mass in the dense, star-forming gas and the mean density in a given large patch of the ISM (Elmegreen 2002). Our results imply that using a single lognormal PDF to build a model of global star formation in galaxies (e.g., Elmegreen 2002; Wada & Norman 2007) is probably an oversimplification. Instead, the global star formation relation may vary depending on the dynamical and thermodynamical properties of the ISM. We can thus expect differences in the star formation efficiency between the low-density and low-metallicity environments of dwarf and high-redshift galaxies and the higher-metallicity, denser gas of many large nearby spirals. Note that many of the results and effects we discuss above may not be reproduced with a simple 3D density threshold for star formation, as commonly implemented in galaxy formation simulations. Such a threshold can reproduce the atomic-to-molecular transition only crudely and would not include effects of the local interstellar radiation field, metallicity and dust content, etc.

A clear caveat for our work is that the simulation resolution limits the densities we can model correctly. At high densities, the gas in our simulations is over-pressurized to avoid numerical Jeans instability. The equilibrium density and temperature structure of the ISM and the molecular fraction are therefore not correct in detail. Note, however, that our pressurization prescription is designed to scale with the resolution, and will converge to the “correct” result as the resolution improves. In any event, the simulations likely do not include all the relevant physics shaping density and temperature PDFs of the ISM in real galaxies. The results may obviously depend on other microphysics of the ISM as they influence both the temperature PDF and the fraction of gas in a high-density, molecular form. Future simulations of the molecular ISM may need to account for new microphysics as they resolve scales where such processes become important.

5. SUMMARY

Using hydrodynamical simulations of the ISM and star formation in cosmologically motivated disk galaxies over a range of representative masses, we examine the connection between molecular hydrogen abundance and destruction, observed star formation relations, and the thermodynamical structure of the interstellar medium. Our simulations provide a wide variety of new insights into the scale-dependency of star formation efficiency in galaxies. A summary of our methodology and results follows.

1. A model of heating and cooling processes in the interstellar medium (ISM), including low-temperature coolants, dust heating and cooling processes, and heating by the cosmic UV background, cosmic rays, and the local interstellar radiation field (ISRF), is calculated using the photoionization code Cloudy (Ferland et al. 1998). Calculating the molecular fraction of the ISM enables us to implement a prescription for the star formation rate (SFR) that ties the SFR directly to the molecular gas density. The ISM and star formation model is implemented in the SPH/N-body code GADGET2 (Springel 2005) and used to simulate the evolution of isolated disk galaxies.
2. We study the correlations between gas surface density (Σ_{gas}), molecular gas surface density (Σ_{H_2}), and SFR surface density (Σ_{SFR}). We find that in our most realistic model that includes heating and destruction of

- H_2 by the interstellar radiation field, the $\Sigma_{\text{SFR}} \propto \Sigma_{\text{gas}}^{n_{\text{tot}}}$ relation measured in annuli is power law with an index n_{tot} that varies from $n_{\text{tot}} \sim 2$ in massive galaxies to $n_{\text{tot}} \gtrsim 4$ in small mass dwarfs. The corresponding slope of the $\Sigma_{\text{SFR}} \propto \Sigma_{\text{H}_2}^{n_{\text{mol}}}$ molecular-gas Schmidt-Kennicutt relation is approximately the same for all galaxies, with $n_{\text{mol}} \approx 1.3$. These results are consistent with observations of star formation on a variety of scales (e.g., Kennicutt 1998; Wong & Blitz 2002; Boissier et al. 2003; Heyer et al. 2004; Boissier et al. 2006; Kennicutt et al. 2007).
3. In our models, the SFR density scales as $\Sigma_{\text{SFR}} \propto f_{\text{H}_2} h_{\text{SFR}} h_{\text{gas}}^{-1.5} \Sigma_{\text{gas}}^{1.5}$, where h_{gas} is the scale-height of the ISM and h_{SFR} is the scale-height of star-forming gas. The different $\Sigma_{\text{SFR}} - \Sigma_{\text{gas}}$ relations in galaxies of different mass and in regions of different surface density in our models therefore owe to the dependence of molecular fraction f_{H_2} and scale height of gas on the gas surface density.
 4. We show that the $\Sigma_{\text{SFR}} \propto \Sigma_{\text{gas}} \Omega$ and $\Sigma_{\text{SFR}} \propto \Sigma_{\text{H}_2} \Omega$ correlations describe the simulations results well where the molecular gas and total gas densities are comparable, while the simulations deviate from $\Sigma_{\text{SFR}} \propto \Sigma_{\text{gas}} \Omega$ (e.g., Kennicutt 1998) at low Σ_{gas} owing to a declining molecular fraction. We demonstrate that these relations may owe to the fact that the angular frequency and the disk-plane gas density are generally related as $\Omega \propto \sqrt{\rho}$ for exponential disks if the potential is dominated by either the disk, a Navarro et al. (1996) halo, Hernquist (1990) halo, or an isothermal sphere. The correlation of Σ_{SFR} with Ω is thus a secondary correlation in the sense that $\Omega \propto \sqrt{\rho}$ is set during galaxy formation and Ω does not directly influence star formation.
 5. The role of critical surface densities for shear instabilities (Σ_A) and Toomre (1964) instabilities (Σ_Q) in star formation (e.g., Martin & Kennicutt 2001) is examined in the context of the presented simulations. We find that the two-component Toomre instability criterion $Q_{\text{sg}} < 1$ is an accurate indicator of the star-forming regions of disks, and that gravitational instability and star formation are closely related in our simulations. Further, the Q_{sg} criterion works even in simulations in which cooling is restricted to $T > 10^4$ K where gravothermal instability cannot operate.
 6. Our simulations that include H_2 -destruction by an ISRF naturally reproduce the observed scaling $f_{\text{H}_2} \propto P_{\text{ext}}^{0.9}$ between molecular fraction and external pressure (e.g., Wong & Blitz 2002; Blitz & Rosolowsky 2004, 2006), but we find that simulations without an ISRF have a weaker scaling $f_{\text{H}_2} \propto P_{\text{ext}}^{0.4}$. We calculate how the connection between the scalings of the gas surface density, the stellar surface density, and the ISRF strength influence the $f_{\text{H}_2} - P_{\text{ext}}$ relation in the ISM, and show how the simulated scalings reproduce the $f_{\text{H}_2} - P_{\text{ext}}$ relation even as the power-law index of the total gas Schmidt-

Kennicutt relation varies dramatically from galaxy to galaxy.

7. We present a methodology for mitigating numerical Jeans fragmentation in Smoothed Particle Hydrodynamics simulations that uses a density-dependent pressurization of gas on small scales to ensure that the Jeans mass is properly resolved, similar to techniques used in grid-based simulations (e.g., Truelove et al. 1997; Machacek et al. 2001). The gas internal energy u at the Jeans scale is simply scaled as $u \propto m_{\text{Jeans}}^{-2/3}$, where m_{Jeans} is the local Jeans mass, to ensure the Jeans mass is resolved by some N_{Jeans} number of SPH kernel masses $2N_{\text{neigh}} m_{\text{SPH}}$, where N_{neigh} is the number of SPH neighbor particles and m_{SPH} is the gas particle mass. For the simulations presented here, we find the Bate & Burkert (1997) criterion of $N_{\text{Jeans}} = 1$ to be insufficient to avoid numerical fragmentation and that $N_{\text{Jeans}} \sim 15$ provides sufficient stability against numerical fragmentation over the time evolution of our simulations. Other simulations may have more stringent resolution requirements. We also demonstrate that isothermal galactic disks with temperatures of $T = 10^4$ K may be susceptible to numerical Jeans instabilities at resolutions common in cosmological simulations of disk galaxy formation, and connect this numerical effect to possible angular momentum deficiencies in cosmologically simulated disk galaxies.

The results of our study indicate that star formation may deviate significantly from the relations commonly assumed in models of galaxy formation in some regimes and that these deviations can be important for the overall galaxy evolution. Our findings provide strong motivation for exploring the consequences of such deviations and for developing further improvements in the treatment of star formation in galaxy formation simulations.

BER gratefully acknowledges support from a Spitzer Fellowship through a NASA grant administrated by the Spitzer Science Center, and thanks Dan Marrone for helpful ideas. AVK is supported by the NSF grants AST-0239759, AST-0507596, AST-0708154 and by the Kavli Institute for Cosmological Physics at the University of Chicago. AVK thanks the Miller Institute and Astronomy department of UC Berkeley for hospitality during completion of this paper. We thank Nick Gnedin and Konstantinos Tassis for useful discussions, Gary Ferland and collaborators for developing and maintaining the Cloudy code used to tabulate cooling and heating rates and molecular fractions in our simulations, and Volker Springel for making his hydrodynamical simulation code GADGET2 available. Simulations presented here were performed at the `cobalt` system at the National Center for Supercomputing Applications (NCSA) under project TG-MCA05S017. We made extensive use of the NASA Astrophysics Data System and `arXiv.org` preprint server in this study.

REFERENCES

- Abel, T., Anninos, P., Zhang, Y., & Norman, M. L. 1997, *New Astronomy*, 2, 181
 Anninos, P., & Norman, M. L. 1996, *ApJ*, 460, 556
 Bate, M. R., & Burkert, A. 1997, *MNRAS*, 288, 1060

- Beichman, C. A., Myers, P. C., Emerson, J. P., Harris, S., Mathieu, R., Benson, P. J., & Jennings, R. E. 1986, *ApJ*, 307, 337
 Bell, E. F., & de Jong, R. S. 2001, *ApJ*, 550, 212

- Binney, J., & Tremaine, S. 1987, *Galactic dynamics* (Princeton, NJ, Princeton University Press, 1987, 747 p.)
- Black, J. H. 1981, *MNRAS*, 197, 553
- Blanton, M. R., et al. 2001, *AJ*, 121, 2358
- Blanton, M. R., Eisenstein, D., Hogg, D. W., Schlegel, D. J., & Brinkmann, J. 2005, *ApJ*, 629, 143
- Blanton, M. R., et al. 2003, *ApJ*, 592, 819
- Blitz, L., & Rosolowsky, E. 2004, *ApJ*, 612, L29
- 2006, *ApJ*, 650, 933
- Blitz, L., & Thaddeus, P. 1980, *ApJ*, 241, 676
- Blumenthal, G. R., Faber, S. M., Flores, R., & Primack, J. R. 1986, *ApJ*, 301, 27
- Boissier, S., Gil de Paz, A., Boselli, A., & et al. 2006, *ApJS* submitted (astro-ph/0609071)
- Boissier, S., Prantzos, N., Boselli, A., & Gavazzi, G. 2003, *MNRAS*, 346, 1215
- Booth, C. M., Theuns, T., & Okamoto, T. 2007, *MNRAS*, 376, 1588
- Brooks, A. M., Governato, F., Booth, C. M., Willman, B., Gardner, J. P., Wadsley, J., Stinson, G., & Quinn, T. 2007, *ApJ*, 655, L17
- Calzetti, D., et al. 2007, *ApJ*, 666, 870
- Carignan, C., & Beaulieu, S. 1989, *ApJ*, 347, 760
- Cen, R. 1992, *ApJS*, 78, 341
- Cooper, M. C., et al. 2007, *MNRAS*, 376, 1445
- Corbelli, E. 2003, *MNRAS*, 342, 199
- Cox, D. P., & Tucker, W. H. 1969, *ApJ*, 157, 1157
- Dalgarno, A., & McCray, R. A. 1972, *ARA&A*, 10, 375
- Das, M., O’Neil, K., Vogel, S. N., & McGaugh, S. 2006, *ApJ*, 651, 853
- Dekel, A., & Birnboim, Y. 2006, *MNRAS*, 368, 2
- 2007, *MNRAS* submitted (astro-ph/0707.1214), 707
- Dobbs, C., & Bonnell, I. 2007, *ArXiv Astrophysics e-prints*
- Draine, B. T. 1978, *ApJS*, 36, 595
- Draine, B. T., & Bertoldi, F. 1996, *ApJ*, 468, 269
- Elmegreen, B. G. 1989, *ApJ*, 338, 178
- Elmegreen, B. G. 1993a, in *Star-Forming Galaxies and Their Interstellar Media*, ed. J. Franco, F. Ferrini, & G. Tenorio-Tagle, 337
- 1993b, *ApJ*, 411, 170
- Elmegreen, B. G. 1997, in *Revista Mexicana de Astronomia y Astrofisica Conference Series*, ed. J. Franco, R. Terlevich, & A. Serrano, Vol. 6, 165
- 2002, *ApJ*, 577, 206
- Elmegreen, B. G., & Lada, C. J. 1977, *ApJ*, 214, 725
- Elmegreen, B. G., & Parravano, A. 1994, *ApJ*, 435, L121+
- Elmegreen, D. M., Elmegreen, B. G., Ravindranath, S., & Coe, D. A. 2007, *ApJ*, 658, 763
- Ferland, G. J., Korista, K. T., Verner, D. A., Ferguson, J. W., Kingdon, J. B., & Verner, E. M. 1998, *PASP*, 110, 761
- Ferland, G. J., & Mushotzky, R. F. 1984, *ApJ*, 286, 42
- Freeman, K. C. 1970, *ApJ*, 160, 811
- Gao, Y., & Solomon, P. M. 2004, *ApJ*, 606, 271
- Gardan, E., Braine, J., Schuster, K. F., Brouillet, N., & Sievers, A. 2007, *ArXiv e-prints*, 707
- Geha, M., Blanton, M. R., Masjedi, M., & West, A. A. 2006, *ArXiv Astrophysics e-prints*
- Giovanelli, R., & Haynes, M. P. 1983, *AJ*, 88, 881
- Glover, S. C. O., & Mac Low, M.-M. 2007, *ApJS*, 169, 239
- Gnedin, N. Y., Norman, M. L., & Ostriker, J. P. 2000, *ApJ*, 540, 32
- Gnedin, O. Y., Kravtsov, A. V., Klypin, A. A., & Nagai, D. 2004, *ApJ*, 616, 16
- Governato, F., Willman, B., Mayer, L., Brooks, A., Stinson, G., Valenzuela, O., Wadsley, J., & Quinn, T. 2007, *MNRAS*, 374, 1479
- Guhathakurta, P., van Gorkom, J. H., Kotanyi, C. G., & Balkowski, C. 1988, *AJ*, 96, 851
- Haardt, F., & Madau, P. 1996, *ApJ*, 461, 20
- Hernquist, L. 1990, *ApJ*, 356, 359
- Heyer, M. H., Corbelli, E., Schneider, S. E., & Young, J. S. 2004, *ApJ*, 602, 723
- Hippelein, H., Haas, M., Tuffs, R. J., Lemke, D., Stickel, M., Klaas, U., & Völk, H. J. 2003, *A&A*, 407, 137
- Hollenbach, D., & McKee, C. F. 1979, *ApJS*, 41, 555
- 1989, *ApJ*, 342, 306
- Hopkins, A. M. 2004, *ApJ*, 615, 209
- Hopkins, A. M., & Beacom, J. F. 2006, *ApJ*, 651, 142
- Hultman, J., & Pharasyn, A. 1999, *A&A*, 347, 769
- Hunter, D. A., & Elmegreen, B. G. 2004, *AJ*, 128, 2170
- Hunter, D. A., Elmegreen, B. G., & Baker, A. L. 1998, *ApJ*, 493, 595
- Hunter, D. A., Elmegreen, B. G., & Martin, E. 2006, *AJ*, 132, 801
- Ikeuchi, S., & Ostriker, J. P. 1986, *ApJ*, 301, 522
- Jeans, J. H. 1928, *Astronomy and cosmogony* (Cambridge [Eng.] The University press, 1928.)
- Jog, C. J., & Solomon, P. M. 1984, *ApJ*, 276, 114
- Joung, M. K. R., & Mac Low, M.-M. 2006, *ApJ*, 653, 1266
- Karachentsev, I. D., Karachentseva, V. E., Huchtmeier, W. K., & Makarov, D. I. 2004, *AJ*, 127, 2031
- Katz, N. 1992, *ApJ*, 391, 502
- Katz, N., Weinberg, D. H., & Hernquist, L. 1996, *ApJS*, 105, 19
- Kauffmann, G., et al. 2003, *MNRAS*, 341, 54
- Kaufmann, T., Wheeler, C., & Bullock, J. S. 2007, *ArXiv e-prints*, 706
- Kenney, J. D. P., & Young, J. S. 1989, *ApJ*, 344, 171
- Kennicutt, R. C. 1989, *ApJ*, 344, 685
- 1998, *ApJ*, 498, 541
- Kennicutt et al. 2007, *ApJ*, accepted, astro-ph/0708.0922
- Klein, R. I., Fisher, R., & McKee, C. F. 2004, in *Revista Mexicana de Astronomia y Astrofisica Conference Series*, Vol. 22, *Revista Mexicana de Astronomia y Astrofisica Conference Series*, ed. G. Garcia-Segura, G. Tenorio-Tagle, J. Franco, & H. W. Yorke, 3–7
- Kravtsov, A. V. 2003, *ApJ*, 590, L1
- Kravtsov, A. V., Berlind, A. A., Wechsler, R. H., Klypin, A. A., Gottlöber, S., Allgood, B., & Primack, J. R. 2004, *ApJ*, 609, 35
- Kroupa, P. 1995, *MNRAS*, 277, 1522
- Krumholz, M. R., & McKee, C. F. 2005, *ApJ*, 630, 250
- Krumholz, M. R., & Tan, J. C. 2007, *ApJ*, 654, 304
- Krumholz, M. R., & Thompson, T. A. 2007, *ApJ* submitted (astro-ph/0704.0792), 704
- Kuhlen, M., & Madau, P. 2005, *MNRAS*, 363, 1069
- Lada, C. J. 1987, in *IAU Symposium*, Vol. 115, *Star Forming Regions*, ed. M. Peimbert & J. Jugaku, 1–17
- Lee, H., Skillman, E. D., Cannon, J. M., Jackson, D. C., Gehrz, R. D., Polonski, E. F., & Woodward, C. E. 2006, *ApJ*, 647, 970
- Leroy, A., Bolatto, A., Walter, F., & Blitz, L. 2006, *ApJ*, 643, 825
- Leroy, A., Bolatto, A. D., Simon, J. D., & Blitz, L. 2005, *ApJ*, 625, 763
- Li, Y., Mac Low, M.-M., & Klessen, R. S. 2005a, *ApJ*, 620, L19
- 2005b, *ApJ*, 626, 823
- 2006, *ApJ*, 639, 879
- Machacek, M. E., Bryan, G. L., & Abel, T. 2001, *ApJ*, 548, 509
- Martin, C. L., & Kennicutt, R. C. 2001, *ApJ*, 555, 301
- Mathis, J. S., Mezger, P. G., & Panagia, N. 1983, *A&A*, 128, 212
- Mathews, L. D., Gao, Y., Uson, J. M., & Combes, F. 2005, *AJ*, 129, 1849
- McGaugh, S. S. 2005, *ApJ*, 632, 859
- McKee, C. F., & Ostriker, E. C. 2007, *ARA&A* in press (astro-ph/0707.3514)
- Miller, G. E., & Scalo, J. M. 1979, *ApJS*, 41, 513
- Misiriotis, A., Xilouris, E. M., Papamastorakis, J., Boumis, P., & Goudis, C. D. 2006, *A&A*, 459, 113
- Mo, H. J., Mao, S., & White, S. D. M. 1998, *MNRAS*, 295, 319
- Möllenhoff, C., & Heidt, J. 2001, *A&A*, 368, 16
- Monaghan, J. J., & Lattanzio, J. C. 1991, *ApJ*, 375, 177
- Murgia, M., Crapsi, A., Moscadelli, L., & Gregorini, L. 2002, *A&A*, 385, 412
- Nakamura, F., & Umemura, M. 2001, *ApJ*, 548, 19
- Navarro, J. F., Frenk, C. S., & White, S. D. M. 1996, *ApJ*, 462, 563
- 1997, *ApJ*, 490, 493
- Nieten, C., Neinger, N., Guélin, M., Ungerechts, H., Lucas, R., Berkhuijsen, E. M., Beck, R., & Wielebinski, R. 2006, *A&A*, 453, 459
- O’Shea, B. W., & Norman, M. L. 2007, *ApJ*, 654, 66
- Ostriker, J. P., & Gnedin, N. Y. 1996, *ApJ*, 472, L63+
- Padoan, P., Nordlund, A., & Jones, B. J. T. 1997, *MNRAS*, 288, 145
- Passot, T., & Vázquez-Semadeni, E. 1998, *Phys. Rev. E*, 58, 4501
- Pelupessy, F. I., Papadopoulos, P. P., & van der Werf, P. 2006, *ApJ*, 645, 1024
- Press, W. H., & Schechter, P. 1974, *ApJ*, 187, 425
- Press, W. H., Teukolsky, S. A., Vetterling, W. T., & Flannery, B. P. 1992, *Numerical recipes in C. The art of scientific computing* (Cambridge: University Press, [c1992, 2nd ed.)
- Rafikov, R. R. 2001, *MNRAS*, 323, 445
- Rana, N. C. 1987, *A&A*, 184, 104
- 1991, *ARA&A*, 29, 129
- Raymond, J. C., Cox, D. P., & Smith, B. W. 1976, *ApJ*, 204, 290
- Ricotti, M., Gnedin, N. Y., & Shull, J. M. 2001, *ApJ*, 560, 580
- Robertson, B., Bullock, J. S., Cox, T. J., Di Matteo, T., Hernquist, L., Springel, V., & Yoshida, N. 2006a, *ApJ*, 645, 986
- Robertson, B., Cox, T. J., Hernquist, L., Franx, M., Hopkins, P. F., Martini, P., & Springel, V. 2006b, *ApJ*, 641, 21
- Robertson, B., Hernquist, L., Cox, T. J., Di Matteo, T., Hopkins, P. F., Martini, P., & Springel, V. 2006c, *ApJ*, 641, 90
- Robertson, B., Yoshida, N., Springel, V., & Hernquist, L. 2004, *ApJ*, 606, 32
- Rosenberg, J. L., & Schneider, S. E. 2002, *ApJ*, 567, 247
- Rubin, V. C., Waterman, A. H., & Kenney, J. D. P. 1999, *AJ*, 118, 236
- Safronov, V. S. 1960, *Annales d’Astrophysique*, 23, 979
- Salpeter, E. E. 1955, *ApJ*, 121, 161

- Scalo, J., Vazquez-Semadeni, E., Chappell, D., & Passot, T. 1998, *ApJ*, 504, 835
- Schaye, J. 2004, *ApJ*, 609, 667
- Schaye, J., & Dalla Vecchia, C. 2007, *MNRAS* submitted (astro-ph/0709.0292), 709
- Schmidt, M. 1959, *ApJ*, 129, 243
- Schuster, K. F., Kramer, C., Hitschfeld, M., Garcia-Burillo, S., & Mookerjee, B. 2007, *A&A*, 461, 143
- Sheth, R. K., & Tormen, G. 1999, *MNRAS*, 308, 119
- Sijacki, D., Springel, V., Di Matteo, T., & Hernquist, L. 2007, *MNRAS* submitted (astro-ph/0705.2238), 705
- Silk, J. 1997, *ApJ*, 481, 703
- Smith, B. D., Sigurdsson, S., & Abel, T. 2007, ArXiv e-prints, 706
- Smith, L. F., Mezger, P. G., & Biermann, P. 1978, *A&A*, 66, 65
- Spitzer, L. J. 1948, *ApJ*, 107, 6
- Springel, V. 2000, *MNRAS*, 312, 859
- 2005, *MNRAS*, 364, 1105
- Springel, V., Di Matteo, T., & Hernquist, L. 2005, *MNRAS*, 361, 776
- Springel, V., & Hernquist, L. 2003a, *MNRAS*, 339, 289
- 2003b, *MNRAS*, 339, 312
- Springel, V., Yoshida, N., & White, S. D. M. 2001, *New Astronomy*, 6, 79
- Stecher, T. P., & Williams, D. A. 1967, *ApJ*, 149, L29+
- Steinmetz, M., & Müller, E. 1995, *MNRAS*, 276, 549
- Stinson, G., Seth, A., Katz, N., Wadsley, J., Governato, F., & Quinn, T. 2006, *MNRAS*, 373, 1074
- Struck-Marcell, C. 1982, *ApJ*, 259, 116
- Sutherland, R. S., & Dopita, M. A. 1993, *ApJS*, 88, 253
- Talbot, Jr., R. J. 1980, *ApJ*, 235, 821
- Tan, J. C. 2000, *ApJ*, 536, 173
- Tasker, E. J., & Bryan, G. L. 2006, *ApJ*, 641, 878
- 2007, *ApJ* submitted (astro-ph/0709.1972), 709
- Tassis, K. 2007, *MNRAS* submitted
- Tassis, K., Kravtsov, A. V., & Gnedin, N. Y. 2006, *ApJ* submitted (astro-ph/0609763)
- Thacker, R. J., & Couchman, H. M. P. 2000, *ApJ*, 545, 728
- Toomre, A. 1964, *ApJ*, 139, 1217
- Truelove, J. K., Klein, R. I., McKee, C. F., Holliman, II, J. H., Howell, L. H., & Greenough, J. A. 1997, *ApJ*, 489, L179+
- Tully, R. B., & Fisher, J. R. 1977, *A&A*, 54, 661
- van Hoof, P. A. M., Weingartner, J. C., Martin, P. G., Volk, K., & Ferland, G. J. 2001, in *Astronomical Society of the Pacific Conference Series*, Vol. 247, *Spectroscopic Challenges of Photoionized Plasmas*, ed. G. Ferland & D. W. Savin, 363–+
- Wada, K., & Norman, C. A. 2001, *ApJ*, 547, 172
- 2007, *ApJ*, 660, 276
- Wang, B., & Silk, J. 1994, *ApJ*, 427, 759
- Weingartner, J. C., & Draine, B. T. 2001, *ApJS*, 134, 263
- White, S. D. M., & Frenk, C. S. 1991, *ApJ*, 379, 52
- White, S. D. M., & Rees, M. J. 1978, *MNRAS*, 183, 341
- Wild, V., Hewett, P. C., & Pettini, M. 2007, *MNRAS*, 374, 292
- Wolfe, A. M., & Chen, H.-W. 2006, *ApJ*, 652, 981
- Wolfire, M. G., McKee, C. F., Hollenbach, D., & Tielens, A. G. G. M. 2003, *ApJ*, 587, 278
- Wong, T., & Blitz, L. 2002, *ApJ*, 569, 157
- Wu, J., Evans, II, N. J., Gao, Y., Solomon, P. M., Shirley, Y. L., & Vanden Bout, P. A. 2005, *ApJ*, 635, L173
- Wyse, R. F. G. 1986, *ApJ*, 311, L41
- Wyse, R. F. G., & Silk, J. 1989, *ApJ*, 339, 700
- Yang et al. 2007, *ApJ*, accepted, astro-ph/0708.3243
- Yepes, G., Kates, R., Khokhlov, A., & Klypin, A. 1997, *MNRAS*, 284, 235
- Yoshida, N., Abel, T., Hernquist, L., & Sugiyama, N. 2003, *ApJ*, 592, 645
- Yoshida, N., Omukai, K., Hernquist, L., & Abel, T. 2006, *ApJ*, 652, 6
- Young, J. S., & Scoville, N. Z. 1991, *ARA&A*, 29, 581
- Zwaan, M. A., Staveley-Smith, L., Koribalski, B. S., & et al. 2003, *AJ*, 125, 2842

APPENDIX

Truelove et al. (1997) showed that hydrodynamical calculations that do not properly resolve pressure forces on scales where self-gravity begins to dominate over gaseous pressure support are susceptible to a numerical instability that leads to the rapid artificial fragmentation of gas. Truelove et al. (1997) suggest a constraint on the spatial resolution of hydrodynamical mesh calculations such that the Jeans length λ_{Jeans} is locally larger than the grid resolution Δx . This resolution requirement for grid codes can be expressed in terms of a constraint on the “Jeans number” $J = \Delta x / \lambda_{\text{Jeans}} < 0.25$ to properly resolve the Jeans scale and prevent such artificial fragmentation.

Similarly, the inability of SPH codes to capture pressure forces properly on scales less than the smoothing length can also allow for numerically-induced fragmentation if the smoothing length is of order the Jeans length (Bate & Burkert 1997). As discussed by Bate & Burkert (1997) and in §2.3, the requirement that the Jeans scale is resolved an SPH calculation by some number N_{Jeans} of SPH kernels is $2N_{\text{Jeans}}N_{\text{neigh}}m_{\text{gas}} < m_{\text{Jeans}}$, where m_{gas} is the SPH particle mass and N_{neigh} is the number of SPH neighbors. A similar requirement can be formulated in terms of relevant spatial scales (e.g., Klein et al. 2004). Owing to the temperature dependence of the sound speed ($c_s \propto \sqrt{T}$ for ideal gas) and the dependence of the Jeans scale on density and temperature, it is clear that for a given number of gas particles N_{gas} used in an SPH calculation, the lower the temperature floor allowed the more potentially susceptible the simulated fluid will be to numerical Jeans fragmentation. SPH simulations of the ISM in galaxies with molecular coolants must be especially cautious given the typical numerical resolutions, high densities, and potentially low temperatures.

For SPH calculations in the literature, typical approaches for addressing numerical Jeans instability include improving the numerical resolution such that the Jeans scale is resolved with $N_{\text{Jeans}} = 1$, as suggested by Bate & Burkert (1997), or using sink particles to represent high density regions of the ISM (e.g. Li et al. 2005b, 2006; Booth et al. 2007). Each of these approaches have possible drawbacks, as the Bate & Burkert (1997) resolution criterion can clearly depend on the density, depending on the gas equation-of-state, and the sink particle method, depending on its implementation, may neither avoid numerical fragmentation nor properly capture the complicated chemical, thermodynamical, and radiative processes that operate in dense ISM gas. Another possible solution is to use a stiffer equation-of-state for the gas (e.g., Springel et al. 2005; Schaye & Dalla Vecchia 2007).

Instead, the simulations presented in this paper adopt a pressure floor on the scale of the Jeans length through an approach similar to that implemented by Machacek et al. (2001) in grid codes. Machacek et al. (2001) adopt an effective pressure P_{eff} on the scale of the finest grid resolution Δx , given by

$$P_{\text{eff}} = KG\rho_b^2\Delta x^2/\mu \quad (1)$$

where ρ_b is the baryon density in the cell, μ is the mean molecular mass, G is the gravitational constant, and $K \approx 100$ is a parameter that sets the effective resolution of their simulations. If the effective pressure $P \propto \rho u$ on the scale of the SPH kernel is set to ensure the Jeans scale is over-resolved by a factor N_{Jeans} , then the internal energy of gas particles with kernel mass

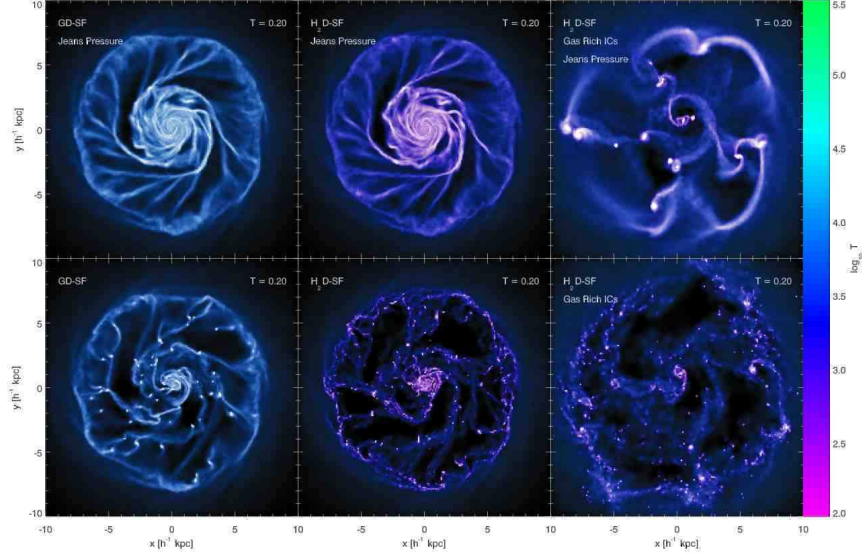


FIG. A1.— Mitigation of numerical Jeans fragmentation. Shown are simulations of an isolated galaxy model with a circular velocity of $v_{\text{circ}} = 160 \text{ km s}^{-1}$ evolved with (upper row) and without (lower row) a pressure floor to resolve the local Jeans mass and length. The image intensity tracks the surface density while the color reflects the gas effective temperature. For galaxy systems of this mass and disk structure with gas fractions of $f_{\text{gas}} = 0.2$ and simulated with $N = 400,000$ gas particles, the local Jeans mass is smaller than the typical mass in an SPH kernel if its ISM is modeled with either atomic cooling and a $T = 10^4 \text{ K}$ temperature floor (lower left panel) or atomic and molecular cooling with a $T = 10^2 \text{ K}$ temperature floor (lower middle panel). These systems are susceptible to numerical fragmentation since, owing to the limited resolution, the local gas pressure is artificially low on the scale where the gas is marginally stable against collapse through self-gravity (Bate & Burkert 1997). To avoid this numerical artificiality, a pressure-floor is introduced to increase the local sound speed until the Jeans scale is resolved by several SPH kernels. Our prescription allows for galaxy models with either atomic cooling at temperatures $T > 10^4 \text{ K}$ (upper left panel) or atomic and molecular cooling at temperatures $T > 10^2 \text{ K}$ (upper middle panel) to be evolved stably. Systems that are extremely gas-rich (e.g., $f_{\text{gas}} = 0.99$, right panels) can still become globally unstable and undergo large scale fragmentation if a pressure-floor is used (upper right panel), but they catastrophically fragment without such preventative measures (lower right panel).

$m_{\text{SPH}} \sim N_{\text{neigh}} m_{\text{gas}}$ should be scaled as

$$u = u \times \begin{cases} \left(\frac{N_{\text{Jeans}}}{h_{\text{Jeans}}} \right)^{2/3} & : h_{\text{Jeans}} < N_{\text{Jeans}} \\ \left(\frac{2N_{\text{Jeans}} m_{\text{SPH}}}{m_{\text{Jeans}}} \right)^{2/3} & : m_{\text{Jeans}} < 2N_{\text{Jeans}} m_{\text{SPH}} \end{cases}, \quad (2)$$

which is Equation 10 from §2.3. A factor $N_{\text{Jeans}} = 1$ would correspond to a density-dependent version of the Bate & Burkert (1997) criterion, while applying the effective pressure of Machacek et al. (2001) with $K \sim 100$ and equating $\Delta x \sim h$ would imply $N_{\text{Jeans}} \gtrsim 1000$. Klein et al. (2004) provide a survey of the literature and find that values of $N_{\text{Jeans}} \sim 0.4 - 30$ for a fixed maximum density are in common usage.

As briefly mentioned in §2.3, we have performed a variety of resolution studies where we examine the range of $N_{\text{Jeans}} = 1 - 100$ and found $N_{\text{Jeans}} \approx 15$ to provide sufficient stability for our studies. The resolution studies utilized a galaxy model initialized with a virial velocity $V_{\text{vir}} = 160 \text{ km s}^{-1}$, spin $\lambda = 0.033$, NFW concentration $c = 9$, disk mass fraction $m_{\text{d}} = 0.05$, bulge mass fraction $m_{\text{b}} = 0.0167$, and disk gas fraction $f_{\text{gas}} = 0.2$ according to the method described in §2.5. The dark matter halo, bulge, stellar disk, and gaseous disk were resolved with $N_{\text{DM}} = 120,000$, $N_{\text{b}} = 40,000$, $N_{\text{d}} = 128,000$, and $N_{\text{g}} = 400,000$ particles respectively, and the halo and baryonic particle gravitational softenings were set to $\epsilon_{\text{DM}} = 100h^{-1} \text{ pc}$ and $\epsilon_{\text{b}} = 50h^{-1} \text{ pc}$. The mass contained within the SPH kernel with $N_{\text{neigh}} = 64$ for this galaxy model was typically $m_{\text{SPH}} = 2 \times 10^6 M_{\odot}$. The galaxy model was evolved with two ISM models, the atomic cooling treatment with a temperature floor of $T = 10^4 \text{ K}$ (the GD-SF model) and the atomic and molecular cooling treatment with a temperature floor of $T = 10^2 \text{ K}$ (the H₂D-SF model). Figure A1 shows the disk galaxy evolved with a density-dependent pressure floor described by Equation 10 with $N_{\text{Jeans}} = 15$ (upper row) and without a pressure floor (lower row) evolved in isolation for $t = 0.2 \text{ Gyr}$. The systems without a pressure floor quickly fragment if the effective temperature floor is either $T = 10^2 \text{ K}$ (lower middle panel) or $T = 10^4 \text{ K}$ (lower left panel), as the Jeans mass is initially not resolved at the highest gas densities for either temperature. By design, the simulations that include the suggested pressure floor do not fragment on the Jeans scale (upper row). The pressurization on the Jeans scale used to ameliorate artificial fragmentation does not insure that simulated disks will avoid other instabilities, such as global Toomre (1964) instability. The right panels of Figure A1 show the $V_{\text{vir}} = 160 \text{ km s}^{-1}$ disk model with the disk gas fraction increased to $f_{\text{gas}} = 0.99$, evolved for $t = 0.2 \text{ Gyr}$ in isolation. The gas rich model simulated without a pressure floor violently fragments, but the gas rich model evolved using a pressure floor also undergoes fragmentation on a much larger mass scale. As discussed in Springel & Hernquist (2003a), Robertson et al. (2004) and Springel et al. (2005), systems like this gas rich model that are violently Toomre-unstable when using an ideal gas or weakly pressurized equation-of-state can be stabilized by adopting a more strongly pressurized ISM equation-of-state, but we do not examine such models here.

We note that separating artificial fragmentation and physical Jeans fragmentation owing to self-gravity may be difficult without detailed resolution studies that examine the convergence of the growth rate of perturbations on different size scales. To illustrate

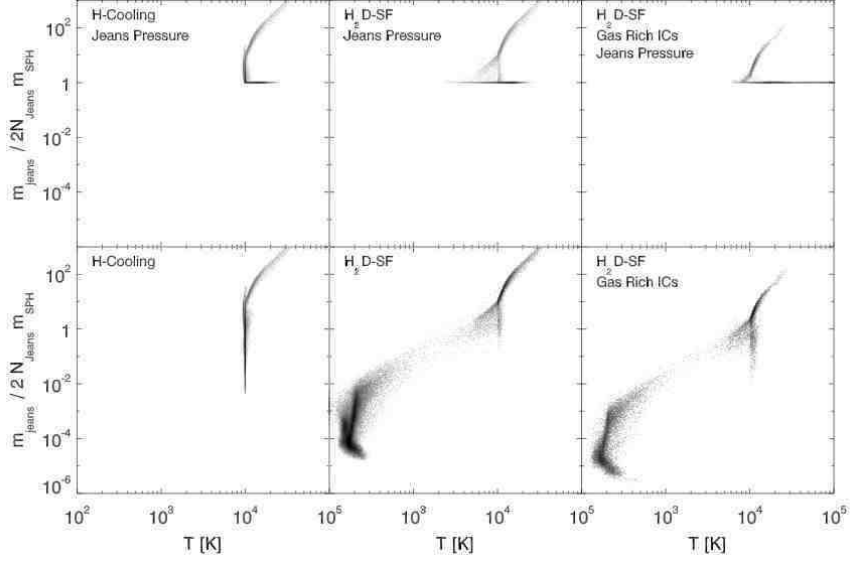


FIG. A2.— Effective resolution of simulations with (top row) and without (bottom row) a pressure floor to over-resolve the Jeans mass and length by a factor $N_{\text{Jeans}} = 15$. When a pressure floor is used the internal energy of gas particles is scaled in a density-dependent way, corresponding to the increase in temperature along the $m_{\text{Jeans}}/2N_{\text{Jeans}}m_{\text{SPH}} = 1$ line in the upper panels. For galaxy systems of this mass and disk structure with gas fractions of $f_{\text{gas}} = 0.2$ and simulated with $N = 400,000$ gas particles, the local Jeans mass is smaller than the typical mass in an SPH kernel if the ISM is modeled with either atomic cooling and a $T = 10^4\text{K}$ temperature floor (lower left panel) or atomic and molecular cooling and a $T = 10^2\text{K}$ temperature floor (lower middle panel). The systems are under-resolved by a factor of $m_{\text{Jeans}}/2N_{\text{Jeans}}m_{\text{SPH}} \sim 100$ for a $T = 10^4\text{K}$ temperature floor or $m_{\text{Jeans}}/2N_{\text{Jeans}}m_{\text{SPH}} > 10,000$ for a $T = 10^2\text{K}$ temperature floor. The discrepancy is larger for larger gas fractions (e.g., $f_{\text{gas}} = 0.99$, lower right panel), and requires a higher artificial pressurization to resolve the Jeans scale (upper right panel). Simulating molecular cooling in Milky Way-sized disks using SPH without using an artificial pressure floor may require $N \sim 10^8 - 10^9$ gas particles to avoid numerical Jeans fragmentation.

the difficulty associated with this approach, Figure A2 shows the effective resolution $m_{\text{Jeans}}/2N_{\text{Jeans}}m_{\text{SPH}}$ of the simulations presented in Figure A1 as a function of the local dynamical gas temperature $T \approx (\gamma - 1)\mu u/k$, where k is the Boltzmann constant and $\gamma = 5/3$ is the ratio of specific heats. For Galaxy systems of this mass and disk structure with gas fractions of $f_{\text{gas}} = 0.2$ simulated with $N = 400,000$ gas particles, the local Jeans mass is smaller than the typical mass in an SPH kernel if either an ISM model with atomic cooling and a $T = 10^4\text{K}$ temperature floor (the GD-SF model, lower left panel) or an ISM model with atomic + molecular cooling and a $T = 10^2\text{K}$ temperature floor (the $\text{H}_2\text{D-SF}$ model, lower middle and lower right panels) is used, by a factor of $m_{\text{Jeans}}/2N_{\text{Jeans}}m_{\text{SPH}} \sim 100$ for a $T = 10^4\text{K}$ temperature floor or $m_{\text{Jeans}}/2N_{\text{Jeans}}m_{\text{SPH}} > 10,000$ for a $T = 10^2\text{K}$ temperature floor. The simulations that include a pressure floor maintain $m_{\text{Jeans}}/2N_{\text{Jeans}}m_{\text{SPH}} \approx 1$ by design, with a small scatter induced by fluctuations in m_{SPH} from changing particle masses from star formation and the small allowed range of neighbors $N_{\text{neigh}} = 62 - 66$. While we caution against over-interpreting the effective Jeans resolution, Figure A2 suggests that simulating molecular cooling in Milky Way-sized disks with SPH *without* using an artificial pressure floor would require $N \sim 10^9 - 10^{10}$ gas particles to avoid numerical Jeans fragmentation with the effective equation-of-state calculated using Cloudy. We delay such resolution studies for future work (and faster computers).

Unwanted fragmentation of the ISM in disks may be closely related to the angular momentum problem for producing realistic disk galaxies in cosmological simulations (see, e.g., §6 of Robertson et al. (2004) and Robertson et al. (2006a)). The simulations of a Milky Way analogue galaxy model presented in this appendix contain $N_{\text{gas}} = 400,000$, which exceeds the numerical resolution of many disk galaxies formed in cosmological simulations to date. Both Truelove et al. (1997) and Bate & Burkert (1997) comment on the possible implications of numerical Jeans fragmentation for studies of galaxy formation; based on these test simulations we suggest that to reliably follow the formation and evolution of disks using SPH simulations a pressure floor similar to our Equation 10 should be used. Prescriptions that mimic pressurization from the multiphase structure of the ISM that may develop through feedback from star formation (e.g., Yepes et al. 1997; Hultman & Pharasyn 1999; Springel 2000; Thacker & Couchman 2000; Springel & Hernquist 2003a; Stinson et al. 2006; Schaye & Dalla Vecchia 2007) may also serve to ameliorate numerical Jeans fragmentation by raising the sound speed as a function of the mean ISM density. This affect is apparent in numerical tests examining the stability of isolated disks by Springel et al. (2005) using various ISM equations-of-state. We plan to revisit the implications of numerical Jeans fragmentation on cosmological simulations of galaxy formation in future work. Lastly, we note that since disks that are Toomre-unstable are also roughly Jeans-unstable (see, e.g., Krumholz & McKee 2005), numerical Jeans fragmentation will artificially reinforce any natural correspondence between gravitational instability and star formation. Simulations that examine the relation between star formation and the Toomre instability parameter Q_{sg} should therefore explicitly demonstrate that the Jeans scale is properly resolved at all densities.

APPENDIX

As discussed in §3.4, the simulated galaxies display a correlation between the star formation rate surface density Σ_{SFR} and the product of the total gas surface mass density Σ_{gas} and the angular frequency Ω in regions where the molecular gas and total gas densities are comparable. The correlation in our simulations is similar to the observed $\Sigma_{\text{SFR}} - \Sigma_{\text{gas}}\Omega$ correlation (e.g., Kennicutt

1998; Kennicutt et al. 2007). Since the star formation relation implemented in the simulations calculates the star formation rate density $\dot{\rho}_*$ as proportional to the product of the molecular fraction f_{H_2} and the gas density scaled with the local dynamical time $\rho_g^{1.5}$ (Equation 4), the $\Sigma_{\text{SFR}} - \Sigma_{\text{gas}} \Omega$ correlation would occur if the angular frequency scaled with the density as $\Omega \propto \sqrt{\rho_g}$. Note that it is not at all clear why such a relation should hold, given that gas density is local while orbital frequency is determined by the overall mass distribution and potential of the galaxy. Here we show that the relation between ρ_g and Ω with a similar scaling exists for self-gravitating exponential disks or exponential disks embedded in realistic dark matter potentials.

Given the axisymmetry of the disk galaxy models, the angular frequency is related to the density through Poisson's equation

$$\frac{d^2\Phi}{dz^2} + \frac{d^2\Phi}{dR^2} + \Omega^2 = 4\pi G \rho_{\text{total}}. \quad (1)$$

(Equation 26 in §3.4). Below, the scaling of the angular frequency Ω with the local disk density ρ_{disk} is calculated in the limiting cases of potentials dominated by disks ($\rho_{\text{total}} \approx \rho_{\text{disk}}$) or dark matter halos ($\rho_{\text{total}} \approx \rho_{\text{DM}}$) for exponential disks ($\rho_{\text{disk}} \propto \exp[-R/R_d]$), and we show that for the examined cases $\Omega \propto \sqrt{\rho_{\text{disk}}} B(R/R_d)$, where $B(R/R_d) \sim \mathcal{O}(1)$ is a weak function of the disk radius R that depends on the form of the dominate potential.

1. Exponential Disk-Dominated Potentials, $\rho_{\text{disk}} \gg \rho_{\text{DM}}$

For a flattened system, Binney & Tremaine (1987) recognized that as the vertical scale h of the density distribution decreases the first term on the left hand side of Equation 26 begins to dominate and eventually

$$\frac{d^2\Phi}{dz^2} \simeq 4\pi G \rho. \quad (2)$$

If the surface density of the disk is exponential, the axisymmetric density distribution of the disk can be written as

$$\rho_d(R, z) = \frac{A \Sigma_0}{R_d} \exp(-R/R_d) f(z) \quad (3)$$

where $f(z) \propto \text{sech}^2(z)$ is determined by Equation 2, and the constant A is determined by taking $f(0) = 1$ and the integral constraint from the disk mass. Using the methods of §2.6.3 of Binney & Tremaine (1987), one can show that the rotation curve in the plane of a very thin exponential disk is

$$v_c^2(R) = 4\pi G \Sigma_0 R_d y^2 [I_0(y)K_0(y) - I_1(y)K_1(y)], \quad (4)$$

where $y \equiv R/R_d$ (Freeman 1970). Substituting for Σ_0/R_d from Equation 3, as is appropriate if the gas densities in the disk plane decrease in proportion to the surface density, we find

$$\Omega_{\text{disk}}(R) = \left\{ 4\pi G A^{-1} \rho_d(R, z) \exp(y) \times [I_0(y)K_0(y) - I_1(y)K_1(y)] \right\}^{1/2} \quad (5)$$

$$= \sqrt{\rho_d} B_{\text{disk}}(R/R_d). \quad (6)$$

The function $B_{\text{disk}}(x)$ is a weak function of the disk surface density $\Sigma(R)$. Over the inner 95% of the disk mass ($x \in \{0.355, 4.75\}$), the fractional deviation from the $\Omega \propto \sqrt{\rho_d}$ correlation, normalized to the disk properties at one scale length, is only $B(0.355)/B(1) - 1 = 0.48$ near the disk center and $B(4.75)/B(1) - 1 = -0.26$ in the disk exterior.

2. Halo-Dominated Potentials, $\rho_{\text{DM}} \gg \rho_{\text{disk}}$

In the case of $\rho_{\text{total}} \approx \rho_{\text{DM}}$, the angular frequency can be determined directly from the integrated mass M within a radius R as

$$\Omega^2 = \frac{GM(<R)}{R^3}. \quad (7)$$

There are a wide variety of possible dark matter halo profiles, but we limit ourselves to three salient models.

Dark matter halos in cosmological simulations on average follow the Navarro et al. (1996) (NFW) dark matter halo profile, given by

$$\rho_{\text{DM}}(R, z) = \frac{4\rho_s}{(\sqrt{R^2 + z^2}/r_s)(1 + \sqrt{R^2 + z^2}/r_s)^2}, \quad (8)$$

where ρ_s is the density at the scale radius r_s . If we substitute for the disk density

$$\rho_s = f_d^{-1} \rho_d(R, z) \exp(R/R_d - r_s/R_d), \quad (9)$$

then the angular frequency in the disk plane of a NFW profile can be written

$$\Omega_{\text{NFW}}(R) = \sqrt{\rho_d} B_{\text{NFW}}(R/r_s), \quad (10)$$

where the function

$$B_{\text{NFW}}(x) = \left\{ 16\pi G f_d^{-1} \exp\left(\frac{r_s(x-1)}{R_d}\right) \left[\frac{(1+x)\ln(1+x) - x}{x^3(1+x)} \right] \right\}^{1/2} \quad (11)$$

is, again, a weak function of the disk surface density $\Sigma(R)$. Over the inner 95% of the disk mass, the fractional deviation from the $\Omega \propto \sqrt{\rho_d}$ correlation, normalized to the disk properties at one scale length, is only $B_{\text{NFW}}(0.355R_d/r_s)/B_{\text{NFW}}(R_d/r_s) - 1 = 0.27$ near the disk center and $B_{\text{NFW}}(4.75R_d/r_s)/B_{\text{NFW}}(R_d/r_s) - 1 = 1.45$ in the disk exterior.

Alternatively, we can consider the Hernquist (1990) profile

$$\rho_{\text{H}}(R, z) = \frac{8\rho_a}{(\sqrt{R^2 + z^2}/a)(1 + \sqrt{R^2 + z^2}/a)^3}, \quad (12)$$

where ρ_a is the density at a scale radius a . The Hernquist (1990) profile is used as the DM halo profile in the galaxy models presented in this paper and has a density and potential similar to the NFW profile within the scale radius. Substituting for the disk density, we can write

$$\rho_a = f_d^{-1} \rho_d(R, z) \exp(R/R_d - a/R_d). \quad (13)$$

The mass profile of the Hernquist (1990) halo provides

$$\Omega_{\text{H}}(R) = \sqrt{\rho_d} B_{\text{H}}(R/a) \quad (14)$$

where the function

$$B_{\text{H}}(x) = \left\{ 32\pi G f_d^{-1} \exp\left[\frac{a(x-1)}{R_d}\right] \left[\frac{1}{x(1+x)^2}\right] \right\}^{1/2} \quad (15)$$

has a scaling nearly identical to the function $B_{\text{NFW}}(x)$ when $x \ll 1$, and is a correspondingly weak function of the disk surface density $\Sigma(R)$. Over the inner 95% of the disk mass, the fractional deviation from the $\Omega \propto \sqrt{\rho_d}$ correlation, normalized to the disk properties at one scale length, is only $B_{\text{H}}(0.355R_d/a)/B_{\text{H}}(R_d/a) - 1 = 0.26$ near the disk center and $B_{\text{H}}(4.75R_d/a)/B_{\text{H}}(R_d/a) - 1 = 1.48$ in the disk exterior.

In real galaxies, it is thought that the dark matter halo will adiabatically compress in response to the dissipational formation of the disk (e.g., Blumenthal et al. 1986). Models of adiabatic compression suggest that the dark matter halo response tends to drive the halo profile to resemble an isothermal sphere over much of the disk (Gnedin et al. 2004). The isothermal density profile can be written

$$\rho_{\text{iso}}(R, z) = \frac{\rho_0}{(\sqrt{R^2 + z^2}/r_0)^2}, \quad (16)$$

where ρ_0 is the density at an arbitrary scale radius r_0 . For simplicity, we set $r_0 = R_d$ and substitute for the disk density as

$$\rho_0 = f_d^{-1} \rho_d(R, 0) \exp(R/R_d - 1). \quad (17)$$

Integrating the isothermal density profile to find the enclosed mass provides the angular frequency in the disk plane as

$$\Omega_{\text{iso}}(R) = \sqrt{\rho_d} B_{\text{iso}}(R/R_d) \quad (18)$$

where

$$B_{\text{iso}}(x) = \{4\pi G f_d^{-1} x^{-2} \exp(x-1)\}^{1/2}. \quad (19)$$

The function $B_{\text{iso}}(x)$ is also weak function of the disk surface density $\Sigma(R)$, and is of the same order as B_{NFW} or B_{H} . Over the inner 95% of the disk mass, the fractional deviation from the $\Omega \propto \sqrt{\rho_d}$ correlation, normalized to the disk properties at one scale length, is only $B_{\text{iso}}(0.355)/B_{\text{iso}}(1) - 1 = 1.04$ near the disk center and $B_{\text{iso}}(4.75)/B_{\text{iso}}(1) - 1 = 0.37$ in the disk exterior.

3. The $\Sigma_{\text{SFR}} - \Sigma\Omega$ Correlation

Figure B1 summarizes the behavior of the functions Ω_{disk} , Ω_{NFW} , Ω_{H} , and Ω_{iso} . In the Hernquist (1990) and Navarro et al. (1996) halo potential models, the disk scale length-to-halo scale radius ratios were set to $R_d/r_s = 0.1$ appropriate for observed spiral galaxies. The quantity $\Sigma(R)^{1.5} \propto \Sigma_{\text{SFR}}$ is plotted as a function of the product $\Sigma(R)\Omega(R)$, normalized to the disk properties at the scale length R_d over the radial range $R = [0, 5R_d]$, for the potentials calculated in this Appendix. The quantity $\Sigma\Omega$ closely tracks $\Sigma^{1.5}$ throughout the disk, demonstrating that deviations from the $\Omega \propto \sqrt{\rho_d}$ correlation are typically $\sim \mathcal{O}(1)$. Hence, the $\Sigma_{\text{SFR}} - \Sigma\Omega$ relation may be understood in terms of the scaling of the local density in exponential disks with the angular frequency of realistic galaxy potentials, rather than some more fundamental relation connecting star formation processes in the ISM with global disk properties. Regions of galaxies with large molecular gas fractions ($\Sigma_{\text{H}_2} \sim \Sigma_{\text{gas}}$) are then expected to follow the $\Sigma_{\text{SFR}} - \Sigma\Omega$ relation, as demonstrated by our simulations (see §3.4). We note that while a different normalization would reduce the typical deviation from the $\Sigma^{1.5}$ scaling, the high-density portion of the relation corresponding to the region where the rotation curve is rapidly increasing should produce a shallower relation than $\Sigma_{\text{SFR}} \propto \Sigma\Omega$. Weak evidence for this may exist in the available data (e.g., the inner-disk region of Figure 9 of Kennicutt et al. 2007).

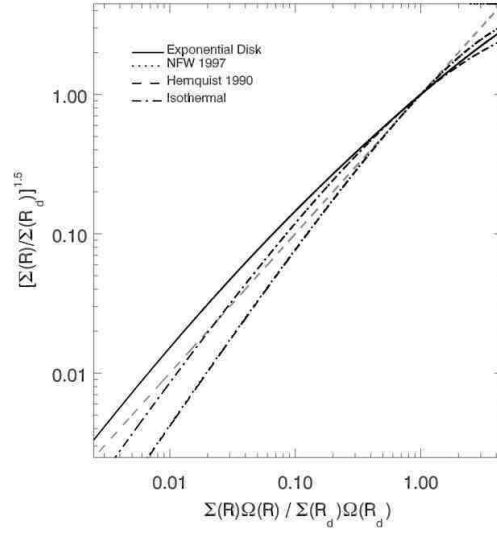


FIG. B1.— Relation between surface density Σ and angular frequency Ω for a variety of disk galaxy model potentials. Shown is the quantity $\Sigma^{1.5} \propto \Sigma_{\text{SFR}}$ plotted against the product $\Sigma\Omega$ for exponential disks in a disk-dominated (solid line), Navarro et al. (1997) halo-dominated (dotted line), Hernquist (1990) halo-dominated (dashed line), or isothermal halo-dominated (dash-dotted line) potential, normalized to the disk properties at an exponential scale length. Deviations from the $\Sigma^{1.5} \propto \Sigma\Omega$ correlation (indicated with a dashed grey line) are typically $\sim \mathcal{O}(1)$ and are largest in the very center and exterior of the disk. The calculation suggests that the $\Sigma_{\text{SFR}} \propto \Sigma\Omega$ may simply reflect the scaling of the local density in exponential gas disks with the characteristic shape of the potentials that host them, rather than an a fundamental connection between star formation and global disk processes.